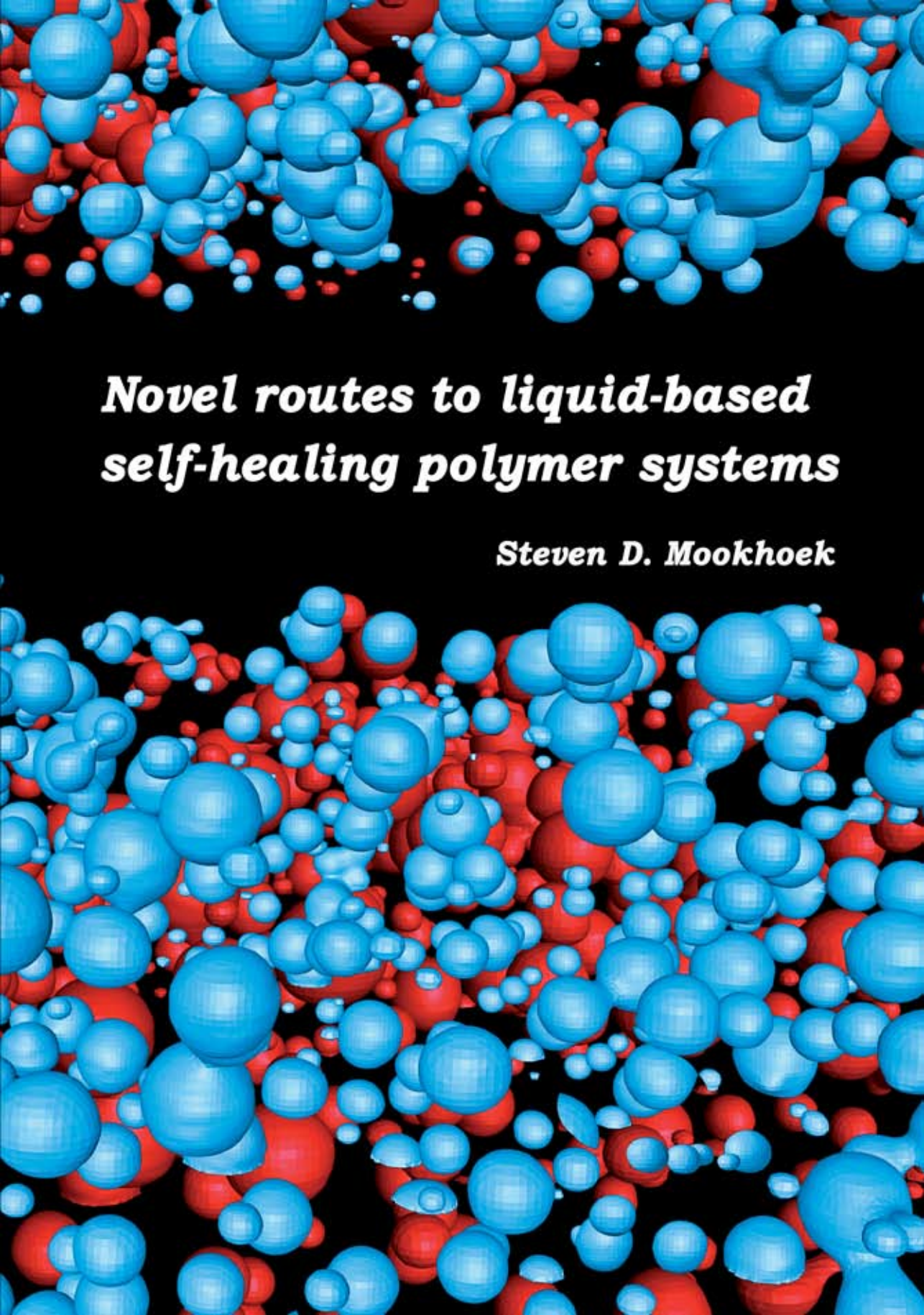

Novel routes to liquid-based self-healing polymer systems

Steven D. Mookhoek

Novel routes to liquid-based self-healing polymer systems

Proefschrift

ter verkrijging van de graad van doctor
aan de Technische Universiteit Delft,
op gezag van de Rector Magnificus Prof. ir. K.Ch.A.M. Luyben,
voorzitter van het College voor Promoties,
in het openbaar te verdedigen op 6 september 2010 om 10:00 uur

door

Steven Dirk MOOKHOEK

scheikundig ingenieur
geboren te Oostburg

Dit proefschrift is goedgekeurd door de promotor:
Prof. dr. ir. S. van der Zwaag

Samenstelling promotiecommissie:

Rector Magnificus,	voorzitter
Prof. dr. ir. S. van der Zwaag,	Technische Universiteit Delft - promotor
Dr. H. R. Fischer,	TNO Industrie & Techniek
Prof. dr. S. J. Picken,	Technische Universiteit Delft
Prof. dr. J. H. van Esch,	Technische Universiteit Delft
Prof. dr. F. E. Du Prez,	Universiteit Gent, België
Prof. dr. W. Ludwig,	European Synchrotron Radiation Facility, Frankrijk
Prof. dr. F. R. Jones,	University of Sheffield, Verenigd Koninkrijk

Dr. H. R. Fischer heeft als begeleider in belangrijke mate aan de totstandkoming van het proefschrift bijgedragen.

Het onderzoek dat in dit proefschrift wordt beschreven is deel van het onderzoeksprogramma van het Dutch Polymer Institute (DPI), postbus 902, 5600 AX Eindhoven, project #582.

ISBN 978-90-9025592-7

Ontwerp omslag door Steven Dirk Mookhoek
mookhoek@gmail.com

Novel routes to liquid-based self-healing polymer systems

voor Renée & mijn ouders...

Contents

CHAPTER 1

An introduction to self-healing materials

> The Sun, with all planets revolving around it, and depending on it, can still ripen a bunch of grapes as though it had nothing else in the Universe to do.
>
> *Galileo Galilei*

1.1 Biological vs. man-made materials

All materials that surround us have designed properties in order to fulfil their function in a desired application. Biological materials in nature have developed and evolved over the course of time to obtain properties that are either flexible, rigid, hard, etc. for instance by changing the structure and morphology by variances in composite composition and crosslink density.[1] Moreover, nature has evolved in the direction of complex hierarchal and adaptive systems that are equipped with autonomous mechanisms able to respond on external stimuli.[2–5] For instance bone-structure, contains cells that can sense the current stress state of the structure.[6,7] The cells can communicate with other cells that are able to grow bone were needed, such as when becoming bigger and heavier. These cells are also able to break down bone when the the properties of the bone are highly over-dimensionised, such as in the case of astronauts at zero gravity. Furthermore, the cells can reconstruct bone-structure in the event of formation of (micro)cracks due to over-stressing. In bone, therefore there is an dynamic equilibrium between the construction and the destruction of material at required sites as a function of the local stress-state. Similarly the design of skin is fully tailored to its

application and expected cuts. Skin consists of many different tissue layers and cells, which are interpenetrated by blood vessels. The function of all the individual components within the complex structure is tuned such that skin is able to contract after opening and heal a cut very quickly without loosing large amounts of blood and keeping infections out.[7,8]

In contrast, man-made engineering materials generally demonstrate excellent (mechanical) properties, which often far exceed those of natural materials, but lack the ability to act on changes in their environment, such as inflicted damage. To illustrate this a comparison between the complex material structure of human skin and a common automotive coating is displayed in Figure 1.1.

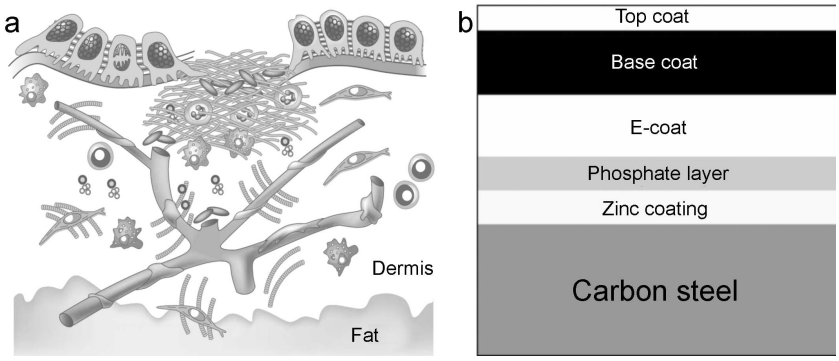

Figure 1.1: Schematic representation of a cross-section of a) human skin and b) an commercial automotive coating showing the difference in morphology and level of complexity in the structure of the material

The inability of the coating to act upon the occurrence of damage is the unintentional consequence of a *Damage Prevention* paradigm,[9] underlying all current engineering material optimization strategies. Accurately defined microstructures have been developed for all these materials that most effectively delay the point at which the formation of damage occurs.

As a consequence, in conventional engineering materials the total amount of damage in a material will always increase (or at best stay constant) with time:

$$\frac{d\,(Damage)}{dt} \geq 0, (0 < t < \text{lifetime}) \tag{1.1}$$

The design concept of *Damage Prevention* has been a very useful concept and will also serve for the future development of new materials. Nevertheless, periodic inspection of the designed structures will be required to follow the damage development in time. Observed damage can be repaired manually, but will imply human intervention and additional costs.

1.2 Damage management

The *Damage Prevention* approach is in sharp contrast to the design concept of biological materials, earlier described. While bio-materials are also optimised to meet the necessary requirements, they contain an intrinsic healing capacity which is able to deal with damage, reconstruct the material and recover the intrinsic material properties. This built-in autonomous counteracting mechanism by nature can be defined as an example of material *Damage Management*. Inherent to this concept the materials must have a rate of damage formation that is smaller than zero at one or more stages within their lifetime:

$$\frac{d\,(Damage)}{dt} \leq 0, \left(t_i < t < t_{i+\Delta t_{\text{healing}}}\right) \tag{1.2}$$

A comparison between the effect of the *Damage Prevention* optimisation for currently engineering materials and the suggested *Damage management* strategy on the development of damage in time is shown schematically in Figure 1.2.

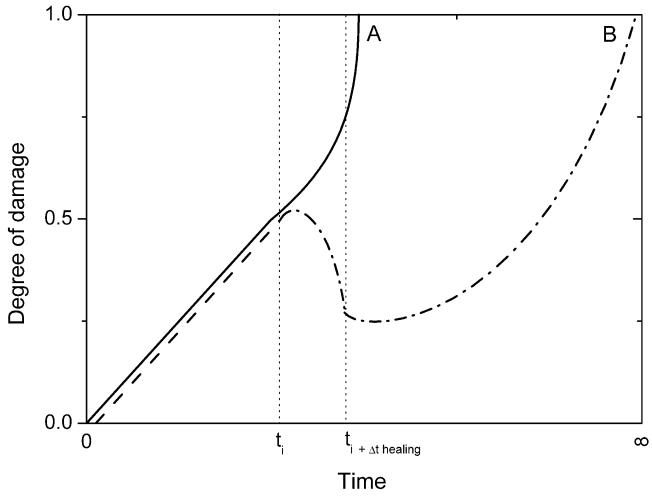

Figure 1.2: Schematic diagram of the functions of the development of damage versus time for A) a classical engineering material according to the *Damage Prevention* paradigm and B) according to the *Damage Management* strategy with a built-in self-healing functionality.

In order to mimic biology and create a man-made material based on the concept of *Damage Management*, currently designed materials will need to be re-engineered with nature's structure-functionality design philosophy in mind. [10] Introducing such a self-healing functionality in an engineering material would be a giant leap forward in material design. The new

class of materials would have a longer lifetime, higher degree or reliability and would require less maintanace than any currently available material.

When examining biological materials at a high level of abstraction, it appears that a natural self-healing material generally has three key constituents that are required in order to create a self-healing material.[9] The first and the largest fraction of the material consists of structural elements and should be responsible for the macroscopic material (mechanical) properties. Thus, a self-healing polymer is foremost a polymer, just as a self-healing concrete is a concrete. The second fraction, which forms the most discriminating aspect of a self-healing material, is a mobile constituent that transports material to a damaged site or crack where it fills the flaw and neutralises the damage by rebonding the crack-surfaces. A third and often small fraction is there to signal the damage. However sometimes this third component is absent and the damage occurrence itself will trigger the healing response.

It is also important that the size of the damage is relatively small and stays constant when a healing reaction takes place. Proper healing generally does not occur when damage results in the full separation of two fractured pieces. Hence, material self-healing is much easier to realise in situations of partial cracking only. This also indicates that healing is favoured when the applied load on the material is reduced or even removed, as this leads to a reduction of crack opening.

In order to incorporate the three key constituents in a synthetic engineering material, the material engineer should no longer only tailor the conventional material properties, *e.g.* stiffness, strength, etc., but should also engineer a way to mobilise a 'healing component' to the damaged site. The latter requires an unconventional approach on material design and manufacturing.

1.3 Liquid-based self-healing polymer systems

One of the first man-made materials with an intentional self-healing functionality was created by Dry.[11] The material she created was a cementeous material containing glass tubes filled with a liquid cyano-acrylate resin. Making use of the intrinsic fluidity of the liquid resin she was able to introduce mobility together with a damage trigger into a classic engineering material. When cracks form in this material, they also rupture some of the embedded reservoirs. As a result of capillary forces the resin spreads itself through the created cracks and hardens in contact with air, repairing the damage. This system is completely autonomous and does not need human intervention. The successful concept was extended to polymers[12] not long after that. Motuku *et al.* were the first to create a self-healing fibre reinforced polymer composite using (*ca.* 1 mm in diameter) resin filled fibres inside the matrix material.[13] They investigated the effect on the mechanical properties after healing with variation in the fibre size, their amount and the type of resin used. Bleay *et al* refined the idea of using hollow fibres in a fibre composite material and sized down the capillary diameter (*ca.* 15 μm) in

order to reduce their negative influence on the intrinsic material properties.[14] However, a reduction in the fibre diameter resulted in an increase in capillary forces, thereby making the deployment and preparation of the fibres more difficult and labour intensive. The development of liquid-based self-healing composites was advanced by Bond and coworkers in recent years.[15–17]

In 2001 a slightly modified concept was demonstrated by White and co-workers, replacing the expensive liquid-filled fibres by spherical microcapsules and introducing a healing mechanism based on an encapsulated liquid diene monomer (dicyclopentadiene) plus a separately dispersed solid catalyst (1st generation Grubbs).[18] Upon fracture, the released monomer comes in contact with the dispersed catalyst and commences a living ring-opening metathesis reaction (ROMP) which creates a tough polymer at the crack-site. Since then, the field of self-healing polymers based upon liquid healing-agents has evolved steadily and the liquid-based concept was picked up by many others, optimising it for different types of applications, *e.g.* composites and coatings.

All the demonstrated systems rely on the safe storage over a long period of time of at least one reactive liquid compound (in capillaries or spherical microcapsules) and in most cases also on the dispersion of a second reactive compound that is either in liquid or solid form. Schematics of the different systems can be found in Figure 1.3

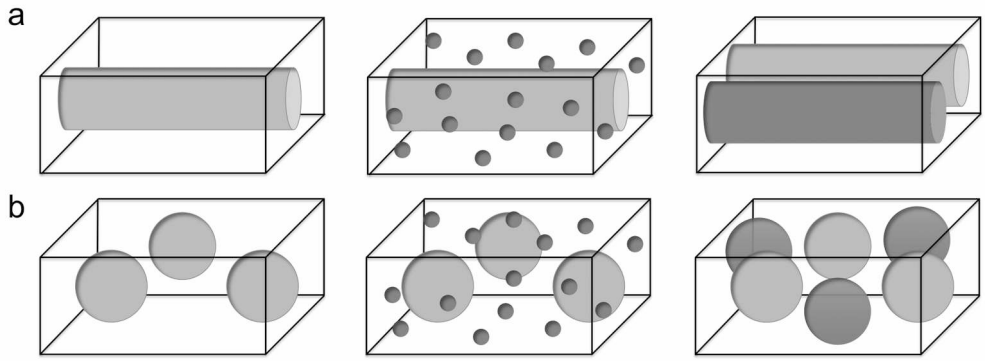

Figure 1.3: Schematic of the encapsulated liquid configuration (in combination with a second solid/liquid reactive component); a) for continuous capillaries; b) for spherical microcapsules

In the continuing optimisation and innovation of the liquid-based systems two key features are addressed. The first is the change of healing mechanism. In these studies the liquids and/or catalysts from the earlier demonstrated systems are replaced by more robust, faster and more effective compounds. Other aspects such as environmental friendliness and costs play a role as well.[19] Examples of such advancements are systems based upon the catalysed cationic polymerisation of epoxy functionalised monomers,[20] the catalysed polycondensation of polydimethylsiloxane[21] and the curing of a two component liquid epoxy resin with the use

of mercaptans.[22] All of these presented systems have demonstrated their excellent healing after fracture. However, these binary systems all strongly rely on the contact and/or simultaneous release of the two dispersed components.

The second feature involves the development of different containers for storing the liquid healing agent inside the material, but only represents a small fraction of the current work on liquid-based self-healing today. Capillaries and microcapsules were initially only designed to contain the latent liquid healing-agent inside and prevent it to make contact with either the matrix or the second dispersed reactive component until the moment of matrix cracking. A major drawback however of these compartmentalised liquid-based systems is that healing-agent can only be released on a single occasion and secondary cracking of an earlier damaged site cannot be repaired. For this reason novel container design mainly focusses on the development of a continuous biomimicked microvascular system, by which the liquid can be replenished to earlier damaged sites.[17,23] Regardless of the design, the liquid containers however should have a) sufficient stability over time to protect the encapsulated phase as long as is necessary; b) a high fracture probability to rupture accordingly the matrix; and c) a facile production route for production on a large scale in order to be used in an application. Surprisingly, only a few researchers have reported on advancements on each of these three points since the introduction of liquid-based self-healing materials 15 years ago.

1.4 Scope and outline of the thesis

Inspired by the current state-of-the-art and the progressing advancements in the field of self-healing materials, this thesis addresses several novel routes to advance the concept of liquid-based self-healing polymer systems.

This thesis presents the concept and characterisation of a one-component solvent-based healing mechanism for thermoplastic materials and in addition to the healing strategy, a new capsular architecture is proposed for the purpose of simultaneous release of two reactants at the same location. Other liquid container designs are investigated to enhance the liquid release upon fracture (also in the case of multiple healing events) and come with less scarification of the intrinsic material properties.

Chapter 2 describes the theoretical and experimental evaluation of all the material system parameters that are significant in the performance of a one component solvent-induced self-healing mechanism for thermoplastic materials. Parameters that are investigated include solvent sorption rates, solvent-induced depression of T_g and polymer diffusion coefficients.

In *Chapter 3* autonomous solvent-induced self-healing mechanism for PMMA are presented and investigated. The self-healing of the mechanical properties is experimental validated for different solvents and capsule volume concentration as a function of the healing time.

In *Chapter 4* the capsule-composite thermoplastic self-healing material is characterised qualitatively and quantitatively by X-ray tomography using SEM-based and Synchrotron X-ray facilities. The techniques allow detailed investigation into the release volume and kinetics of healing-agent at the damaged site.

Chapter 5 presents a novel microcapsular architecture, designed for the encapsulation of two individual liquids within a single microscopic structure. These binary microcapsules have a central liquid core and are peripherally decorated with the second liquid component, which is achieved by the synthesis and application of liquid-filled Pickering particles.

Chapter 6 presents a numerical study into the influence of the microcapsule geometrical shape on the performance of a self-healing material. Classical spherical shapes are compared to cylindrical ones with varying degree of anisotropy and spatial orientation.

In *Chapter 7* production routes are evaluated to obtain anisotropic rod-like microcapsules. The investigated routes involve droplet deformation and encapsulation in shear and elongational flow, by usage of a modified ink-jet printing technique and by creation of stable anisotropic droplets in suspension using Pickering particles.

In *Chapter 8* the concept for a compartmented liquid-filled fibre is given, providing an alternative to the continuous capillaries and discrete spherical microcapsules currently applied in the field of self-healing. Control over the morphology allows production of fibres with different mechanical properties that are in the order of standard composite matrix materials and have slightly lower failure strains.

CHAPTER 2

Solvent sorption and welding of thermoplastics

It is the theory which decides what we can observe.

Albert Einstein

2.1 Introduction

Since the introduction of liquid-based self-healing polymer materials, a substantial amount of work has been focused on two-component repair systems for thermosets.[15,18,21,24] The systems that have been presented up to now either comprise a single encapsulated liquid in combination with a dispersed catalyst[18,24] or two separately encapsulated liquids.[16,21] Both systems rely on the fact that the initially separated reactive chemicals are released or exposed by the same damage event and make contact somewhere on the crack surface, preferably near the crack tip. A disadvantage of these two-component systems is the requirement for the simultaneous release of the reactants (in stoichemeometric ratios) as well as in close proximity of each other. In order to overcome such limitations a one-component liquid healing strategy would be preferable.

Recently, non-reactive organic solvents were introduced as a one-component healing-agent for cured epoxy materials.[25,26] Although solvents mobilise the polymer segments at the surface of the epoxy matrix material in order to repair the crack in the thermoset, healing is essentially established *via* reaction of still present un-reacted functionalities.

[0]Based on: S.D. Mookhoek, H.R. Fischer and S. van der Zwaag, *in prep.*, 2010

Repairing cracks in thermoplastic polymers using solvents as an external healing stimulus is a known method and has been reported earlier.[27,28] Fractured thermoplastic materials can be welded by wetting the two surfaces with a suitable solvent and bringing them together (at elevated temperatures). The solvent swells the polymer matrix and as a consequence the polymer applies pressure to the interface of the two joined fractured parts and seals the interfacial space. Due to a solvent-induced reduction of the glass transition temperature, the polymer chain mobility at the interface is largely increased and polymer reptation occurs across the interface.[29–31] The local T_g is restored upon evaporation and/or diffusion of the solvent, freezing-in the newly formed entanglements to weld the two crack-faces. Analogue to solvent welding, a one-component solvent-based strategy can be designed for the design of a self-healing thermoplastic material.

Hence, in this thesis the design of a one-component solvent-induced self-healing mechanism is presented for amorphous linear thermoplastics, solely based on the activation of polymer reptation and re-entanglement. In this chapter the potential of solvent-induced healing of thermoplastics was investigated focussing on the determination of desirable solvent characteristics. Commonly used polymer solvents were selected on the basis of their physical properties and their interaction with the polymer material. The selected solvents were evaluated for future employment as solvent healing agents by solvent sorption and welding experiments, introducing the solvent manually. In the next chapter the deployment of the concept using encapsulated solvents is addressed.

2.2 Solvent selection

The topic of solubility of polymers has been widely studied.[32–34] Whether a certain polymer is soluble in a given solvent, depends on different factors: such as polarity, molecular weight, degree of branching/crosslinking, crystallinity, temperature, etc.[35] The polymer solubility is determined by the number and type of molecular interactions between the polymeric backbone and the solvent molecules. Small changes in the polymeric chain can already lead to significant changes in molecular interactions and thus can convert a soluble polymer to an insoluble one. Hence, in the case of solvent-induced healing of thermoplastic materials the choice of solvent will highly depend on the nature of the polymeric material used.

Amorphous thermoplastics have low solvent resistance in comparison to semi-crystalline polymers. Fully amorphous materials allow solvents to be absorbed quickly, this because of their relative large free volume in the solid state. In contrast, semi-crystalline materials have high fractions of crystalline phase, which have much higher solvent resistivity at ambient conditions. In order to dissolve the crystallites, an energy barrier has to be overcome first to allow these polymers to be dissolved. In common practice this can only be achieved using suitable solvents at much higher temperatures. Solvent welding at ambient temperatures is therefore only applied to amorphous and not to semi-crystalline thermoplastics. The latter

are generally welded by welding procedures that imply heat, *e.g.* IR-, microwave-, laser-, hotplate welding, etc.[36,37]

In order to find a suitable solvent for an amorphous polymer, Hansen proposed a versatile solubility parameter that provides a quantitative measure for the degree of interaction between the solvent and the polymer.[38] In addition to the more general Hildebrandt solubility parameter,[39] the Hansen solubility parameter not only accounts for dispersive interactions but also takes into account polar and protic interactions. The total solubility parameter of a substance, δ, is defined as follows:

$$\delta^{tot} = \sqrt{\left(\delta^d\right)^2 + \left(\delta^p\right)^2 + \left(\delta^H\right)^2} \tag{2.1}$$

wherein the superscripts d, p and H denote the dispersive, polar and H-bonding interactions respectively. The individual contributions of the different interactions for many molecules can be found in literature.[39] The Hansen solubility parameter is defined such that materials with comparable Hansen solubility are likely to be miscible.[38]

For polymers Hansen not only defined a solubility parameter, he also suggested a 'sphere of solubility' to predict whether a particular solvent/polymer combination is miscible. The radius of that sphere, R_0 varies with the selection of the polymer. Depending on their properties, solvents can be found inside or outside this sphere radius, suggesting either miscibility or inmiscibility. The sphere of solubility is much more accurate than comparing total solubility parameters as it compares dispersive, polar and protic interactions bilaterally. The position of solvents within the sphere, R_a for a particular polymer material is given by the following equation:

$$R_a = \sqrt{4\left(\delta^d_{pol} - \delta^d_{sol}\right)^2 + \left(\delta^p_{pol} - \delta^p_{sol}\right)^2 + \left(\delta^H_{pol} - \delta^H_{sol}\right)^2} \tag{2.2}$$

wherein the subscripts *pol* and *sol* denote the polymer and the solvent respectively.

By taking the ratio of the two radii the predicted solubility is normalised:

$$J = \frac{R_a}{R_0} \qquad \begin{cases} J > 1 & \text{unlikely to be miscible} \\ J = 1 & \text{likely to be partly miscible} \\ J < 1 & \text{likely to be miscible} \end{cases} \tag{2.3}$$

Besides the solvent quality, other parameters such as diffusion coefficient, vapour pressure, viscosity and surface tension are considered to be important in the evaluation of suitable solvents for solvent assisted healing. The diffusion coefficient together with the volatility of the solvent will determine the time characteristics in which the solvent is able to weld the

two crack surfaces. The volatility of the solvent however might change when the solvent is absorbed by the polymer. The solvent viscosity is another parameter that should be evaluated since higher viscosities will prevent the solvent healing agent from spreading inside the crack or only over large time intervals. The surface tension of the solvent will determine spreading of the liquid over the crack faces and allows uniform healing of the interface. With these considerations a first selection of suitable solvents was made on the basis of solvent quality (R_a/R_0) and volatilty (vapour pressure). In Figure 2.1 two diagrams of the vapour pressure versus the ratio of solubility radius are given for polymer solvents; a) for polystyrene (PS) and b) for polymethylmethacrylate (PMMA).

Many of the indicated solvents for PS and PMMA have a value for J that is smaller than unity, indicating them as suitable solvent healing-agents. However, there is a large difference between the vapour pressure of these solvents. For example acetone and dioctylphthalate in either of the two plots have comparable values for J but differ largely in vapour pressure. Because of the difference in vapour pressure these solvents are expected to exhibit dissimilar healing potential. In order to study the effect of solvent quality and volatility on the welding characteristics, good solvents ($J < 1$) and poor solvents ($J \approx 1$) with a high range in vapour pressure (10^{-1}–10^{-5} bar) were selected in this investigation. Based on Figure 2.1 toluene, decalin, PAc, NMP, o-DCB and dioctylphthalate were chosen as solvent welding agents for PS and PMMA. The viscosities of these solvents are low at room temperature, of the order of 1 $mPa.s$.

2.2.1 Solvent-induced depression of T_g

When solvents are applied on polymer surfaces to be healed or welded, solvent uptake by the polymer will lower the local glass transition temperature (T_g) of the material. The T_g has to be reduced to a value below ambient temperature in order to establish sufficient mobility of the macromolecules and obtain healing when the two material surfaces are brought in contact. The reduction of the T_g depends highly on the type of solvent and its volume concentration. Elaborate work on the glass transition temperature as function of solvent volume concentration has been presented in literature and provides a tool for the prediction amount of the solvent needed to reach a T_g below room temperature.

For homogeneous multi-component polymer blends Fox and Flory[40] developed a function for the overall T_g on the basis of the intrinsic polymer glass transition temperatures values and the volume fractions of the polymers:

$$\frac{1}{T_g} = \sum_i \frac{x_i}{T_g^i} \tag{2.4}$$

Later, Fox[41] demonstrated that the given expression as a rule of mixtures not only applies to polymer blends but also appeared valid for solvent-polymer systems. It implies however

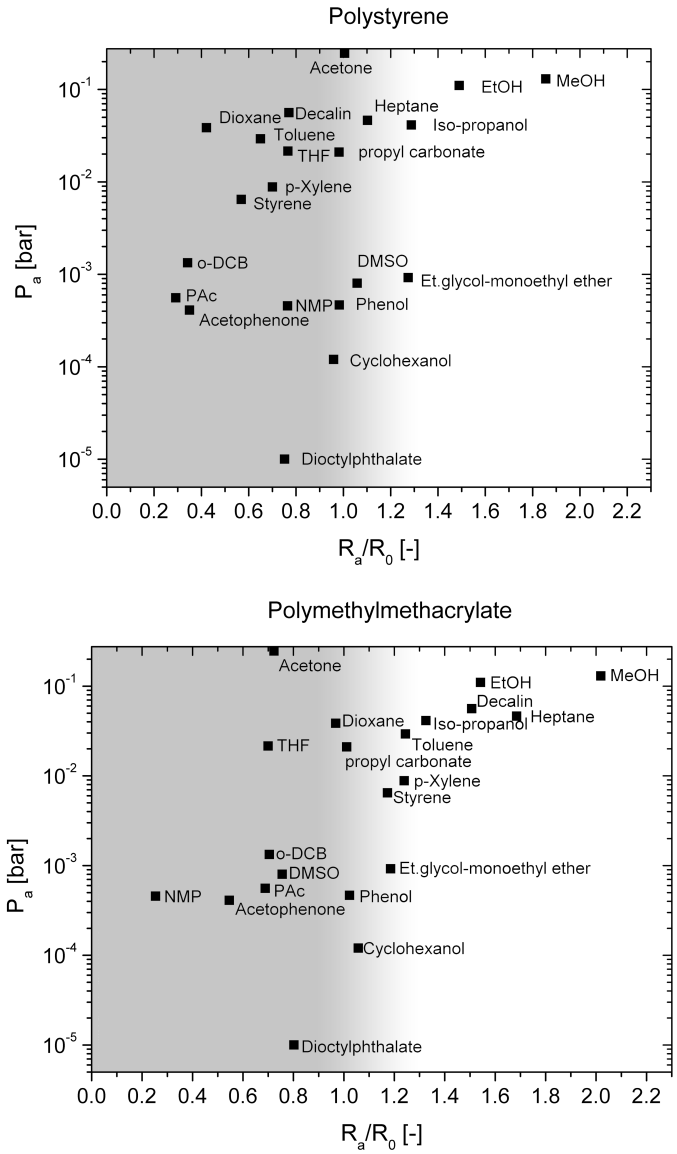

Figure 2.1: Solvent healing-agent map for a) polystyrene and b) polymethylmethacrylate indicating the vapour pressure (P_a at 25^oC) versus the solvent quality of many common solvents (R_a/R_0). DMSO: dimethylsulfoxide, PAc: phenyl acetate, o-DCB: ortho-dichlorobenzene, NMP: 1-Methyl-2-pyrrolidinone, THF: tetrahydrofuran, EtOH: ethanol and MeOH: methanol. The shaded area indicates the good solubility range ($R_a/R_0 < 1$) of the polymer

defining or measuring an intrinsic T_g of the solvent. This temperature can be determined by fitting the Fox-Flory equation to experimental data on the overall glass temperature as function of the solvent volume fraction. In Figure 2.2 it is demonstrated that the Fox-Flory theory approximates experimental data by Kambour *et al.*[42] on a DCB/polystyrene system fairly accurately at lower solvent volume fractions (with the intrinsic T_g as the only fitting parameter). With help of the fit in Figure 2.2 an intrinsic T_g of 130.1 K (-143^{o}C) was found for DCB. Rauch *et al.* determined the T_g of Tol similarly for polystyrene and found a value of 117 K for the solvent.[43] From experimental results of Chow and Ferry for the function of T_g for PS/solvent mixtures the T_g of PAc ($\approx$ 167 K) was estimated on the basis of data on methyl salicylate.[44,45] Figure 2.2 shows estimates of the T_g of PS/solvent systems as a function of Tol and PAc fraction following eq. 2.4.

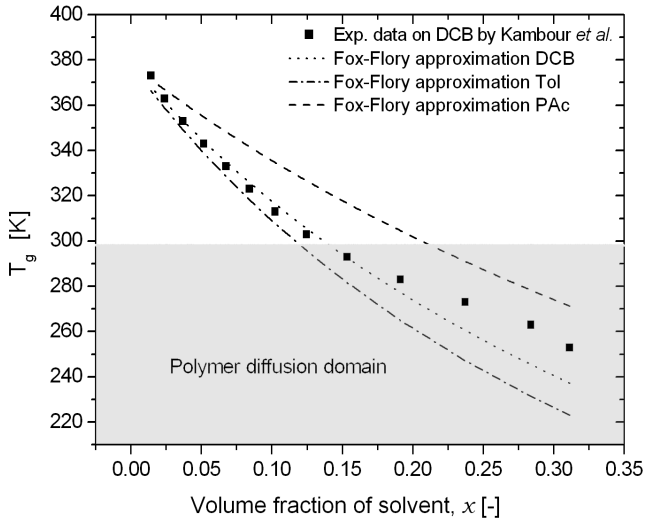

Figure 2.2: Estimates for the glass transition temperature (T_g) of Polystyrene/solvent systems as function of the volume fraction of DCB, Tol and PAc (x) following eq. 2.4

Figure 2.2 shows that a volume fraction of approximately 16 vol% of DCB is needed to reduce the polystyrene's T_g from its intrinsic value of 378 K to room temperature (298 K). For Tol and PAc critical volume concentrations of 13.5 % and 29 % are found, respectively. Hence, the local solvent fraction at the solvent treated surface must exceed this value so that polymer diffusion across the interfaces is stimulated.

The T_g is recovered to values above room temperature in time, since removal of the solvent from the surface by evaporation and or diffusion is unavoidable (as well as desirable for self-healing and property restoration). The crossing of T_g interlocks the newly entangled macromolecules and creates a weld between the two interfaces. For example, at only a small

reduction of the solvent fraction (5%) of DCB the T_g of polystyrene already increases by 25 K to a value of 50^{o}C, for an initial concentration of 13%.

2.2.2 Polymer sorption and diffusion

The absorption of a suitable solvent by a polymer substrate is thermodynamically controlled and the driving force is given by the difference in chemical potential between the solvent and the solvent intruded film. When an excess of solvent is applied, the penetration of the solvent should continue up to a homogeneous level of solvent throughout the matrix material. For the systems under investigation here, only a limited amount of solvent is available and a stabilisation of the solvent penetration front is expected when all the available solvent is absorbed by the plastic material.

Since both solvent sorption and solvent evaporation from the material are time dependent, time is an important parameter in the solvent assisted healing studies. In order to establish optimal solvent assisted healing over a large area the following qualitative equation can be formulated:

$$t_{spr} < t_{abs} < t_{evap} \tag{2.5}$$

in which t_{spr}, t_{abs} and t_{evap} are the time required for of solvent spreading, solvent absorption and solvent evaporation respectively.

The period of increased mobility of the polymer chains in the solvent penetrated layer (when $T_g <$ ambient temperature) should exceed the time required for sufficient polymer diffusion across the interface. For optimal welding of two surfaces the following should be valid:

$$t_{pdif} < t_{evap} + t_{sdiff} \tag{2.6}$$

in which t_{pdif} is the time required for polymer diffusion across the two materials' interface, $t_{evap} + t_{sdiff}$ is the time until the solvent concentration drops below the the critical value of T_g (either by evaporation or diffusion) at which the polymer is immobilised.

Polymer diffusion at temperatures above the glass transition temperature by intrusion of solvent can be described by the diffusion of polymer chains in a concentrated polymer solution.[46–48] Diffusion in polymers has primarily been based on Eyring's free volume theory.[29] The free volume theory assumes that molecular transport within a polymer proceeds through the creation of holes between the chains and that molecules 'leap' from hole to hole through the material. Cohen and Turnbull.[30,45,49,50] demonstrated that free volume theory also applies to polymer solutions when assuming that there is sufficient polymer to polymer interaction. This is assumed to be the case in a highly entangled concentrated solution. An estimate for the critical polymer weight fraction at which the free volume theory is still

assumed valid was proposed by Berry and Fox:[51]

$$\omega_p^* = \frac{4}{1 + 0.2\,(M_w)^{\frac{1}{2}}} \tag{2.7}$$

wherein ω_p^* is the critical weight fraction of the polymer and M_w is the molecular weight of the polymer.

The diffusion of a polymer chain through a solvated polymer network of entanglements is restricted by the presence of other chains. The resistance or friction that controls the diffusion of the macromolecule is a very complex function and difficult to describe precisely. However, Ferry[45] demonstrated that when assuming an average friction coefficient for the polymer chain, the polymer diffusion can be correlated to the friction coefficient, ζ, in Stokes' law in fluid dynamics $[N/\left(m/s^2\right)]$. Through Debye's free draining model for viscosity, Bueche[52] demonstrated that the diffusion of polymer molecules (D) decreases with increasing degree of entanglement for polymers with molecular weights higher than the average molecular weight of entanglements.

$$D \propto \left(\frac{M_e}{M_w}\right)^{2.5} \tag{2.8}$$

in which M_e is the average polymer molecular weight between entanglements and M_w is the polymer's average total molecular weight.

Eq. 2.8 shows that the degree of entanglement highly influences the polymer diffusion and that the diffusion will therefore be a function of the polymer rigidity. The relation between ζ and the polymer diffusion coefficient is derived from Einstein's equation for diffusion:

$$\zeta = kT/D \tag{2.9}$$

in which k is Boltzmann's constant, T is the temperature and D is the diffusion coefficient. It shows that the polymer diffusion is linearly proportional to the reciprocal viscosity. When concerning small objects, such as a small sphere, ζ is simply defined by the geometry of the object (radius: r) and the medium viscosity, η:

$$\zeta = 6\pi\eta R \tag{2.10}$$

For polymers the function of ζ is much more complex. However, Vrentas developed an approximation based on the 'geometrical' parameters of a polymer chain in a concentrated solution:

$$\zeta = \frac{36\eta_p Mw}{\rho N_A \langle R^2 \rangle} \tag{2.11}$$

wherein ρ is the polymer mass density, $\langle R^2 \rangle$ is the mean square end-to-end distance of the chain and N_A is Avagadro's number.

The diffusion coefficient of polymers can be determined experimentally *via* methods such as neutron reflectivity measurements (NRM),[53] nuclear magnetic resonance (NMR)[54] and positron annihilation lifetime spectrsocopy (PALS).[55] However, based on eq. 2.11 the diffusion coefficient can additionally be determined indirectly through simple viscosity measurements on concentrated polymer solutions. The value of the diffusion coefficient for a given polymer/solvent combination can also be predicted rather accurately using polymer free volume theory:[47]

$$D_s = D_0 exp\left(\frac{-\gamma\left(\omega_s \hat{V}_s^* + \xi\omega_p \hat{V}_p^*\right)}{\hat{V}_{FH}}\right) \tag{2.12}$$

$$D_p = \frac{A}{Mw\,(N^*/N)} exp\left(\frac{-\gamma\left(\omega_s \hat{V}_s^* + \zeta\omega_p \hat{V}_p^*\right)}{\zeta\hat{V}_{FH}}\right) \tag{2.13}$$

in which D_s and D_p are the respective diffusion coefficient for solvent and polymer. D_0 and A are the pre-exponential factors and can be determined experimentally or can be found in literature. The parameter γ is the so-called overlap factor taking into account the fact that the same holes in the free volume theory can be occupied by both the solvent and the polymer. The solvent and polymer weight fractions are denoted as ω and $\hat{V}^*$ is the critical volume at 0 K of the hole for either the solvent or the polymer that allows transport.[50] $\hat{V}_{FH}^*$ is the total hole free volume and ξ is the ratio of the molar volume of the jumping unit of the solvent to that of the polymer.

Both ζ and $\hat{V}_{FH}^*$ for the polymer are functions of temperature. The temperature dependence of the pre-exponential factors is small enough for them to be treated as a constant. The total free hole volume for the solvent/polymer combination, $\hat{V}_{FH}^*$, can be expressed as a function of temperature and specific system constants (K_{ij}) which are both related to the polymer and solvent WLF constants:[46,47]

$$\frac{\hat{V}_{FH}^*}{\gamma} = \omega_s\left(\frac{K_{11}}{\gamma_s}\right)\left(K_{21} - T_{g(s)} + T\right) + \omega_p\left(\frac{K_{12}}{\gamma_p}\right)\left(K_{22} - T_{g(p)} + T\right) \tag{2.14}$$

Now, when the values for K_{11}, K_{12}, K_{21}, K_{22} and ξ are known, the diffusion coefficients can

be predicted for solvent and various molecular weights of polymer at different temperatures. Subsequently, the time required for polymer chains to migrate across the interface in order to dissolve it is given by the reptation time, τ:

$$\tau_{rep} = \frac{L^2}{D_p} \tag{2.15}$$

wherein L is the length over which the polymer chains will have to diffuse in order to achieve bulk-like properties. For glassy polymers such as PS and PMMA it was experimentally found that this distance is in the order of 50-100 nm.[56]

2.3 Experimental

2.3.1 Materials

The solvents o-dichlorobenzene (DCB), phenyl acetate (PAc), cis-decahydronaphthalene (Decalin; Dec), 1-Methyl-2-pyrrolidinone (NMP), dioctylphthalate (DOP) and toluene (Tol, tech. 80%) were purchased from Sigma Aldrich and were used as received. DOW Styron® 638 grade polystyrene (PS, GPC: M_n = 66130 Da, PDI = 2.79), was kindly donated by DOW Benelux, The Netherlands and was used as received. Diakon® Polymethylmethacrylate (PMMA, GPC: M_n = 50520 Da, PDI = 2.81) was received from ICI and was dried under vacuum at 50^{o}C prior to use. Dibenzoyl peroxide (BPO), a radical initiator (Sigma Aldrich, 75% pure), was recrystallised from methanol and air dried prior to use.

2.3.2 Evaluation of solvent-thermoplastic combination

The solvent absorption and the rate of solvent penetration as function of time for different polymer-solvent combinations was measured by microindentation. The evaporation of the solvent is assumed to be a critical factor for the time required to establish a good weld between surfaces of material. Hence, in these indentation experiments, solvents were not positioned between two material surfaces but were applied on open surfaces. The latter allows the investigation of the initial solvent intrusion and the subsequent removal by evaporation and/or diffusion. Thin plates (*ca.* 1 mm) of PS and PMMA were wetted with a small drop of solvent (*ca.* 5 μm) for a given time (see Figure 2.3 (1)), during which the sample was covered with a glass to reduce evaporation. After this time the excess of solvent on the surface was removed by a cotton tissue using the capillary action of the fabric. The 'wet' samples were directly placed inside a UNAT automated indentor (Asmec GmbH) and indentations were performed applying 100 mN of force using a Berkovich diamond tip at regular time intervals (Figure 2.3 (2)). After indentation the samples were allowed to dry and were probed again.

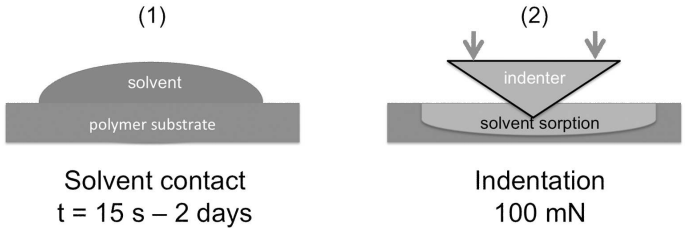

Figure 2.3: Experimental procedure for solvent sorption (1) and indentation experiments (2)

2.3.3 Solvent wetting

The degree of solvent wetting was determined by measuring the solvent-polymer contact angle using a CAM200 Optical tensiometer from KSV Instruments. For the determination of the contact angle, 5 μl droplets of solvent were placed on a smooth polymer surface at a rate of 1 mm/min and the contact angle was allowed to equilibrate in time. Images of the droplet were recorded each at 1.3 frames s^{-1} and when the droplet shape appeared stable, the contact angle was determined as the average contact angle (left and right) from 5 sequential images.

2.3.4 Mechanical evaluation of solvent selection for polymer welding

The ultimate potential of selected solvents as solvent healing-agent to heal cracks in amorphous thermoplastic materials was evaluated using lap-shear tests. Two equally shaped samples with a plate geometry, according to ASTM standard D3163, were welded together using 0.023 $\mu l/mm^2$ of the solvent of choice. The tested sample geometry is shown in Figure 2.4 which has a welded overlap of 25.4 mm. The welded samples were clamped with a load of 5 N and stored in a fume cabinet. There they were allowed to dry for 2 or 10 days. The welded samples were tested at a displacement rate of 5 mm/min using a Zwick/Roell 20 kN tensile load frame under displacement control.

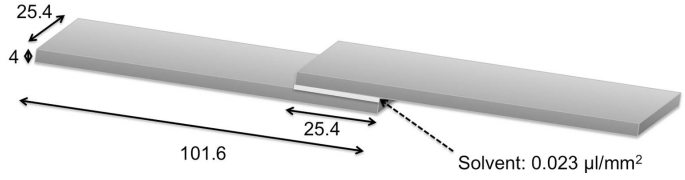

Figure 2.4: Lapshear test geometry used for solvent evaluation (dimensions in mm)

2.4 Results

2.4.1 Solvent intrusion behaviour

Representative indentation curves for DCB penetration in PS and PMMA are given in Figure 2.5a and 2.5b. The penetration of DCB, PAc and Tol into PS and PMMA as a function of time are given in Figure 2.5c and 2.5d respectively.

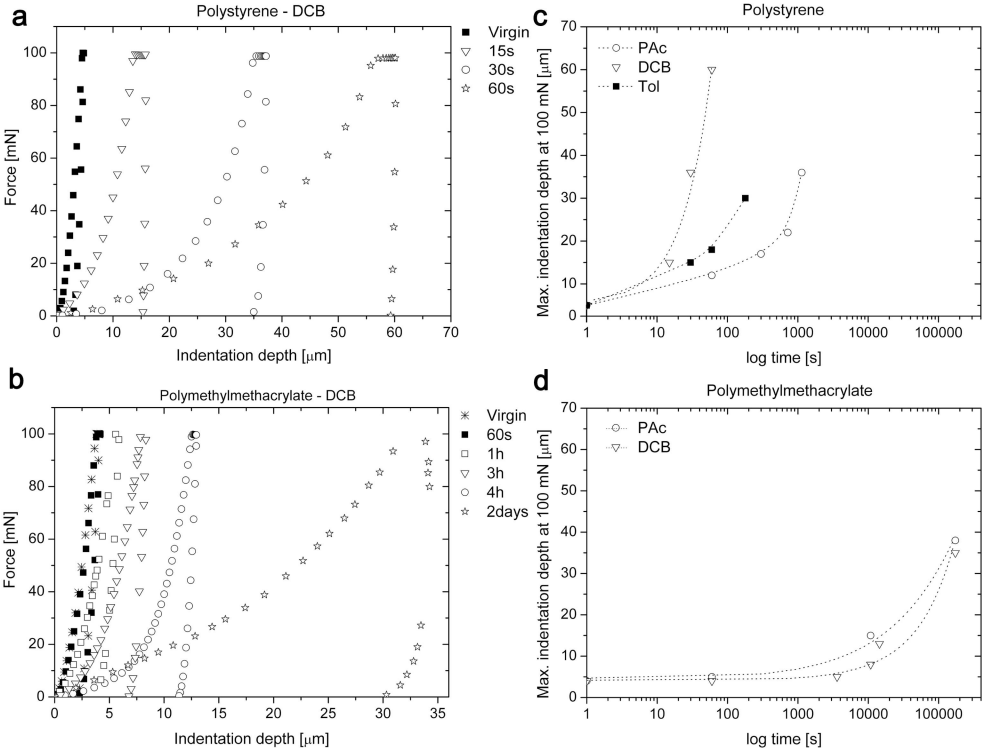

Figure 2.5: experimental results for microindentation tests after solvent sorption. Representative indentation curves after sorption of DCB in PS and PMMA are presented in (a) and (b) respectively. Figures (c) and (d) show the maximum indentation depths at 100 mN force as function of time for different solvents in PS and PMMA

Figure 2.5a demonstrates that DCB for the conditions used penetrates PS up to a depth of 50 μm in less than 1 min, indicating a large plasticized volume under the surface. The shape of the indentation curves change slightly as function of solvent contact time. The difference is mainly found in the initial part, as the modulus of the top layer of the PS decreases with absorption of solvent. The T_g of PS rapidly decreased up to a large depth inside the polymer. The penetration of DCB in PMMA (Figure 2.5b) however is much slower (order

of hours). Similar to PS the curves for PMMA show a change of the material top layer's compliance as function of solvent contact time. However, the results indicate that the time required for lowering the T_g for PMMA below room temperature is substantially larger than that of PS and hence longer healing times should be presumed for PMMA.

The other two investigated solvents, PAc and Tol, exhibit comparable behaviour as DCB for both materials. Both Tol and PAc penetrate PS within minutes, whereas for PMMA hours are required to reach penetration depths in the order of tens of microns. The kinetics of penetration however differ slightly with varying solvent. In PS the rate of intrusion of solvent appears to scale down as follows: DCB < Tol < PAc. This sequence most probably is the effect of the difference in polarity and negative effect of proticity of the PAc as it wants to penetrate the PS.

Additional indentation experiments as a function of subsequent drying time show that the penetration depth of solvent decreases and intrinsic indentation behaviour is restored within days for DCB and PAc. From the indentation curves it is additionally observed that Tol rapidly evaporates. Within minutes after removing the excess of solvent from the surface, the top layer of the polymer appears to harden and re-establishes a stiffness similar to the unintruded substrate. The latter is shown in the indentation curve in Figure 2.6. The three stiffness regimes are indicated by the slopes of the dotted lines. The initial slope of the curve resembles that of the third and approximates the stiffness of the non-absorbed virgin PS. The reduced slope in the center of the curve represents the solvent induced depression of modulus due to transition of the T_g below room temperature.

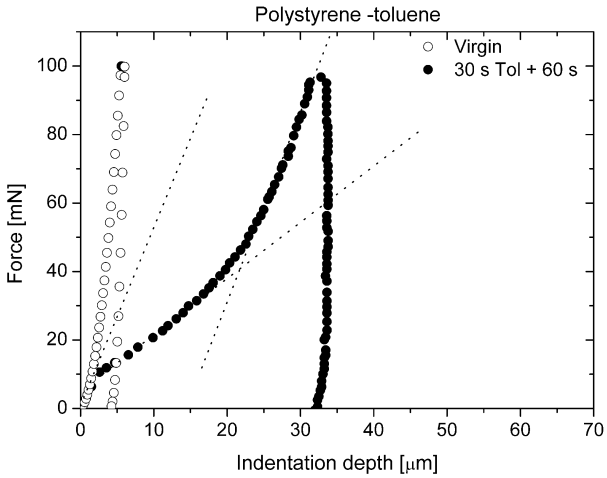

Figure 2.6: Experimental results for microindentation tests after toluene sorption (contact time 30 *s*) and waiting time, 60 *s* in comparisson to the indentation of virgin PS.

2.4.1.1 Solvent-polymer wetting

The results of the contact angle measurements for PS and PMMA in combination with DCB and PAc are presented in Figure 2.7.

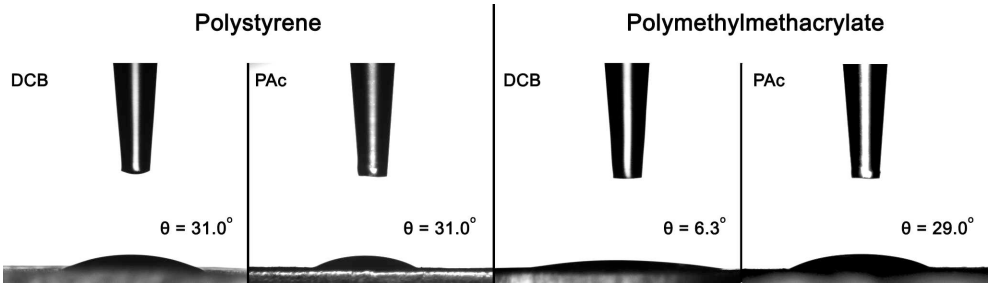

Figure 2.7: Measurments of solvent wetting behaviour on PS and PMMA

In Figure 2.7 the last recorded image for each experiment is given (7.5 *s* after droplet placement). The calculated average stabilised contact angle is denoted in the right bottom corner of the image. The results show that both solvents have relative good wetting properties versus the two polymer materials but spreading is minimal. PAc shows a comparable contact angle for both studied materials: approximately 30^o. A similar value for the contact angle has been determined for DCB on PS. On the other hand the chlorinated solvent has a much smaller contact angle on PMMA and the solvent spreads itself freely over the surface. The good spreading of DCB on PMMA is most probably the effect of the high polarity of this solvent in combination with the polar PMMA substrate and the low rate of sorption of solvent into the material.

2.4.2 Solvent-welded lapshear tests

The results of the welded PS and PMMA substrates' lapshear experiments, using selected solvents: DCB, PAc, DOP, Dec, Tol and NMP, are presented in Figure 2.8. From the figure it can be observed that the strength of the weld created highly depends on the type of material-solvent combination. Besides the type of polymer-solvent combination, time also appears to be a significant factor in the case of PMMA for the welding quality.

Over the whole range of selected solvents, NMP and Tol result in the highest weld strength after a period of two or ten days for both type of materials, despite the fact that toluene can be found outside the PMMA's Hansen solubility sphere. However, rather than dissolving the polymer, the solvent is able to swell the polymer and increase molecular mobility at ambient conditions to a sufficient degree. Hence, the solvent is able to establish a strong weld.

In case of PS, almost similar results are obtained for all the selected solvents when comparing the mutual results for 2 and 10 day respectively. Moreover, the recorded weld strength for PS using DCB, Tol and NMP even exceeded the intrinsic material strength, since material fracture was observed before the weld detached. Both observations indicate that for polystyrene solvent uptake and polymer bridging is a relatively fast process, showing its potential for self-healing purposes.

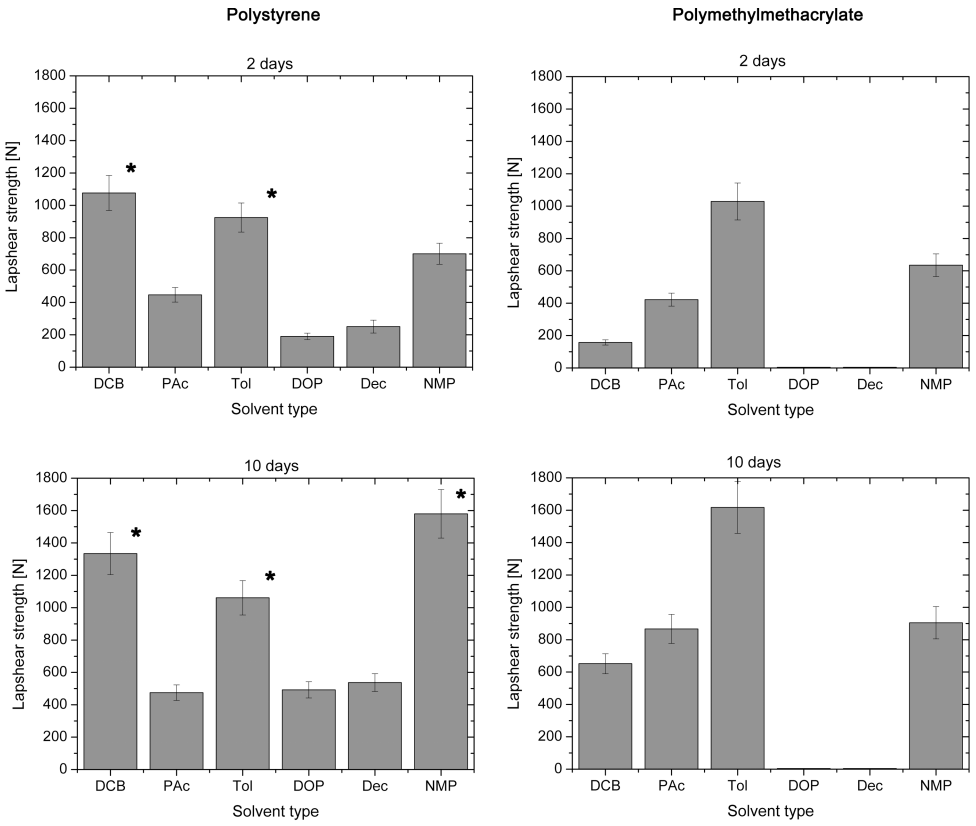

Figure 2.8: Lapshear strength results of PS (left column) and PMMA (right column) welded samples with 0.023 $\mu l/mm^2$ of a selected solvent. Samples were allowed to 'dry' for 2 (upper row) or 10 days (bottom row). The asterisks indicate that the lapshear strength exceeded the materials strength and that the samples fractured outside the welded area.

The required time to obtain high lapshear strength values for PMMA is generally found to be much longer. In comparison to the volatile Tol, only poor solvent welding is observed after two days with PMMA for the low vapour pressure solvents: DCB, PAc, DOP and NMP.

In the case of these solvents, the detached samples show a plasticised zone were the solvent was applied and the welded interface shows rubber-like behaviour in the failure regime of the test. Solvent concentrations are still relatively high and the polymer T_g is still assumed to be below room temperature (Figure 2.2). Dec does not show any effect of solvent welding for PMMA in a period of 2 days, wehereas DOP shows evidence of solvent welding but the weld is still plasticized. The three solvents with vapour pressures around 10^{-3} *bar*: DCB, PAc and NMP show largely increased values for the shear strength of the welded area in 10 days aging time, as the removal of the solvent from the welded area appears to be crucial. DOP, with a much lower vapour pressure, requires even longer times as the remaining DOP after 10 days still largely plastisizes the weld. Again for Dec no proof of welding was observed. Only a high vapour pressure solvent such as Tol appears to be able to establish a strong weld in only a short period of time.

2.5 Discussion

The results of the indentation experiments have shown that sorption of similar solvents behaves significantly different in PS and PMMA. Since the welding experiments show comparable behaviour as the indentation experiments, it indicates that the diffusion of polymer and solvent governs the welding process. The diffusion for each of the two materials is expected to vary due to their difference in polymer chain structure and morphology.

The diffusion of the polymers within the top-layer of solvent absorbed material may be predicted as function of solvent fraction. Although relative high concentration of solvents are present in the interface layer of the material, eq 2.7 shows that for a polymer with a M_w of 2x10^5 g/mol the free volume theory still applies up to a solvent weight fraction concentration up to 95%. Hence, according to the theory, the diffusion coefficient for the solvent and polymer may be predicted by eq. 2.12 and eq. 2.13. For a representative system of PS/toluene the necessary free volume parameters can be found in literature[47,57] and are presented in Table 2.1. Additional physical data on the polystyrene grade used, have been added to the table.

The diffusion coeffecient of the solvent and polymer are derived for temperatures of 298 K and 323 K as a function of solvent weight fraction with the values from Table 2.1; these curves are given in Figure 2.9.

The curves starts at a weight fraction of about 12%. At this particular weight fraction (Figure 2.2) the solvent/polymer mixture's T_g equals a value of 298 K. The diffusion coefficient (298 K) at this fraction is 1.7 x 10^{-22} cm^2/s. This is the minimal diffusion rate at which the polymer chains can migrate from one side of the interface to the other at the given temperature. When assuming that the distance to bridge the interface is in the order of 100 nm, eq. 2.15 yields in the minimal time required to obtain bulk-like behaviour between the two polymer surfaces and dissolve the interface: τ_{rep} = 1.49 x 10^{11} s ($\approx$ 4 x 10^7 h). The time related to diffusion that is needed for the polymer to migrate 100 nm is also presented

Table 2.1: Free volume parameters and physical data on PS/toluene[47,57]

parameter	PS/toluene
K_{11}/γ_s $[cm^3/g.K]$	2.20
$K_{21} - T_{g(1)}$ $[K]$	-102.72
K_{12}/γ_p $[cm^3/g.K]$	5.82x10^{-4}
$\hat{V}_s^*$ $[cm^3/g]$	0.917
$\hat{V}_p^*$ $[cm^3/g]$	0.850
D_0 $[cm^2/s]$	1.87x10^{-4}
A $[g.cm^2/s]$	2.23x10^{-2}
ξ [-]	0.61
$\langle R^2 \rangle / Mw$ $[cm^2]$	7.29x10^{-17}
M_w $[g/mol]$	1.84x10^5
M_e $[g/mol]$	1.8x10^4
N^*/N [-]	46.6

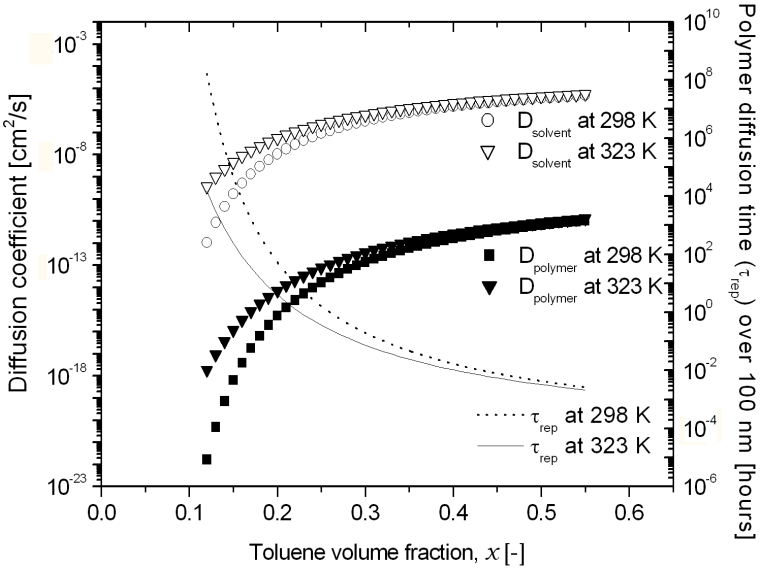

Figure 2.9: Approximations of the solvent and polymer diffusion coefficients as function of toluene volume fraction in a PS/toluene system at 298 K and 323 K (left side axis). Predictions of D are based on Free Volume Parameters derived from Hong[57] and Vrentas.[58] On the right axis the polymer diffusion time is presented needed to overcome a distance of 100 nm, according to eq 2.15

in Figure 2.9. At the particular concentration at the onset of the material system's T_g, complete welding or healing of the polymer-polymer interface is only predicted within a period

of 4 x 10^7 h. The time needed for diffusion decreases accordingly with increasing volume concentration of the solvent. For example at a solvent volume concentration of 26% the same diffusion time has reduced to less than 1 h.

The solvent concentration in the initial 50 - 100 nm of the interface in our experiments is expected to be much higher than a volume concentration of 12% due to the large amount of solvent applied per area. Hence, actual re-establishment of the polymer entangled network at the interface is presumed be achieved within hours.

The increased mobility at higher temperature is predominately visible at lower fractions of solvent. The diffusion coefficient is increased by 5 orders of magnitude at the onset of T_g, due to a temperature increase from 298 K to 323 K. The difference between the two temperatures diminishes at higher solvent fractions. The *diffusion time* to migrate over a 100 nm is reduced in agreement with the diffusion coefficient, by orders of magnitude as well and the 1 h limit is already crossed at volume fractions of 22% rather than of 26%.

The prediction of polymer diffusion of PMMA in a polymer/solvent system via the free volume theory could also be performed if the free volume parameters would have been available. Unfortunately, the availability of useful data on these parameters for PMMA and toluene in literature is very limited. For this reason the diffusion of PMMA is estimated *via* eq. 2.8, knowing the difference in M_e for PS and PMMA. Vrentas[46] estimated the value of M_e for PS to be in the order of 1.8 x 10^4 g/mol, which is in agreement to other work.[59] The average molecular weight between entanglements for PMMA ($\approx 10^4$ g/mol) is nearly a factor of 2 lower than that of PS.[60] The molecular weight of the PMMA used in this work has a Mw of approximately 1.4 x 10^5. The diffusion coefficient for PS should therefore scale down with a factor of approximately $(0.56/0.78)^{2.5} = 0.43$. At a volume fraction of 26% this predicts a diffusion coefficient of 1.23 x 10^{-14} cm^2/s and a diffusion time over 100 nm of 2.3 h.

It is evident from the predictions of the diffusion coefficient that polymer diffusion over large distances (up to 100 nm) can occur in the order of hours or days when solvent concentrations in the welding domain are well above the critical concentration at the onset of T_g and temperatures are above 298 K. The predicted difference between the diffusion coefficient in PS and PMMA is reflected by the results of the welding experiments where similar solvents are able to weld PS to much higher values of lapshear strength within the same period of time.

The wetting experiments of solvents on PS and PMMA have shown that solvent wetting of the substrates is very fast, but spreading is not. In order to spread the solvent over the desired surface, capillary forces should be exerted on the liquid between two polymer surfaces. When spreading occurs directly after introduction of the solvent, the first term in eq. 2.5 can be assumed to be zero compared to the other two. Since the time of solvent absorption differs significantly between the two polymeric materials, loss of solvent applied on PMMA is more likely to happen.

At ambient conditions the evaporation of a sessile drop of solvent is dependent on its vapour pressure. However, when the solvent is absorbed by the polymer, the kinetics of

evaporation change drastically. Li *et al.*[61] showed that the vapour pressure of a drop of toluene on PS was reduced far below the theoretical vapour pressure of pure toluene (0.038 *bar*) to a value approximate to zero in the order of seconds. This behaviour was found to be nearly independent of the PS' molecular weight. As a consequence, the toluene and PS can freely mix over a large period of time. Li stated that although the solvent evaporates slowly in time, traces of toluene are still found within the material after days. Solvents with much lower initial vapour pressures than that of toluene are therefore expected to remain even longer within the polymer and ultimately determine the time of welding/healing.

It has been demonstrated in additional experiments on PS and PMMA using x-ray microtomography (Chapter 4) that after the initial absorption of the solvent, the penetration of solvent stabilises at a certain depth. Such behaviour was also observed by Li when using sessile drops.[61] Subsequent homogenisation of the material by diffusion of the solvent was not observed within days of solvent deployment. As a consequence evaporation should be considered as the predominant mechanism for solvent removal and re-establishing material properties. In order to regain integrity of the newly formed interface, not all solvent should be removed, but the solvent concentration should at least decrease below the critical concentration where $T_g >$ room temperature.

The evaporation time from PS open surfaces is found to be within the order of days for DCB and PAc, but only within minutes for Tol for the top layer (as was observed from indentation experiments). This predicted time dependence of the recovery of a welded interface was clearly observed in the performed lapshear experiments. Both for PS and PMMA a build-up of welding strength was recorded with time, especially when looking at the low vapour pressure solvents (DOP, PAc). The welding time for PMMA is considerably longer than for PS and is in accordance to the solvent absorption rate from the indentation experiments as well as the lower value of the polymer diffusion coefficient.

Based on these solvent welding results, NMP, DCB, PAc, Tol and Dec were identified to be used in the preparation of microcapsules and a self-healing solvent based mechanism for thermoplastic materials to be described in the next chapter. DOP is omitted due its very low vapour pressure and related long welding time.

2.6 Conclusions

The Hansen solubility model appeared to be a good model to select potential effective healing solvents for PS and PMMA. For both PS and PMMA solvent absorption proceeded at a much higher rate than solvent desorption. Hence, the latter is expected to dominate the healing kinetics for the amorphous materials.

The predicted T_g depression and the mobility of the polymer chains with introduction of different solvents was found to correlate well with the solvent assisted healing behaviour recorded in the lapshear tests. The lapshear tests demonstrated that the solvent assisted healing is time dependent and substantial healing for non-volatile solvents can be achieved

at long healing times.

Calculated diffusion coefficient indicated that polymer diffusion across the interface could be established in the order of hours or days for PS and PMMA when solvent concentrations were above the onset of T_g.

The combined results provide the basis for a concept of a solvent-induced self-healing mechanism for thermoplastic materials. In Chapter 3 solvents are encapsulated and embedded inside thermoplastic materials. Solvent deployment will then occur autonomously upon fracture and heal the crack inside the thermoplastic matrix.

CHAPTER 3

Solvent-induced self-healing of thermoplastic materials

Mr. McGuire: "I want to say one word to you. Just one word".
- *Benjamin*: "Yes, sir"?
Mr. McGuire: "Plastics"!
- *Benjamin*: "Exactly how do you mean"?
Mr. McGuire: "There is a great future in plastics. Think about it".

Scene from the film *'The Graduate'*, MGM, 1967

3.1 Introduction

In the previous chapter it was demonstrated that small quantities of solvent are able to weld relative large surfaces of amorphous polymers together. In these experiments the introduction of the solvent progressed through manual injection of the required quantity at the two polymer surfaces. For the design of an autonomous self-healing mechanism, the release of solvent within a polymeric material should be accomplished as a consequence of material cracking itself. In order to do so, several approaches have been presented in literature, which store liquid-healing agent latently inside containers that rupture together with the failing matrix.[11,62,63] It has been demonstrated that the encapsulation of a healing agent

[0]Based on: S.D. Mookhoek, H.R. Fischer, T.J. Dingemans and S. van der Zwaag, *in prep.*, **2010**

within microcapsules is a versatile and straightforward approache in preparation as well as their handling. The autonomously released solvent swells and mobilises the matrix macromolecules across the created interface, analogue to the experiments with manually injected solvent.[64] Healing is established when the polymer chains re-entangle and the solvent is removed. The solvent release and solvent-induced healing of thermoplastic materials using spherical microcapsules is illustrated in Figure 3.1.

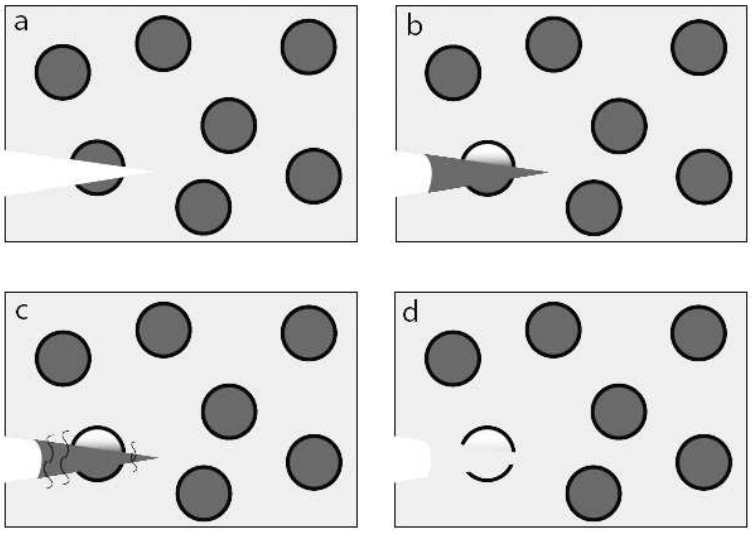

Figure 3.1: (a) When fracture or cracking of the matrix occurs, some of the embedded capsules inside the system will rupture. (b) Upon rupture of the capsules their liquid content flows into the into the crack area. (c) The deployed solvent will slowly dissolve/swell the (uncrosslinked) surrounding matrix material which it has come in contact with. (d) The mobilised polymer chains then bridge the two interfaces and re-entangle and heal the inside of the crack with non-foreign material when the solvent is removed

The incorporation of solvent containing microcapsules inside amorphous thermoplastic materials however is not that straightforward. Thermoplastic materials are normally processed at high temperatures and at high shear in processing installations such as injection moulding and extrusion. A significant modification of the capsule shell is required before the capsules can be used under process conditions that often exceed temperatures of 150^{o}C and shear stresses of 200 kPa.[65] In that case, the produced capsular materials should have both considerable strength and good thermal stability. Secondly, the encapsulated solvent should stay below its boiling point to avoid depletion of healing-agent because of container bursting due to pressure increase and plain evaporation which could lead to potentially harmful formation of gases.

In this chapter the potential of solvent induced self-healing of amorphous thermoplatics

was evaluated experimentally as a first concept. Polymers were processed as a resin system starting with a mixture of polymer and its monomer that could be handled at room temperature. The microcapsules were then dispersed through the resin system and incorporated by bulk-polymerisation of the resin at room temperature, thereby overcoming the disadvantegeous thermal and shear forces involved steps. The reactive molded materials were tested by control fracture and their healing capacity was characterised.

3.2 Experimental

3.2.1 Materials

The solvents o-dichlorobenzene (DCB), phenyl acetate (PAc), cis-decahydronaphthalene (Decalin; Dec), 1-methyl-2-pyrrolidinone (NMP) and toluene (Tol, tech. 80%) were purchased from Sigma Aldrich and were used as received. Urea, resorcinol, ammonium chloride (NH_4Cl), poly(ethylene-maleic anhydride) (EMA), d-chloroform ($CDCl_3$) and 4-N,N-trimethylaniline (TMA) were also purchased from Sigma Aldrich and were used as received. Methyl methacrylate (MMA), styrene (Sty) and ethyleneglycol dimethacrylate (EDMA) monomers were also obtained through Sigma Aldrich but were purified over a basic-Al_2O_3 column to remove the inhibitor. Formaldehyde (37% in water) was ordered through Acros Organics, Belgium. DOW Styron® 638 grade polystyrene (PS, GPC: Mn = 66130 *Da*, PDI = 2.79), was kindly donated by DOW Benelux, The Netherlands and was used as received. Diakon® polymethylmethacrylate (PMMA, GPC: Mn = 50520 *Da*, PDI = 2.81) was received from ICI and was dried under vacuum at 50^oC prior to use. Dibenzoyl peroxide (BPO), a radical initiator (Sigma Aldrich, 75% pure) was recrystallised from methanol and air dried prior to use to remove the remaining water.

3.2.2 Encapsulation of solvents

Solvent encapsulation was performed *via* a slightly modified method earlier described by Brown *et al.*[66] The solvents (60 *ml*) were dispersed in water (100 *ml*) using EMA (25 *ml*, 2,5 wt% in H_2O) as a polymeric surfactant at a stirring rate of 570 *rpm* using a standard 2-blade impeller. An *in-situ* polymerization reaction between urea (2.5 *g*) and formaldehyde (6.3 *g*) was used to encapsulate the liquid within a polymeric (UF) shell wall at a pH of 3.6. The resulting urea-formaldehyde capsules were washed with water and a small quantity of ethanol. The capsules were subsequently dried in air for 24 *h* and could be collected as a free-flowing powder.

3.2.3 Microcapsule characterisation

Optical microscopy The synthesised microcapsules were evaluated using a calibrated Leica optical microscope equipped with a CCD camera. Capsule size distributions, mean

diameters and standard deviations were determined from a data set of at least 200 individual microcapsules in microscope images.

Differential Scanning Calorimetry (DSC) Besides using microscopic techniques the microcapsules were characterised using Differential Scanning Calorimetry (DSC) on a PerkinElmer Sapphire DSC from -100 to 20^{o}C in a closed sample pan. Prior to the measurements the capsules were hold isothermally at -100^{o}C for 30 min. Samples of typical 10 mg were investigated using a heating rate of 10 K/min under flowing N_2 gas.

The curing behaviour of monomer-polymer mixture resin systems was investigated using isothermal DSC at 25^{o}C. Sample weigths were typically 7.5 mg and were measured in special aluminium pans for volatile substances, preventing evaporation.

Capsule permeability study The permeability of the synthesized capsules was tested by extraction experiments in MMA monomer to detect if the capsule liquid would leach into the surrounding matrix monomer while processing the specimens. For these experiments 0.4 g of capsules was dispersed in 2.6 g of purified MMA whilst stirring. After 45 min the capsules were filtered off and the MMA filtrate was examined by 1H NMR spectroscopy. Subsequently, the capsule residue was washed with a small quantity of diethylether and dried for 1 h in air. The dried capsules were ground in a mortar and the crushed capsules were extracted with 2 g of $CDCl_3$. The collected $CDCl_3$ was then also examined by 1H NMR.

3.2.4 Preparation of bulk-polymerised thermoplastic matrix and self-healing composite material

The thermoplastic matrix materials were either PMMA or a blend of PMMA/PS. The materials were bulk-polymerised from a resin system, comprising a solution of a 4:1 by weight ratio of MMA/PMMA or 2:1 by weight of MMA/PS. The fraction of pre-made polymer was added to the monomer for viscosity control. Both resin systems were employed with a small quantity of EDMA (5 wt% per hundred monomer) to accelerate the polymer hardening. Prior to specimen fabrication 1.0 wt% with respect to the monomer of purified BPO was mixed into the resin. Next, the resin was degassed in a desiccator under vacuum for a few minutes to remove entrapped air. The encapsulated solvents were added according to the recipe and were dispersed by hand. Subsequently 0.10 wt% with respect to the monomer of TMA was added to the resin to commence the accelerated radical polymerisation reaction at ambient temperature. The hardening resin was degassed again for 5 min and quickly poured into a polyethylene mould (HDPE). The resin with or without capsules was cured within 1 h. The cured specimens were stored in a fume cabinet at room temperature for at least 7 $days$ prior to testing, allowing residual monomer to post-polymerise or escape from the material by evaporation.

3.2.4.1 Sample recipe for testing

The prepared capsule-thermoplastic composite samples are denoted as the PMMA-?-X, in which '?' is the concentration (by wt%) of added capsules and 'X' the type of incorporated solvent (DCB, PAc, Tol, Dec). Application of Dec is used for reference only since it was demonstrated that Dec was unable to weld PMMA.[64] The recipes at which the different samples were prepared can be found in Table 3.1

Table 3.1: The recipes for the prepared PMMA samples for self-healing evaluation

component [g]	MMA	EDMA	PMMA	BPO	Capsules	TMA
PMMA-0	32.0	1.60	8.0	0.32	0	0.032
PMMA-5-X	32.0	1.60	8.0	0.32	2.00	0.032
PMMA-10-X	32.0	1.60	8.0	0.32	4.00	0.032
PMMA-15-X	32.0	1.60	8.0	0.32	6.00	0.032

3.2.5 Matrix and capsule-composite material characterisation

Dynamic Mechanical Thermal Analysis (DMTA) The matrix materials properties were evaluated using DMTA on a PerkinElmer Pyris Diamond DTA apparatus. All tests were performed in oscillatory bending mode at a heating rate of 2 K/min, deformation frequency of 1 Hz and amplitude of 5 μm. The tested samples had a typical geometry of 50 x 4 x 10 mm (length x thickness x width).

Fracture and healing tests Fracture testing followed earlier reported protocols by Brown *et al.* and Rule *et al.* using tapered double cantilever beam (TDCB) samples[62,67] prepared either from polymethyl methacrylate (PMMA) or a blend of PMMA and polystyrene (PS). The applied TDCB sample geometry was initially designed by Beres *et al.*[68] and results a geometry with a crack-length independent value of the fracture toughness. In this work a modified short groove (25 mm) TDCB test geometry was used to limit the crack face separation.[67] The TDCB geometry used is depicted in Figure 3.2.

After a precrack was inserted with a sharp razor blade into the groove of the sample, the TDCB specimens were pin-loaded and tested to failure using a Zwick/Roell 20 kN tensile load frame under displacement control at a rate of 300 $\mu m/min$. After fracture, the two crack surfaces were clamped together by an external force of 5 N and were allowed to heal at room temperature (25^{o}C). The healed TDCB samples were again loaded to failure and the load-displacement curve was recorded. The healed samples were tested after 2, 7, or 14 $days$ of healing. Healing efficiencies (HE) are defined as the ratio between the healed and the

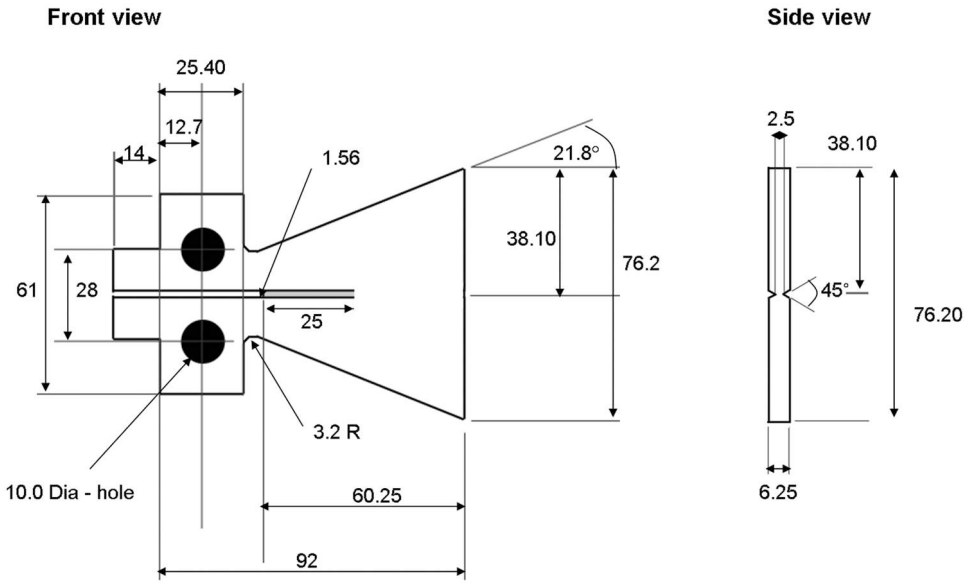

Figure 3.2: TDCB geometry (dimensions in mm)

virgin fracture peak loads before fracture ($HE_{str} = P_{healed}/P_{virgin}$), defining the strength-related healing. P_{virgin} represents the maximum load before fracture of the virgin sample and P_{healed} is the maximum load before the healed sample's compliance deviates from the virgin sample. A solvent volume of 0.025 $\mu l/mm^2$ was injected between the fracture planes of PMMA-0 samples. These were subsequently allowed to heal and tested for mechanical recovery, simulating the solvent-induced healing of a 15 vol% capsule filled specimen.

Crack-plane investigation To study the fracture behaviour of embedded solvent-containg capsules in the matrix, fracture surfaces of virgin and healed TDCB specimens were investigated by Scanning Electron Microscopy (JEOL 7500) and Confocal Laser Scanning Microscopy (Olympus LEXT) after applying a 10 nm Au-sputtered layer.

3.3 Results and discussion

3.3.1 Solvent filled microcapsules

All priorly investigated solvents, except for NMP, were successfully encapsulated and resulted in polymer microcapsules as a free flowing powder with little to no polymer residue outside the microcapsule shell wall. NMP could not be encapsulated due to the miscibility with organic as well as aqueous media and was therefore omitted from this investigation. The capsule size distribution and capsule morphology for each of the solvent encapsulation procedure are presented in Figure 3.3.

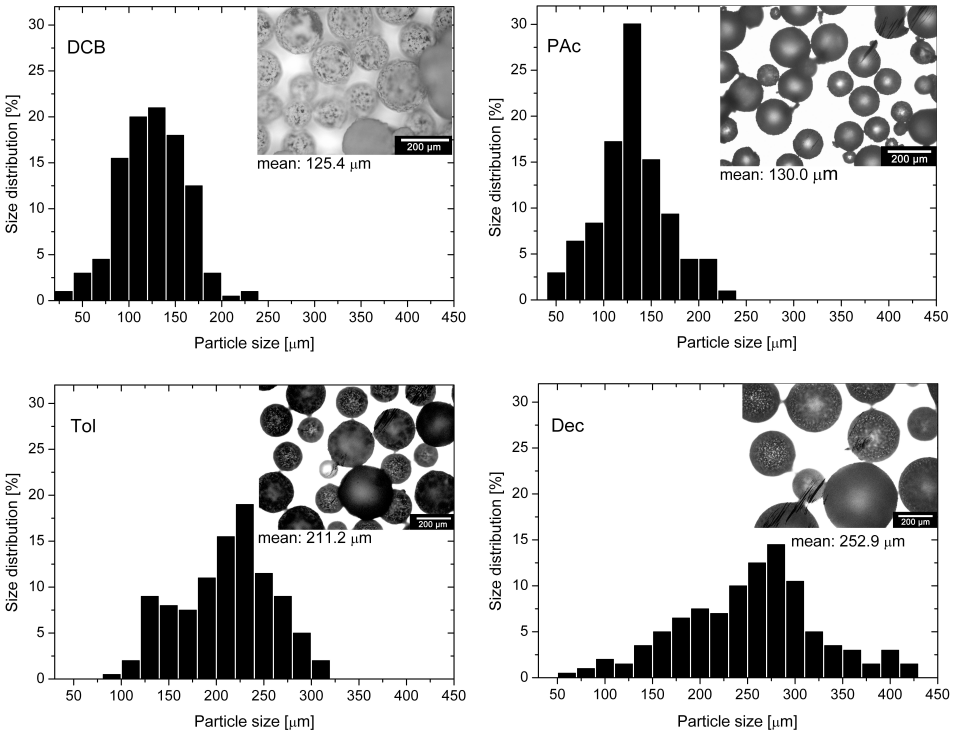

Figure 3.3: Size distributions and structure morphology for the synthesised capsules: a) UF(DCB), b) UF(PAc), c) UF(Tol) and d) UF(Dec)

Figure 3.3 shows that a monomodal size distribution is obtained for the solvent encapsulations. The polydispersity of the capsule size varies significantly although the solvents were dispersed at identical processing conditions. Both DCB and PAc show a narrow capsule distribution between 0 and 250 μm. In contrast, Tol and Dec show a more broad size distri-

bution between 0 and 450μm. Tol and Dec are both volatile substances compared to DCB and PAc and the large size distribution is most probably the effect of partly evaporation of the solvent during encapsulation procedure.

Liquid release was observed for the four created solvent containing capsules when crushing them between two glass plates. The presence of the encapsulated solvent within the capsule in large volume was demonstrated by DSC. Figure 3.4 shows the melting peaks of the encapsulated phase as function of temperature for each of the encapsulated solvents. The observed minima of the melting peaks of the crystallised solvents (PAc: -2^{o}C, DCB: -13^{o}C, Dec: -61 / -41^{o}C and Tol: -92^{o}C) reflect the melting points of the solvents grade used. In Figure 3.4 a double melting point is observed for the Dec filled microcapsules. This observation corresponds to a similarly detected melting behaviour for the pure decalin grade used and is caused by the different melting point of cis- and trans-decalin.

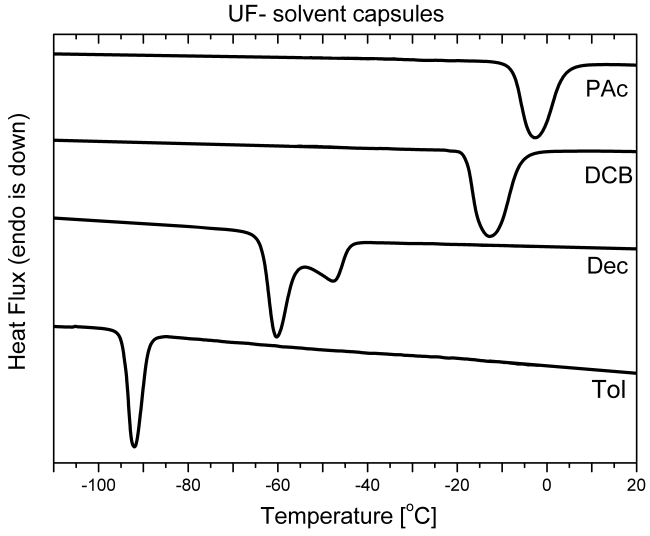

Figure 3.4: DSC measurements indicating the presence of the encapsulated phase inside the UF-microcapsules by characterising the melting point of the solvents

When all the solvent inside the microcapsules is crystallised, the area of the melting peaks directly relates to the encapsulated quantity of solvent. However in the experiments performed on encapsulated and pure solvents, complete crystallisation of the solvent was never obtained. Hence, the encapsulation degree cannot be assessed by determination of the recorded heat of fusion of the core solvent.

The solvent permeability of the urea-formaldehyde polymer shell wall is limited. Leaching of solvent is not observed when capsules are dispersed inside liquid MMA monomer for 45 min. The 1H NMR spectrum (Fig 3.5a) from the MMA filtrate shows that DCB was

not extracted by the MMA (δ = 1.2 - 1.7 (H1, 3H), 3.1 - 3.6 (H2, 3H), 4.8 - 5.3 (H3, 1H) and 5.4 - 5.9 (H4, 1H)). The 1H NMR spectrum of the capsule contents demonstrated that also no MMA penetration into the DCB core (δ = 6.9 - 7.2 (H1, 2H) and 7.3 - 7.7 (H4, 1H)) was observed (Fig 3.5b) as well. Hence, the quality of the microcapsules is adequate and loss of solvent during processing of the microcapsules in monomer/polymer mixtures is neglectable. All the incorporated solvent inside the microcapsules at sample preparation is therefore assumed available for self-healing.

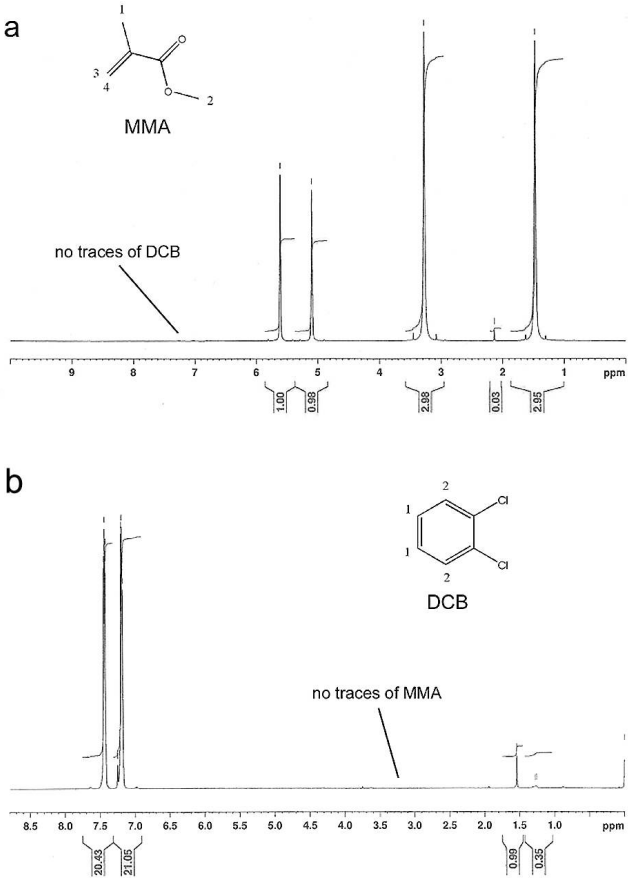

Figure 3.5: 1H NMR spectra of microcapsule solvent permeability experiment, a) MMA filtrate after 45 *min* of capsule immersion, b) extract of crushed capsules after immersion in MMA

The depletion of encapsulated solvent from the microcapsules was observed when contact times with solvent on the outside of the shell exceeded a period of several days. Earlier reported experiments by Yuan on the solvent permeability of UF capsules (having a 30 -

60 μm thick shell) showed comparable behaviour in time. Significant encapsulate depletion was only recorded in their experiments, when the capsules were placed in solvents such as acetone for periods of days.[69]

3.3.2 Thermoplastic material matrix

3.3.2.1 Thermoplastic resin polymerisation

The MMA-PMMA resin system could be successfully polymerised in a mold at room temperature by radical polymerisation with the aid of tertiary amine accelerator (TMA). The resin system solidified within a period of 30 min (independent of the presence of solvent containing capsules), exhibiting a large exotherm (Figure 3.6). The solidified material could easily be removed from the mold without distorting the shape of the molded sample. The MMA-PS system could be polymerised similarly, but solidified only after more than 45 min. In comparison to the PMMA system a much lower exotherm was recorded (Figure 3.6). During polymerisation of the MMA-PS resin system, phase separation of the growing PMMA phase and the dissolved PS was observed, turning the clear solution turbid to off-white in time. The solidified material still appeared heavily plasticised upon removal of the sample from the mold and unwanted deformation of the sample occurred easily. Attempts to polymerise a Sty-PS resin to produce an all-PS matrix material following the same reaction procedure were unsuccessful. Polymerisation of the Sty-PS resin resulted only in an increase of the solution viscosity and a full solidification of the resin was never obtained.

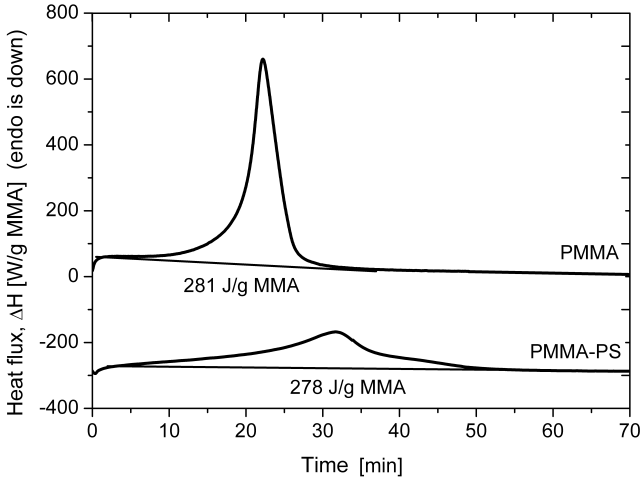

Figure 3.6: Isothermal DSC curing curves for MMA-PMMA and MMA-PS resin

Fig 3.6 shows the difference in accelerated radical polymerisation behaviour of the two MMA-based resin systems at room temperature. The polymerisation for PMMA is much faster and exhibits a more exothermic curing behaviour in comparison to the PMMA-PS system. The accumulated exothermic energy for both polymerisations however is comparable and indicates that the fraction of reacted MMA in both resin types is comparable. The recorded heat of polymerisation is for both systems rather low in comparison to literature values for the complete polymerisation of MMA (559 J/g).[70] This observation indicates that a large fraction of unreacted MMA is still present when the material is solidified, plasticizing the matrix until it post-polymerises or evaporates.

It is hypothesised that the MMA polymerisation within the MMA-PS leads to the formation of lower molecular weight polymer that plasticises the solidified material, since the polymerised PMMA-PS is found to be far more ductile than the solidified PMMA. Brittle material fracture is desired in order to evaluate the material's self-healing properties upon addition of solvent capsules. The effect of a ductile matrix is that loading will lead to deformation/yielding of the matrix, but will not rupture the much stiffer embedded microcapsules. Only after very long ageing time (months) the PMMA-PS material becomes stiffer and more brittle in nature. Hence, the fracture and healing tests are only performed on the MMA-PMMA cured resin, since solvent depletion from the capsules can no longer be assumed to be absent in the plasticised PMMA-PS matrix.

3.3.2.2 Evaluation of mechanical properties

Although the polymerised MMA-PMMA resin shows significant stiffness and brittle fracture after solidification, its material properties change significantly with ageing time as well. This behaviour is found to be independent of capsule concentration. From DMA experiments (Figure 3.7) it can be observed that the cured PMMA material initially exhibits a glass transition temperature at 128^{o}C with a broad shoulder on the tan(δ) peak towards lower temperatures.

The function of tan(δ) in combination with a shoulder in the storage modulus, indicates the presence of multiple phases within the material. As a function of time the shoulder in tan(δ) grows, the initial T_g related tan(δ) peak disappears and the shoulder in G' decreases in the direction of the arrows. The T_g of the material equilibrates to a value of 109^{o}C after 14 days of ageing. The modulus of the material below T_g increases with ageing, securing better properties for the fracture and healing experiments. These effects can most probably be explained by the way the bulk polymerisation of the MMA-PMMA resin system progresses. Upon polymerisation, the increasing fraction of PMMA suddenly precipitates from the monomer when the solubility limit is reached, hereby creating a two phase system from a homogeneous system. The residual monomer then continues to polymerise further until again the chains are no longer soluble and percipitate. As a result different domains of polymer with varying molecular weight exist when the the sample has solidified. Because of these different domains the resulting PMMA material initially is expected to be largely het-

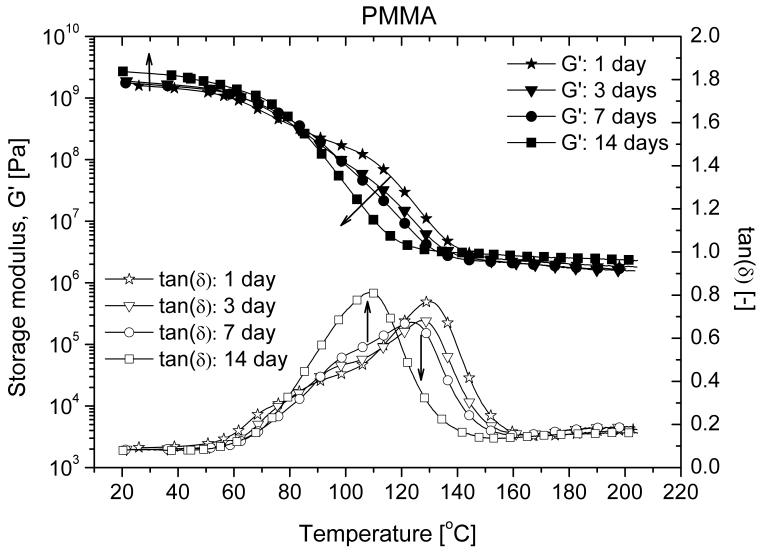

Figure 3.7: Evaluation of the mechanical properties as a function of ageing time for a cured MMA-PMMA system

erogeneous in nature. In time the material homogenises slowly due to the intrinsic polymer mobility assisted by remaining MMA that ultimately gives the mechanical behaviour after 14 *days*. Hence, it was found that mechanical tests have to be performed at least 7 *days* after sample preparation in order to obtain reproducible material fracture and healing.

3.3.3 Fracture and healing tests

3.3.3.1 The effect of healing time

Representative virgin fracture and healed load-displacement curves for a PMMA-15-DCB system as a function of healing time are displayed in Figure 3.8. The load-displacement figure for the virgin material shows a classical brittle fracture that propagates the crack from the intial pre-crack length to the end of the 25 *mm* long groove. Loading beyond this point shows the remaining compliance of the TDCB as the sample is bent at the end of the groove. Figure 3.8 shows that the compliance of the healed interface is lower than that of the virgin sample. Absorbance of the solvent has plasticised the weld and lowered the stiffness, resulting in a smaller initial slope in forced-displacement curve. The peak load before fracture of the virgin fracture is significantly higher than the recorded peak loads after healing. The peak loads of the healed samples are indicated in the figure by horizontal lines at the load-axis. Beyond this point the initial compliance of the material changes and the polymer at the healed crack starts yielding. Plastic deformation of the bonded surfaces is observed

(rather than brittle fracture), which is demonstrated by the relative large displacement at low load increase, as the crack reopens. Occasionally stick-slip behaviour is observed as the failure of the weld propagates. At approximately 1.3 *mm* of displacement all the healed samples show the same level of compliance that is similar to the recorded value for the virgin material, when the total crack has reopened completely.

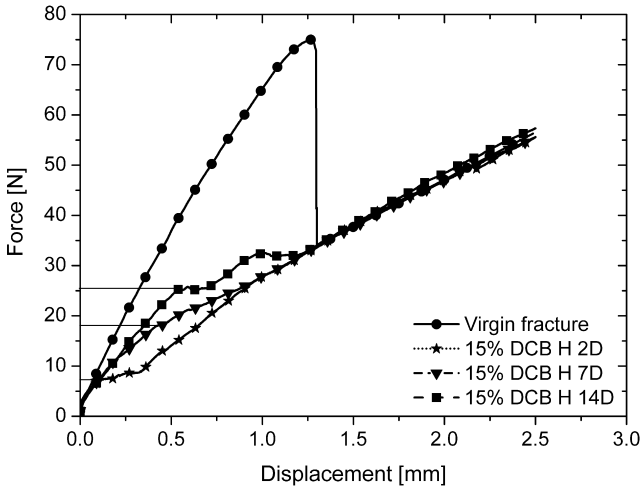

Figure 3.8: Representative load-displacement curves for TDCB testing, showing virgin material fracture and re-fracture of healed samples for different healing times.

The determined average strength related healing efficiencies (HE_{str}) as a function of healing time for the systems: PMMA-15-DCB, -PAc, -Tol and -Dec are presented in Figure 3.9a. The average efficiencies of the capsule-based samples are compared to PMMA-0 samples that were injected with the relative solvent. The measured efficiency for DCB and PAc are found comparable within error of the measurements. Both solvents show an increase of the efficiency with time and the increase is in accordance to the observations made in Chapter 2. The increase in efficiency with healing time for samples with the injected solvent is also found in agreement with the capsule containing systems. At longer healing times the increase of the efficiency appears to level off at a maximal achievable healing efficiency for PMMA-15-DCB and -PAc. The healing efficiency nearly becomes constant at a value of 30% at 14 days of healing.

Very smooth and flat fracture surfaces are obtained for PMMA-0 since no capsules are incorporated. Fracture surfaces of PMMA-15 have a much rougher and angular topology due to a continuously changed crack path through the capsules. As a result, the two surfaces of PMMA-0 can be repositioned within close proximity after fracture. A larger crack opening distance is expected for PMMA-15 due to small misalignment of the surfaces. Hence, the measured healing efficiency levels are significantly higher for the injected samples than those

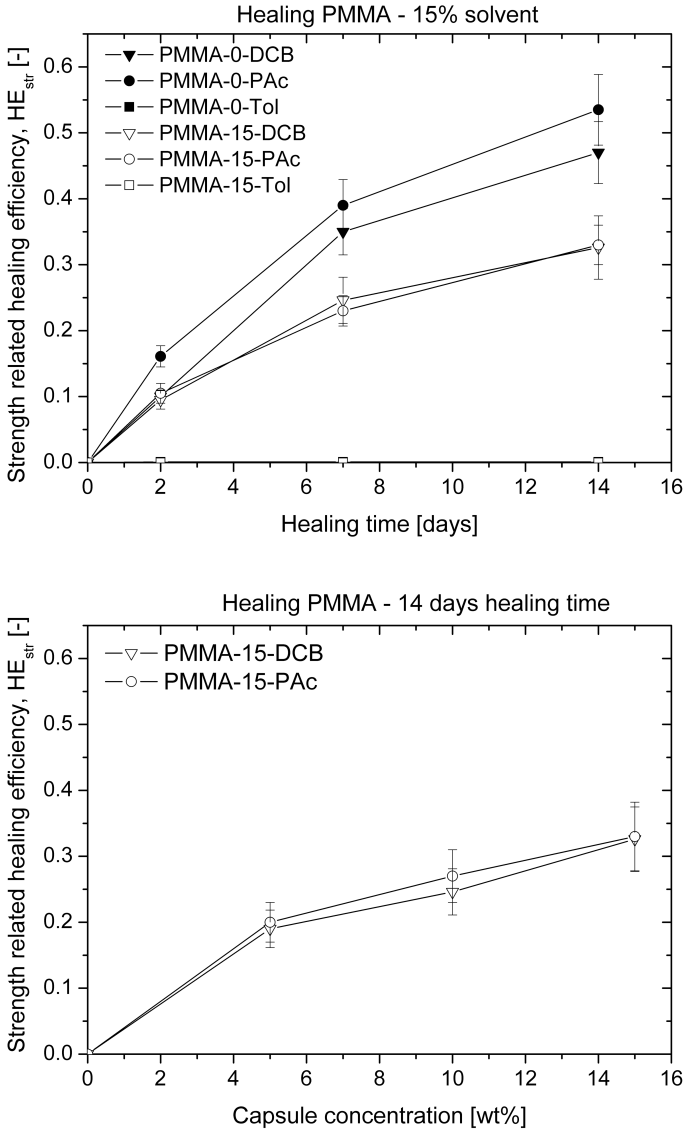

Figure 3.9: Average strength related healing efficiencies, a) as a function of healing time and b) as a function of capsule concentration for the investigated solvents: DCB, PAc, Tol and Dec.

for the capsule based samples.

The control solvent (Dec), does not show any healing which is in line with our expectations. It proves that the intrinsic matrix material is unable to self-heal without the presence of solvent. Surprisingly, for Tol no healing was observed. Additionally, the PMMA-0 samples that were injected with Tol did not show any effect of solvent-induced healing. Lapshear welding experiments showed very high shear strengths for Tol as is discussed in Chapter 2. The disparity between these results appears to be an effect of the experimental conditions. The very small amounts of Tol released or injected in the TDCB are able to evaporate fast from the small surface as the crack opening is large at the time of testing. In the lapshear experiments the amount of Tol is directly injected between two high surface area plates, already at close proximity, reducing the initial evaporation substantially. Figure 2.6 in Chapter 2 shows that the T_g of the top-layer of the polymer increases above room temperature quickly as Tol evaporates. Since the process of evaporation is in competition with the swelling of the matrix, fast evaporation makes healing impossible.

3.3.3.2 The effect of capsule concentration

In figure 3.9b the average strength related healing efficiency is given as a function of the capsule concentration for a healing time of 14 *days*. Again, the healing efficiencies for both solvent types are found to be equal when comparing the healing with DCB and PAc. In addition, both calculated efficiencies show a small increase with higher capsule concentration at this healing period.

The combined results demonstrate that non-reactive solvents, *i.e.* DCB and PAc, that are released from embedded microcapsules are able to autonomously heal a crack in PMMA. As a control, fractured samples of PMMA-15-DCB and -PAc were additionally allowed to heal at a reduced temperature of 4°C (assuming to be below the solvent-depressed T_g of the PMMA). In this case recovery of the fracture strength was not observed. The absence of healing at this temperature indicates that the solvent-induced healing is indeed the effect of mobilised chains at healing temperatures above the material's depressed T_g.

3.3.3.3 Investigation of the fracture and healed surfaces

An investigation of the fracture surfaces with SEM and LSCM indicated that the embedded UF capsules failed together with the surrounding matrix and release their contents accordingly. An SEM image of a virgin fracture surface can be found in Fig 3.10. The image, taken from a fracture surface of a PMMA-10-DCB sample, shows a typical fracture surface exposing the ruptured embedded microcapsules. Some of particles are not fractured, but are removed from the fracture plane as the propagating crack deflects and debonds the particles. Figure 3.10b shows a close-up of a typical fractured capsule with diameter of 127 μm. Around the ruptured capsule the image displays the fracture lines along which the crack propagated. The capsule shell can clearly be observed and displays a smooth shell (< 1 μm) with a very coarse outer texture (*ca.* 5 μm) which is anchored in the matrix material.

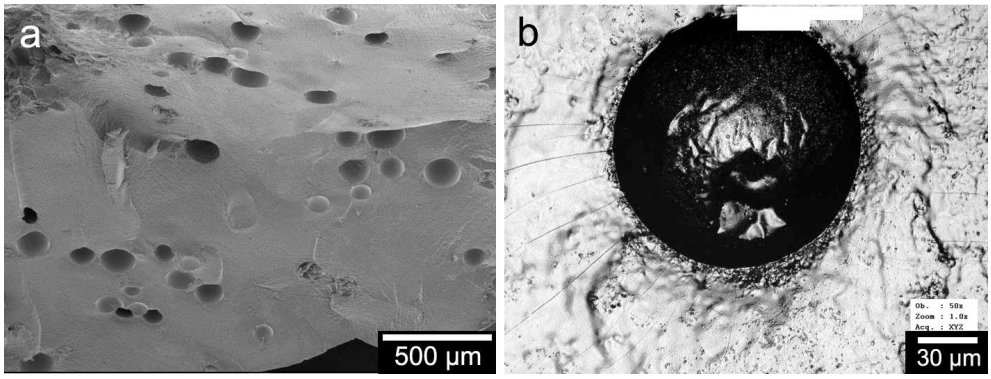

Figure 3.10: Investigation of fracture surfaces, a) SEM image of a PMMA-10-DCB sample after virgin fracture and b) a high magnification LSCM image of a single ruptured capsule displaying the capsule shell wall.

After healing, a second investigation of the fracture surface revealed that due to the solvent contact, changes in surface morphology could be observed. Figure 3.11a depicts an LSCM image giving a section of the healed fracture surface. A height-profile of the surface along the indicated line is presented below in Figure 3.11b.

Figure 3.11 shows an interesting topography. A rivulet shaped rim of material curves around the fractured capsules on the surface. The sharp and higher edged rim (depicted in blue) indicates that at this location the fracture surface was swollen by the released solvent and was re-connected to the opposite surface upon healing. The volume increase due to the swelling of matrix resulted in an increase of polymer mobility and established the polymer rim through polymer reptation when the two surfaces were pushed together. The sharp observed feature is a result of the second fracture test when the healed connection was broken. At other places, *i.e.* the bottom side of the big capsule cavity and around the smaller cavity in the right bottom corner (depicted in red), the rim is not as sharp and suggests only a volume increase without establishing contact with the opposite surface. The profile of the cross-section of the capsules in the profile is however not completely correct. Due to absence of reflected light from the capsule bottom the curvature of the capsule cannot be recorded.

The image also shows that the healed contact area is small compared to the total crack area and hence total healing is not expected. Although the two crack faces of the tested specimen were pushed together, the remaining crack face separation stays too large for the matrix to be fully bridged by the released amount solvent. Nevertheless, the small surface contact causes a significant increase in material properties and allows the material to regain *ca.* nearly 30% of its original peak load before fracture.

An examination of the fracture surfaces however is only indicative of the solvent release and matrix healing. At the same time, the solvent-microcapsule-matrix healing system is found rather complex and the solvent-induced healing depends on many (time dependent)

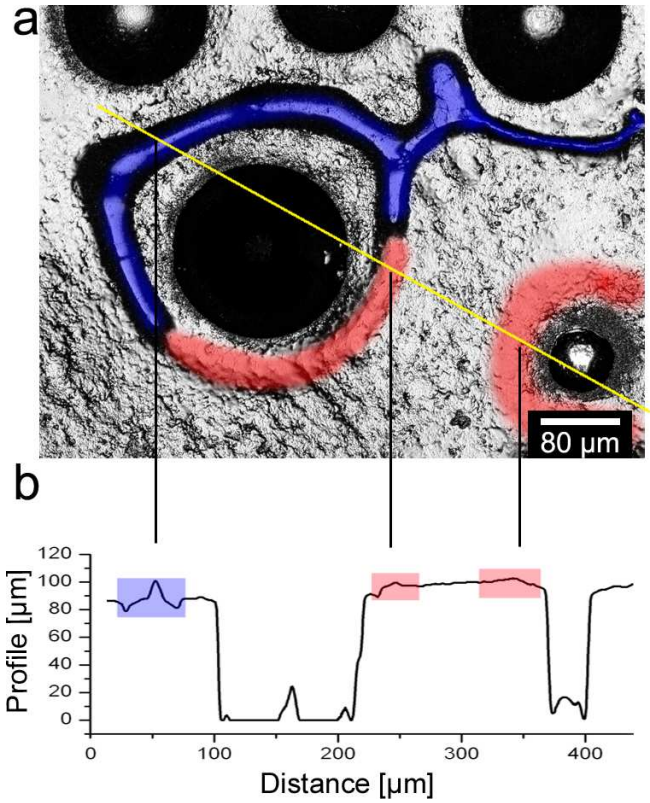

Figure 3.11: a) a LSCM image of a section of the healed surface showing a rivulet of healed material on the surface and b) the corresponding height-profile along the indicated yellow line

parameters. Hence, the release of solvent at the crack and the solvent kinetics inside the polymer matrix have to be examined in more detail. Using X-ray tomography the release of solvent at the crack and the solvent kinetics can be characterised. The results of that investigation are presented in Chapter 4.

3.4 Conclusions

It was demonstrated that non-reactive solvents are able to heal thermoplastic materials without external intervention.

The selected solvents for the design of self-healing thermoplastics could be encapsulated successfully in urea-formaldehyde capsules and their presence was confirmed by DSC. The stability of the prepared capsules was guaranteed during processing since no premature solvent depletion was observed.

Accelerated radical polymerisation of a MMA-PMMA resin resulted in adequate material properties comparable to commercially available PMMA, but he influence of ageing of the polymer matrix cannot be ignored when evaluating mechanical properties such as fracture and healing. Reproducible data for fracture and healing experiments can only be obtained when experiments are performed at least 7 days after preparation.

Autonomous solvent deployment was able to heal a formed crack and recover the fracture strength of PMMA. Depending on capsule loading and healing time, cracks were only healed partly and a maximum strength related healing efficiency of 30% is be obtained for a capsule loading of 15 wt% after healing time of 14 days. Due to a required healing time in the order of days, solvents with high volatility are found unsuitable as healing agents. The removal of solvent appears to be the crucial factor for healing and healing time is found to be the predominant parameter. Qualitative and quantitative characterisation of the solvent release and healing kinetics is needed to understand the solvent-induced healing of thermoplastics better.

The presented concept has shown potential for the further development of industrial materials based on the similar concept. Hence, future work should lead to the development of thermally and mechanical stable containers that would able to process solvent-type liquids together with commercial available thermoplastics at high temperatures and high shear forces.

CHAPTER 4

Observation of liquid-based self-healing features using x-ray tomography

Some men see things as they are and say why?
- I dream things that never were and say why not?

George Bernard Shaw

4.1 Introduction

X-ray tomography is a versatile, non-destructive, experimental technique that is able to display fine morphological features within optically non-transparent materials and reconstruct their spatial characteristics and volume fraction in 3D.[71] Alongside other methods, *e.g.* Magnetic Resonance Imaging (MRI) and Acoustic imaging, X-ray tomography is widely applied for medical purposes and for characterisation of materials in general.[72,73] Most instruments yield information with a resolution of $< 100\ \mu m$ as the topology reconstruction is based on conventional absorbance contrast, being sufficient for most applications. Microtomography experiments under conditions leading to additional phase-contrast give much improved contrast in particular for soft materials but generally require X-ray beam characteristics which are only provided by synchrotron facilities,[74] not being a routine instrument and thus greatly

[0]Partly based on: S.D. Mookhoek, S.C. Mayo, A.E. Hughes, S.A. Furman, H.R. Fischer and S. van der Zwaag, *Adv. Eng. Mater.*, **2010**, doi: adem.200900289
S.D. Mookhoek, H.R. Fischer, S. van der Zwaag and W. Ludwig, **2010**, *in preparation*

adding to the cost of such experiments. To reach the required x-ray beam coherency for phase contrast but at much reduced costs, CSIRO in collaboration with XRT ltd. developed an X-ray Ultra Microscope (XuM) set-up which is based on a standard SEM.[75] With the tailored apparatus it is possible to resolve small (20 - 2000 μm) particles in engineering polymer composites with excellent resolution ($\approx$ 10 μm) using in-line phase contrast in addition to absorption-contrast.[76] The combination of both contrast techniques makes it possible to even distinguish between hollow and liquid filled capsules incorporated in a polymeric matrix. This ability is extremely useful for measuring the fine details of novel self-healing polymer systems containing a liquid healing agent stored in microcapsules.[18,21,77] The technique is described in more detail in Paragraph 4.2.3.2.

While the occurrence of self-healing for such systems has been demonstrated irrefutably by the partial restoration of the fracture strength of thermosetting materials after cracking[18,19,25] no studies have been reported on the actual release process of the healing agent from ruptured particles near the original crack surface. In the present work we make use of the potential of the custom made XuM technique and Synchrotron facilities to visualise and examine the liquid-capsule composite morphology near the crack plane as well as throughout the rest of the volume. SEM-based x-ray tomography is used to detect the depleted layers of microcapsules close to the crack surfaces after healing and quantify the released liquid volume in a static mode. Given the low beam dose, exposure times to record tomographic data are rather long (approximately 7 h), precluding dynamic studies of the liquid spreading and healing. On the other hand, synchrotron x-ray tomography provides fast scanning procedures and allows dynamic investigation of the healing agent release processes after cracking. Both techniques are applied to the novel solvent-based class of microcapsule-based self-healing materials (see Chapter 3).

4.2 Experimental

4.2.1 Materials

Urea, resorcinol, ethylene-maleic anhydride copolymer (EMA), methyl methacrylate (MMA), ethyleneglycol dimethacrylate (EDMA), dibenzoylperoxide (BPO), o-dichlorobenzene (DCB), bromobenzene (BB) and 4,N,N-trimethylaniline (TMA) were all purchased from Sigma Aldrich, The Netherlands. Formaldehyde, 37% in H_2O and ammonium chloride (NH_4Cl) were obtained via Acros Organics, Belgium. Polystyrene (PS), Styron grade 638, was kindly donated by DOW Benelux, The Netherlands. Prior to use MMA was purified over a basic Al_2O_3 column, removing the radical inhibitor. BPO was recrystallised from methanol to remove the water present. All other materials were used as received without further purification.

4.2.2 Urea-formaldehyde encapsulation of contrast solvents

o-Dichlorobenzene (DCB) and bromobenzene (BB), both suitable solvents for polystyrene,[38,78] and high density solvents with good x-ray contrast were encapsulated according to the method described by Brown *et al.* using the same synthesis conditions.[66] After dissolving the urea, resorcinol and ammonium chloride (NH_4Cl) in a 2.5 $wt\%$ ethylene-maleic anhydride copolymer (EMA)/H_2O solution the pH was adjusted to 3.60. Subsequently a volume of 60 ml of DCB or BB was slowly added to the stirring solution. After 20 min of agitation the formaldehyde was added and the reaction was commenced by heating the dispersion to 55^0C at 1 K/min. After 4 h reaction time the microcapsules were redispersed in 500 ml deionized water, filtrated under vacuum and washed with another 200 ml of water. The remaining water was removed by a second washing step using ethanol (96% technical grade). The capsules were then air dried until resulting a free-flowing powder. The DCB-filled microcapsules created at 1100 rpm resulted in *ca.* 60 μm microcapsules. The BB-filled microcapsules created at 900, 1220 and 1520 rpm resulted in *ca.* 85, 60 and 45 μm diameter capsules respectively.

4.2.3 SEM-based x-ray microtomography for static evaluation of solvent release

4.2.3.1 Preparation of PMMA-PS cylindrical samples for static experiments

The microcapsules were dispersed in a 2:1 by weight ratio of MMA/PS solution containing 5 $wt\%$ of EDMA and 1 $wt\%$ of BPO. After removal of entrapped air by subjecting the mixture to a reduced pressure environment, 0.1 $wt\%$ of TMA was added to start the hardening of the resin. For these experiments the curing PMMA-PS resin was injected into a polyethylene cylindrical mould with a typical diameter of 2 mm and height of 2 cm. After 1 h the sample was removed from the mold. Full sample equilibration was ensured by storing the samples for 14 $days$ at ambient conditions. The hardened cylindrical PMMA-PS composite containing 15 $wt\%$ of DCB filled microcapsules were opaque and brittle in nature.

The cylinders were fractured perpendicular to the cylinder axis close to middle of the sample using a 4-point bending mode. Solvent release was observed by the naked eye directly after fracture. To minimise possible evaporation of the solvent the two cylinder-ends were gently put back together within a period of seconds, positioning the cylinder ends back in their original alignment. After 7 $days$ of healing period the samples were investigated using X-ray microtomography. The sample morphology at large distances from the crack was assumed to be unchanged after the controlled fracture test. Hence, no scans of the initial state of the sample were performed.

4.2.3.2 X-ray microscopy and microtomography

X-ray microscopy and microtomography were carried out using a prototype X-ray ultra-Microscope (XuM), developed in collaboration between CSIRO and XRT Ltd.[76] The set-up is hosted on a standard SEM (Philips-FEI XL 30 S-FEG) to which it adds x-ray microscopy and microtomography functionality. It uses the fine electron focus on a tantalum foil to produce a submicron x-ray source for high resolution imaging and tomography. The sample is placed (and in case of the tomographic measurement rotated) between the x-ray source and the x-ray CCD detector giving a simple point projection geometry with natural magnification (Figure 4.1). Typically the source to sample distance R1 is much smaller than the source to detector distance giving magnifications of 10x to 2000x. The small source size coupled with the imaging geometry means that the system also benefits from additional contrast through refractive effects known as in-line phase contrast which enhances the visibility of edges, boundaries and voids in the sample.

For the data collection the Ta foil target was used with an SEM accelerating voltage of 30 kV. The resulting average detected x-ray energy is constrained by these parameters to around 8 keV. Tomographic datasets of healed samples were acquired from which three-dimensional reconstructions were produced. The tomographic datasets consisted of 720 views of the samples with 0.5^o rotations of the samples between each view. The total image recording time was 7 h and the image magnification was x10 at the detector.

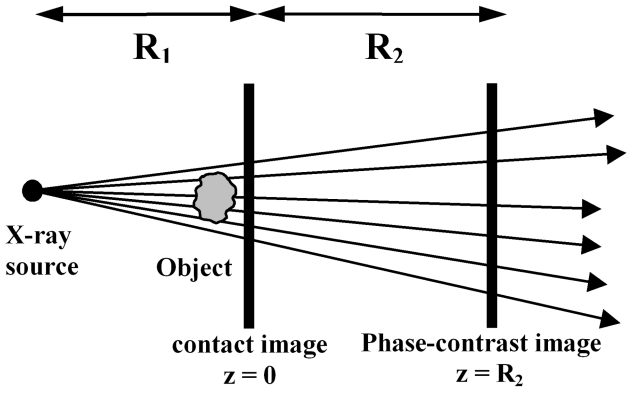

Figure 4.1: Schematic of XuM imaging geometry

The raw experimental x-ray images contained phase-contrast as well as the conventional absorption-contrast information; therefore it was necessary to perform phase-retrieval on the images prior to tomographic reconstruction. The data was processed using the X-TRACT software for both phase-retrieval (Paganin method[79]) and tomographic reconstruction.

In this case we use the simplest form of inline phase-contrast in which the edges and boundaries are enhanced by near-field Fresnel diffraction, rather than the multiple dataset form used for holotomography introduced by Cloetens.[80] In this simpler case the data is

amenable to phase-retrieval using the single-image algorithm of Paganin.[79] This transforms the data, which contains both phase- and absorption-contrast with much improved signal to noise than if only absorption-contrast data is used.

The reconstructed tomographic data was in the form of a series of axial (X-Y plane) images down the longitudinal (Z) axis of the cylindrical sample. The reconstructed data were imported into a commercial available software platform (AMIRA[81]), for segmentation and analysis.

4.2.4 Synchrotron x-ray tomography for dynamic evaluation of solvent release

4.2.4.1 Preparation of PMMA-PS cylindrical samples for dynamic experiments

The synthesized microcapsules were dispersed in a 2:1 by weight ratio of MMA/PS solution containing 5wt% of EDMA and 1 wt% of BPO. After removal of entrapped air by subjecting the mixture to a reduced pressure environment, 0.1 wt% of TMA was added to start the hardening of the resin. The PMMA-PS resin with 15 wt% of BB-filled microcapsules of different sizes (85, 60 and 45 μm) was injected into a long polyethylene cylndrical mold with a typical diameter of 1.5 mm. After 1 h the sample was removed from the mold. Full sample equilibration was ensured by storing the samples for 14 $days$ at ambient conditions. The hardened cylindrical PMMA-PS composite containing 10 or 15 wt% of BB filled microcapsules were cut to sample lengths of 2.5 mm and were scored using a miniature hand-held file 10-15 min before the actual experiment to introduce a guide for the crack-path as indicated in Figure 4.2a.

The modified cylinders were cracked by using a modified compression device suited for application inside the ESRF ID-19 set-up. Controlled fracture was accomplished by driving a wedge shaped piston inside the inserted score in the sample. Insertion of the wedge, with a slightly larger angle than the inserted score, created tensile stresses at the tip of the score. Typical forces of 20 N were used to vertically crack the sample along the groove to the substrate. This way the crack was orientated perpendicularly to the x-ray beam. A set-up of the modified compression set-up inside the x-ray beam is shown schematically in Figure 4.2b.

4.2.4.2 X-ray microscopy and microtomography

The dynamic X-ray microtomography experiments were carried out using synchrotron x-ray tomography at the ID-19 beamline station at ESRF in Grenoble, France. For the data collection the beam energy was set to 33 keV. Tomographic datasets of virgin and fractured samples were acquired as a function of time from which three-dimensional reconstructions were produced. The tomographic datasets consisted of 720 views of the samples with 0.25^o

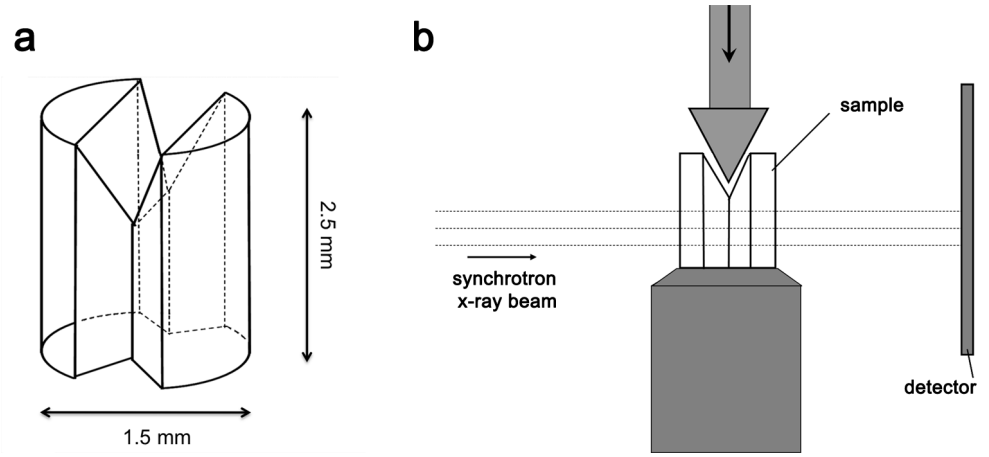

Figure 4.2: a) Typical sample geometry for the dynamic studies of healing-agent release and b) experimental set-up for the controlled fracture and image recording at the synchrotron beamline ID-19

rotations of the samples between each view. In order to reduce radiation damage to the samples, the total recording time was kept minimal and set to only 13 ms per image. The total time per scan over over 180^o therefore was approximately 10 s. The image at the detector was binned to 4x4 of the original.

The data were processed using an ESRF reconstruction software for tomographic reconstruction, converting the obtained projections into a series of X-Y plane slices down the longitudinal axis of the cylinder. The reconstructed data were imported into a commercial available software platform (AMIRA [81]), for segmentation and analysis.

4.3 Results and discussion

4.3.1 DCB and BB encapsulation

All synthesized UF microcapsules filled with DCB and BB were stable after drying and quite homogeneous in size as shown by a representative image for the DCB-filled microcapsules in Figure 4.3a. Figure 4.3b shows the capsule size distribution for these capsules. Statistically, the mean capsule diameter for all capsules synthesised was found to be: 60 μm with a standard deviation of 14 μm for the DCB-filled microcapsules and 85 $\pm$ 16, 60 $\pm$ 16 and 45 $\pm$ 10 μm for the BB-filled microcapsules. The mean diameters and size distributions were determined from sizing 200 individual microcapsules via optical microscopy.

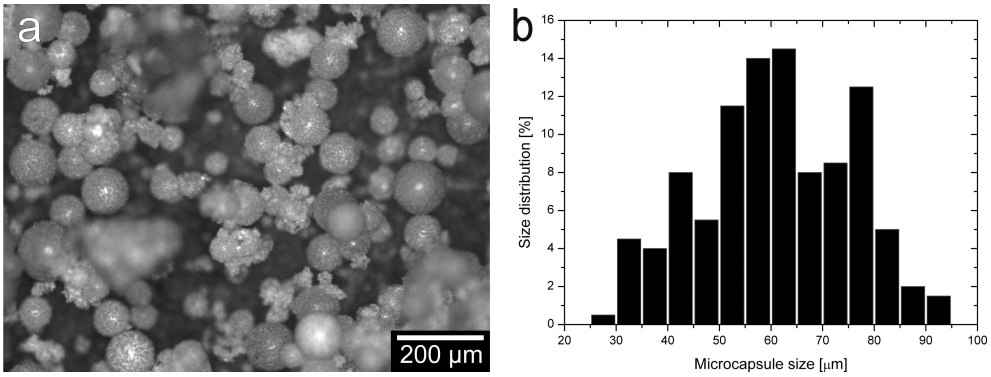

Figure 4.3: Laser scanning microscopy image of the UF DCB filled microcapsules and their size-distribution

4.3.2 Static determination of solvent release and crack-surface healing

4.3.2.1 The capsule/polymer system

The absorption and phase-contrast microtomography of the thermoplastic samples using the XuM produced data of sufficient resolution ($\approx$ 10 μm) to observe the capsules of solvent within the material and in particular their behavior around the crack zone. An example of an axial (X-Y) slice through the reconstructed volume is shown in Figure 4.4. The axial slice of the sample data clearly shows the dispersed filled (white) and several empty (black) microcapsules within the matrix material. The matrix itself appears to be inhomogeneous in density, observable by the different shades of grey. The light gray areas indicate material domains of higher density.

Inspection of all the tomographic slices throughout the reconstructed volume indicates

that denser regions of the polymer corresponded to the presence of empty capsules. From Figure 4.4a it can be observed that the high density areas are predominately surrounding the empty and not the filled microcapsules. Low concentrations of empty capsules appear to be present throughout the matrix material and are the result of premature rupture due to processing, storage or low pressure environment.[24] This caused the release of high density solvent and allowed solvent penetration into the thermoplastic material. The solvent absorbance increased the local density of the capsule surrounding matrix, leading to stronger absorption of the x-rays and a lighter shade of grey in the reconstructed image.

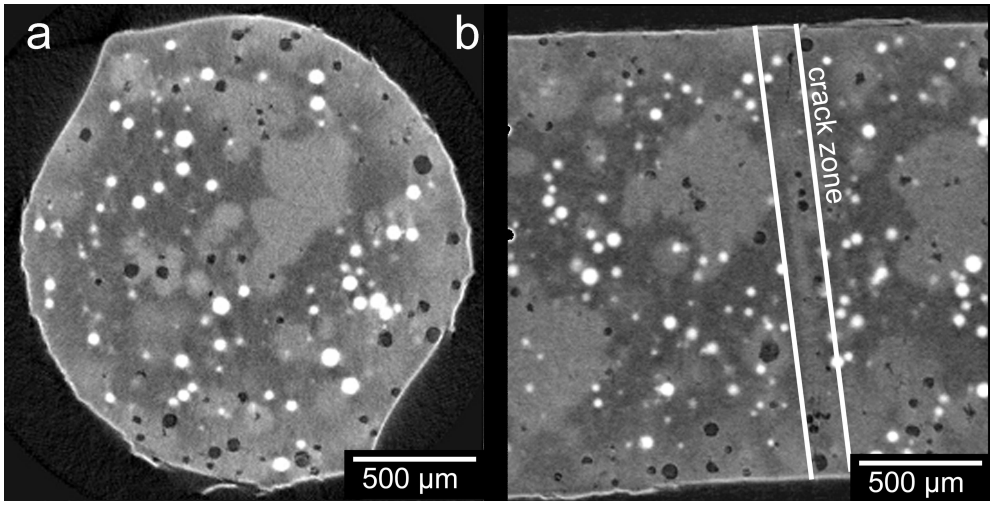

Figure 4.4: a) Axial tomographic slice through the reconstructed volume, clearly showing filled (white) and empty (black) capsules. Additionally, density variances in the matrix can be observed. b) Tomographic slice of a longitudinal section through the reconstructed volume, indicating the nearly disappeared fracture line. Lighter grey indicates higher density.

4.3.2.2 Crack-zone investigation after healing

To clarify and quantify the healing mechanism, the volume around the crack-zone was investigated in more detail by SEM-based microtomography. A longitudinal cross-section from the obtained data is displayed in Figure 4.4b. Similar to the earlier presented axial slice of the reconstructed volume, filled (white) and empty capsules (black) can be observed. In this image the crack-zone can also be identified. Since the fracture line is hard to detect the image demonstrates that the solvent-promoted healing made the crack disappear almost completely. The released solvent was spread over the surface areas, bridged the crack and allowed closure of the crack by an increase in molecular mobility in the solvent swollen regions and re-entanglement of the polymeric chains.

Further examination of the fractured and healed samples axial tomographic slices (par-

allel to the fracture plane) using intensity segmentation shows that there is a clearly visible higher concentration of empty capsules nearer to the fracture line. It is expected that the fracture process will rupture adjacent capsules, releasing the solvent so that most of the capsules in the region of the crack will be empty whilst further away most capsules will still be filled. To prove the proposed mechanism, the reconstructed segments were colour labelled and the full volume was displayed using 3D rendering. The 3D representations of the examined composite are given in Figure 4.5. In addition to the 2D tomographic slices, these figures show the spatial dispersion of filled (purple) and empty (green) capsules within the matrix material and unambiguously demonstrate the high concentration of ruptured capsules (Figure 4.5a) and the absence of filled microcapsules at and around the healed crack in the center of the image (Figure 4.5b). In addition to the large excess of empty capsules at the crack zone, several empty capsules can be found away from the crack, which agrees with the observations of Figure 4.4a and 4.4b. In Figure 4.5c a 2D axial section of the segmented data is displayed, which is taken at the position of the crack (the segmented matrix material is coloured yellow). Looking top-down at the crack plane, empty capsules are abundant at this location, whereas there are only a few filled capsules. In addition to the observed capsules also a large void (black area) is detected in this slice. The void indicates that this part of the fracture surface was not rebonded during the healing period, locally leaving a small volume of air at the crack.

The volume reconstruction gives not only the opportunity to qualitatively observe the features of the matrix material and the embedded microcapsules, it also allows quantitative analysis of the segmented areas.

4.3.2.3 Analysis of the distribution of full and empty capsules

The fraction of filled and empty capsules in regions around the healed crack was determined *via* an additional analysis of the 3D data. The change in the concentration of the two capsule types could be quantified by extracting the average proportion of full versus empty capsules down through the stack of slices.

In order to reduce the data noise the concentration of empty capsules was determined over stacks of 20 slices (*i.e.* the typical capsule diameter). The fracture plane of the sample was roughly parallel to the axial slices so that the crack region was hence confined to a small number of slices in the middle of the volume. Analysing the capsule concentration as function of Z is therefore a sensitive test to quantitatively determine the distribution of both capsule types around the crack. Comparable fraction analyses in morphology studies were presented earlier by Maire *et al.*[82]

The first stage of the analysis involved a discrete segmentation of the data into four zones: sample-exterior, polymer matrix, filled capsules and empty capsules. This process was carried out using the segmentation tool that comes with the AMIRA software package.[81] The data were initially smoothed slightly using a 3D, 3-pixel median-filter and then the majority of the segmentation was carried out using thresholding of grey levels, in order

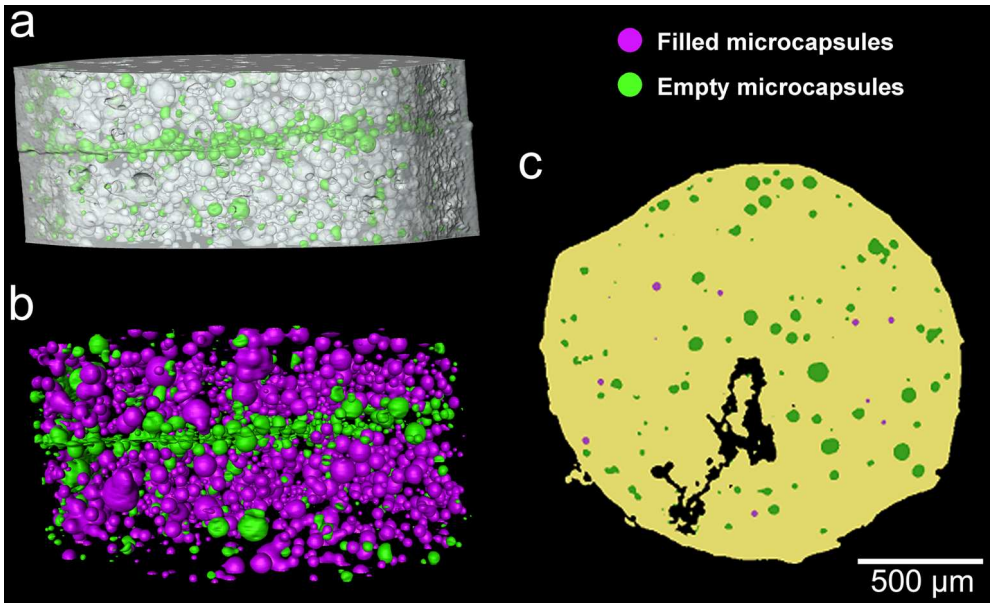

Figure 4.5: Reconstructed tomographic views: a) a 3D rendered dataset of 200 slices including the crack and the segmented empty capsules, b) the segmented microcapsules only, (c) a 2D segmented slice of the data at the crack.

to remove spurious signals. The region of the crack was segmented manually as part of the sample-exterior to prevent it from adding to the apparent volume of empty capsules. The proportions of each segmented region (segmented amount of voxels / total amount of voxels) are plotted against the Z position in the volume and show the concentration of filled and empty capsules as function of the distance to the crack (Figure 4.6). At large distances from the crack the total amount of filled and empty microcapsules/matrix ratio (*ca.* 12 $vol\%$) agrees very well with the 11.5 $vol\%$ (= 15 $wt\%$ with a capsule/matrix density ratio of 1.3) at which the composite samples were prepared. The graph shows near the crack a local decrease in the number of filled capsules and a rise in the number of empty ones. Over a total length scale of ca. 150 μm ($\approx$ 2.5 x the mean capsule diameter) there is a depleted zone, covering both sides of the fracture line. This indicates that only similar healing conditions are applicable when a subsequent crack is formed at distances $>$ 75 μm from the healed crack.

The local decrease of the filled microcapsules concentration corresponds to the total amount of liquid released near the crack as a result of the material fracture. The amount of liquid discharged into the crack is a crucial parameter in the degree of healing for liquid based systems.[67] The released solvent volume can be determined by integrating the peak area of the filled microcapsule curve. This integral gives the total decrease in filled capsules over the width of the crack and results a released volume of 0.25 x10^8 μm^3 (= 0.025 μl).

Assuming that the crack area to be healed is more or less equal to the total surface area of a single tomographic slice at the crack, *i.e.* 2.6 x10^6 μm^2 (= 2.6 mm^2), the presented material system ($\approx$ 60 μm microcapsule and loading of 15 $wt\%$) can be characterised by a healing agent release of 0.0096 $\mu l/mm^2$.

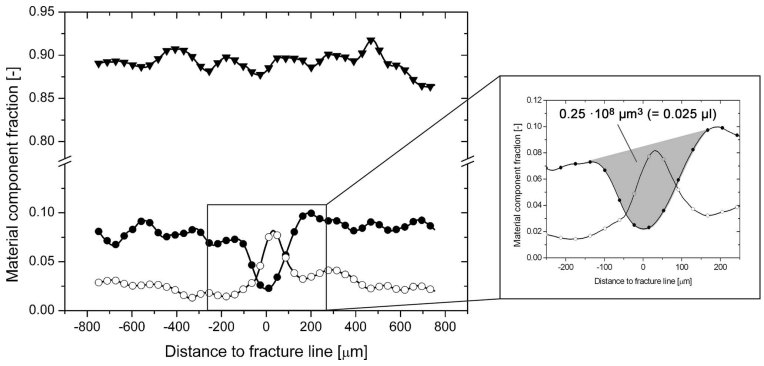

Figure 4.6: Plot of the material composition ratio as function of the distance to fracture line. The material composition ratio is given for the three material parts: filled capsules, empty capsules and matrix material.

Theoretically, the liquid release of a given capsule matrix volume element can be predicted by calculating the probability of a microcapsule being intersected by a unidirectional crack; assuming microcapsule uniformity. The fracture probability for a single microcapsule is given by:

$$\Psi = \frac{dA}{V} \tag{4.1}$$

in which d is the capsule diameter and A is the crack area and V is the total volume of the sample. Hence, the total number of capsules intersected by an intersecting plane, n, is given by:

$$n = \Psi N = \frac{dA}{V} N \tag{4.2}$$

N is the total amount of spherical capsules present inside the volume element.
Since

$$N = \frac{\phi V}{V_{caps}} \tag{4.3}$$

in which V_{caps} is the single capsule volume, eq. 4.2 can be rewritten as:

$$n = \frac{\phi dA}{V_{caps}} \tag{4.4}$$

from which it directly follows that volume released per crack area is given by:

$$\frac{V_{released}}{A} = nV_{caps} = \phi dA \tag{4.5}$$

Equation 4.5 shows a linear dependency for the released volume with the capsule volume concentration (ϕ), capsule diameter (d). Now, by simply filling in eq. 4.5 with the parameters for the system examined, $\frac{V_{released}}{A}$ results in a value of 0.0069 $\mu l/mm^2$. This volume agrees rather well with our measured value. The value found in our measurements is slightly higher than the theoretical value since it is observed that capsules at larger distances than d are ruptured by the crack as well.

4.3.2.4 SEM imaging of re-fractured surfaces

Following microtomographic analysis the healed sample was re-broken and SEM images of the fracture surfaces were acquired. Two of these images are shown in Figure 4.7. The SEM images exhibit the ruptured microcapsules at the crack and show regions with different texture around them. Smooth regions (dark) where the surface looks like a fresh fracture are observed, together with other more rough regions (light) where there was healing. At the bottom side of Figure 4.7a a larger unhealed area can be observed. As the sample was brittle and snapped completely in two, the presence of unhealed area may either be because of imperfect alignment of the cracked surfaces or due to loss of material during cracking. In both cases this could lead to larger crack sizes, which are unable to heal. Looking at the position of this area it corresponds to the black void detected in our tomographic measurements (Figure 4.5).

When studying the surface in more detail we also observe partly healed rivulets with rough texture running through smoother areas that did not heal across the crack. The rivulets illustrate the boundary of the solvent wetted area on the fracture surface. In particular the high magnification image (Figure 4.7) shows a well healed area on the left of the image (solvent wetted) and a less well healed area on the right (non-wetted) with the rivulets in between. These features correspond nicely to the well healed and poorly healed parts of the crack plane deduced from the microtomographic measurements.

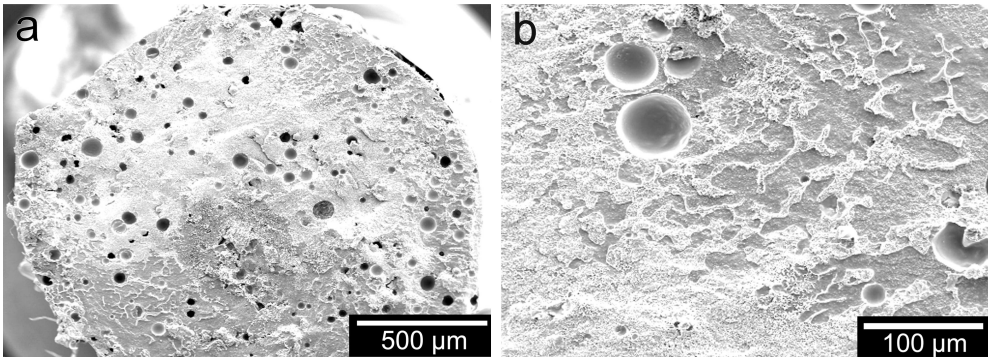

Figure 4.7: SEM images of refractured sample showing the ruptured microcapsules at the crack (a) and the different material textures on the crack surface. The lower image (b) shows the healed region on the left and the partly healed rivulets on the right.

4.3.3 Dynamic evaluation of the healing-agent release and solvent-matrix sorption

Using synchrotron radiation, fast tomographic scans allow a detailed investigation of the solvent release and solvent sorption within minutes after crack formation.

Experiments on virgin material samples showed comparable characteristics as recorded with the XuM. Similarly to the SEM-based technique, filled and empty microcapsules can be identified inside the material matrix and x-ray microscopy images also show regions of increased density around the empty capsules. However in the synchrotron experiments the fraction of empty microcapsules and the volume fraction of matrix material with increased density is found to be significantly higher. The latter is found to be the direct result of the sample handling, in particular the filing of the grooves just prior to the loading experiment. In retrospect the grooves should have been created by proper shaping the mold, rather than by mechanical means, unavoidably leading to capsule rupture. Despite the preliminary loss of healing-agent, sufficient solvent-filled capsules remained inside the material for evaluation of the solvent release kinetics.

4.3.3.1 Capsule/matrix investigation after cracking

Introduction of a crack in the sample caused rupture of the microcapsules in the crack-path and at a limited distance away from the crack as discussed earlier in the previous sections. In contrast to expectations, the solvent release from the capsules outside the direct line of the crack in these systems is not quasi instantaneous but occurs over a period of minutes after cracking. The reconstructed tomographic slices at a position just below the crack-tip clearly show how several embedded capsules appear to be intact after introduction of a crack

but release the solvent into the matrix up to 20 *min* after crack formation (Figure 4.8).

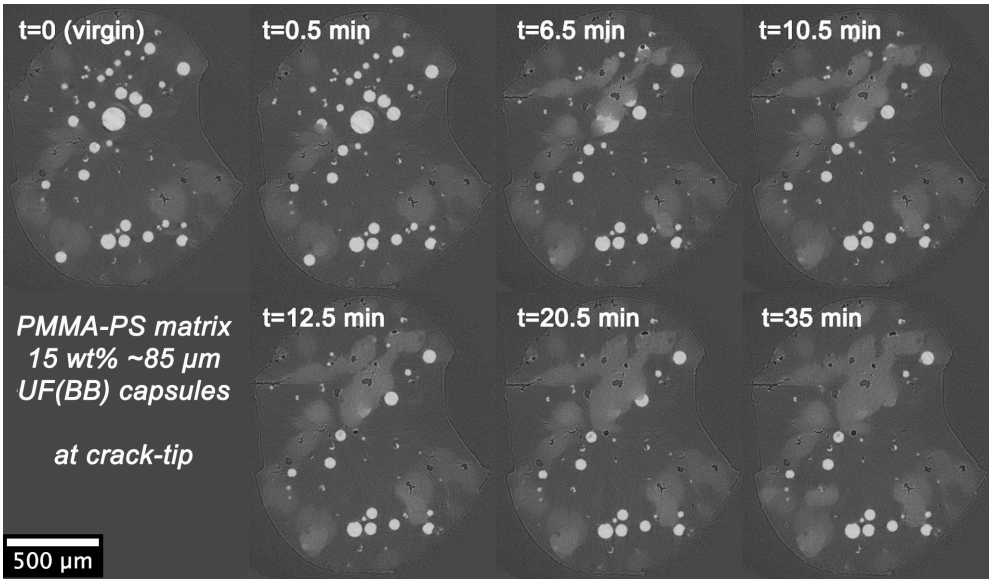

Figure 4.8: A X-Y tomographic slice showing the embedded microcapsules inside a virgin PMMA-PS 15 wt% 85 μ UF(BB) sample and at a position below the crack-tip as function of time

The solvent is absorbed by the PMMA-PS matrix after capsule rupture which leads to a detectable volume of solvent affected matrix around the position of the capsule. This affected volume increases slightly in time as the solvent penetrates further into the matrix but does not show full homogenisation over the measuring time of the experiment (35 *min*). The solvent remains in high concentration around the ruptured capsule and solvent 'clouds' of approximately twice the capsule diameter can be observed. This effect is advantageous for achieving a strong depression of the local glass transition temperature around the crack, thereby increasing the molecular mobility (see Chapter 2). However subsequent removal of the solvent from the healed area by solvent diffusion trough the volume towards an equilibrium concentration cannot be achieved. Solvent evaporation should therefore be accepted as the predominant process of solvent removal and the recovery of properties.

From full 3D analysis and segmentation of the data-sets on the solvent sorption around the crack it can be observed that the solvent spreading inside the crack for PMMA-PS matrices is minimal and absorption of solvent into the matrix is very fast. Figure 4.9 illustrates the evolution of solvent absorption by the matrix after fracture as a function of time. The volume of solvent affected material is segmented from the matrix volume and is indicated by the yellow coloured phase.

For purpose of reference, the segmented volume of the microcapsules (purple) and the

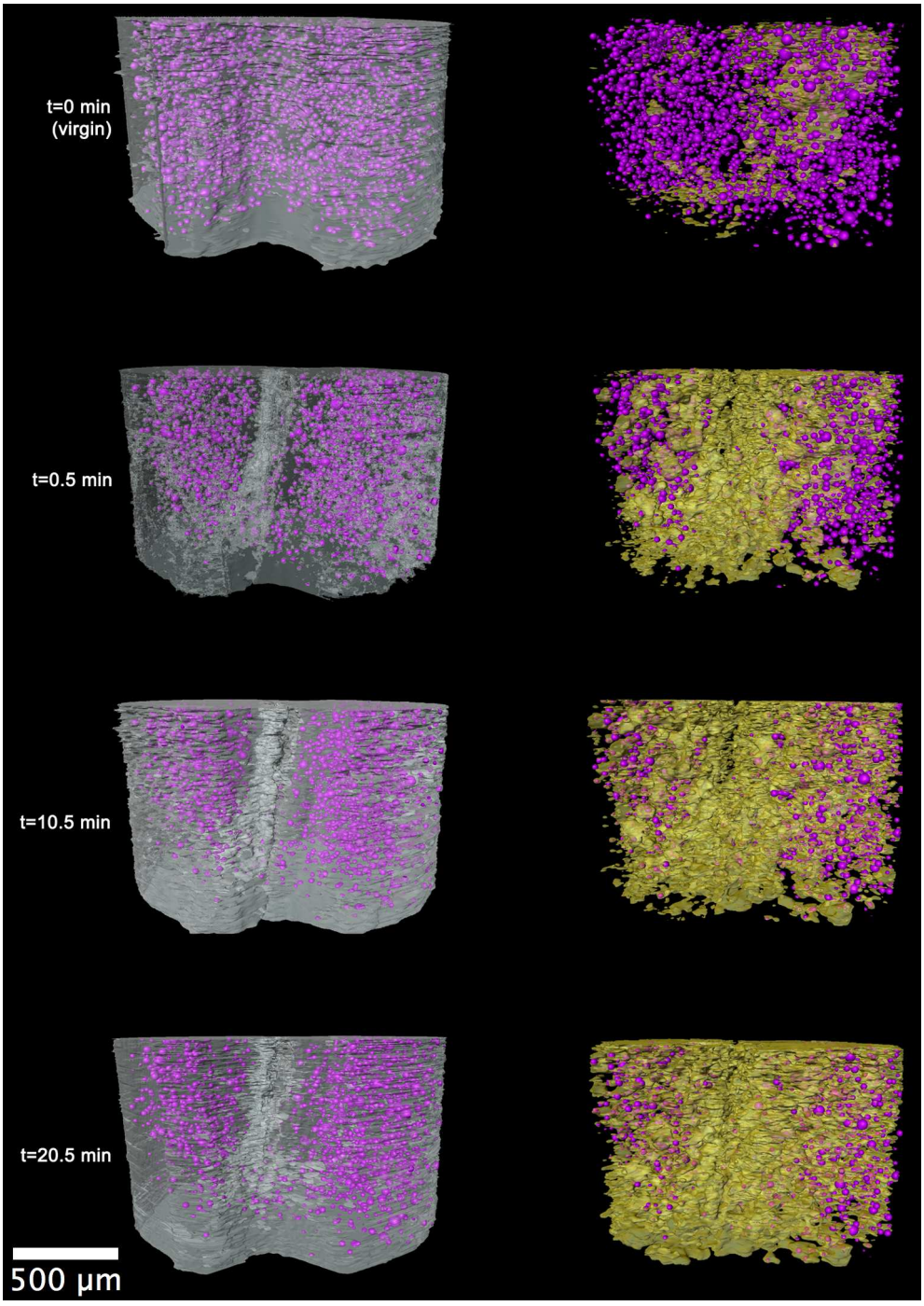

Figure 4.9: Evolution of the matrix solvent absorption after crack introduction for a 15 wt% *ca.* 45 μm UF(BB) PMMA-PS system

matrix material (white) is also given in Figure 4.9, showing where the crack was introduced. In Figure 4.9 at t=0 *min* a small volume of solvent affected matrix can already be detected in the virgin sample prior to cracking, caused by the preliminary rupture of capsules. At t = 0.5 *min* after fracture the large volume of solvent absorbed around the crack is clearly visible. It is shown by the subsequent images at t = 10.5 and 20.5 *min* that the affected volume expands slightly away from the crack in time, which is caused by limited diffusion and delayed capsule depletion outside the crack-line.

4.3.3.2 Radiation damage

Besides the rupture of the capsules around the crack, analyses of the BB-filled capsules well separated from the fracture surface indicate that additional capsule depletion can be detected, mainly at the edges of the sample in time. The unexpected loss of filled capsules at these locations is related to radiation damage caused by the high intensity synchrotron x-rays. In order to study the effect of radiation damage caused by the technique, a non-loaded control sample was subjected to a series of scans and the concentration of filled capsules was monitored over time. These experiments indicate that the volume of capsules decreases by approximately 1% per scan. Hence, the intensity of the beam and exposure time of the samples should be kept to a minimum.

4.3.3.3 Analysis of the released solvent volume and fraction of solvent affected volume in time

Detailed segmentation of the different features within the broken sample allows the quantification of the reduction of filled microcapsules (released solvent volume) and the affected volume by the solvent in the vicinity of the crack. Figure 4.10a displays the released volume per crack area for samples with different capsule sizes as a function of time after fracture. In accordance to Figure 4.9 the curves show that a large amount of solvent is released upon crack formation for all microcapsule sizes investigated and confirm that the volume of solvent released increases slightly in time. The trend of released volume increasing with capsule diameter is in agreement with predictions based on eq. 4.5. However, for these experiments the absolute amount of released solvent per crack area is substantially larger than theoretically predicted. It is rationalised that under the experimental conditions used, compression forces cause capsules to rupture even in the absence of a crack. Tomographic experiments under static load have indeed confirmed this hypothesis.

The evolution of solvent affected volume with time is displayed in Figure 4.10b. This figure shows that virgin samples already have a significant amount of solvent affected fraction due to the preliminary capsule rupture. For all three curves the fraction of solvent in the matrix increases in time, which corresponds to the decrease in filled capsules shown in Figure 4.10a. The rate of increase after fracture however depends on the capsule diameter and shows a delay for larger capsules. The sorption of solvent into the matrix is initially

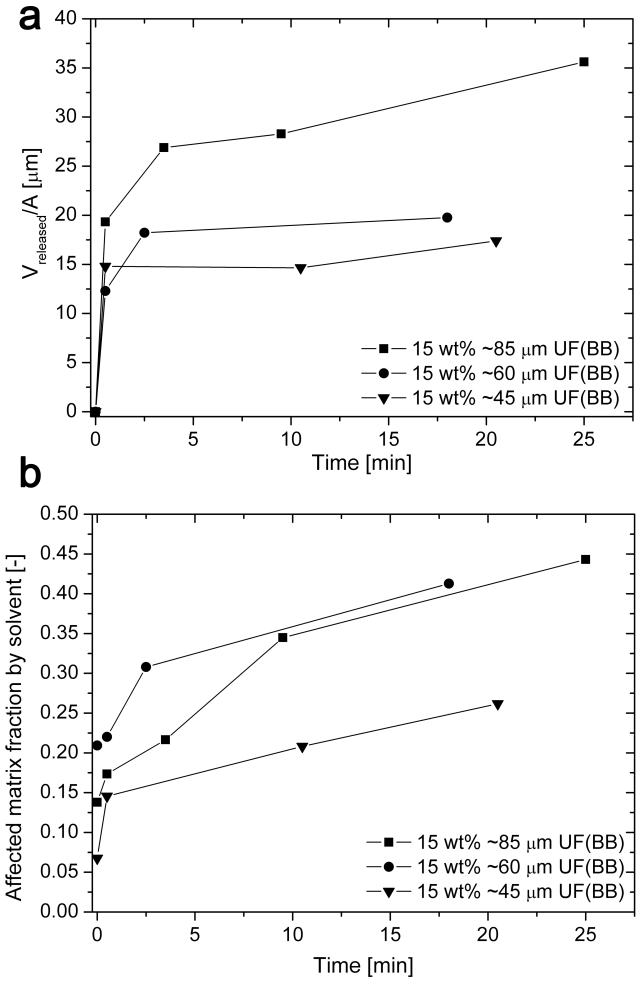

Figure 4.10: a) The released solvent volume per crack area and b) the fraction of solvent affected matrix as a function of time for PMMA-PS matrices embedded with UF(BB) microcapsules of different sizes

retarded for larger microcapsules due to their small surface to volume ratio. At longer time the increase in the solvent fraction is found to be more or less comparable for all three capsule sizes.

The tomographic experiments have shown that solvent sorption is fast and nearly all the solvent released is directly absorbed by the material without spreading inside the crack. It was suggested in Chapter 2 that spreading of the solvent should be fast in comparison to the solvent absorption in order to achieve optimal healing. Hence, on the basis of these data,

selection of a pure PMMA matrix for future experiments using solvent filled microcapsules would be advisable in order to get better crack wetting and more homogeneous crack-healing.

4.4 Conclusions

3D microtomography coupled with image segmentation and analysis allowed a quantitative analysis of the fracture and release processes in a microcapsule based self-healing thermoplastic material.

Static evaluation of the solvent release indicated the presence of a distribution of full and empty capsules throughout the sample as a consequence of crack formation. From the tomographic data it can be concluded that there was good healing across a sizeable fraction of the crack, which is in agreement with an SEM investigation. More detailed segmentation showed that total amount of solvent released at the crack could be determined by quantitative analysis of data after healing. The measured value of the released solvent volume is in good agreement with the theoretical value found *via* statistical calculations.

Dynamic studies on the liquid release as a function of time after fracture showed that microcapsules outside the direct crack-path show an unplanned delayed rupture and healing-agent release which depends on the capsule size. The volume of released solvent in the PMMA-PS matrix is absorbed by the matrix at a fast rate and forms a cloud-like domain of high solvent concentration around the original position of the capsule. Homogenisation of the solvent in time throughout the volume does not occur. In order to achieve optimal healing, better spreading of the solvent inside the crack is required, which could be achieved by selection of a more solvent resistant matrix material.

Having demonstrated the ability to observe the processes of fracture and healing of thermoplastic materials, microtomography offers potential for characterisation of many other self-healing materials such as microvascular systems and hollow fibre composites.

CHAPTER 5

Binary microcapsules containing two liquids

> The person who says: "it cannot be done", should not interrupt the person doing it.
>
> *Chinese proverb*

5.1 Introduction

As presented in the previous chapters the use of microcapsules as liquid storage containers inside structural materials has received great interest in the community dedicated to the development of self-healing polymer systems.[18] In such systems, microcapsules act as a storage medium for liquid monomers inside a polymer matrix and release their reactive contents upon fracture of the surrounding material. Microencapsulation of liquids is a widely used technique to store and protect functional liquids from the external environment and to handle them as solids. Many review articles and books have been published on the subject,[83–85] addressing numerous techniques to create a wide variety of liquid filled microarchitectures. These methods include for example the use of polymers,[86] liposomes[87] and silica[88] to encapsulate various organic and non-organic liquids in core-shell particles. Many of these particles not only vary in shell type material and liquid core but sometimes also exhibit complex architectures enlarging their potential in a wide variety of products ranging from carbon copy

[0]Based on: S.D. Mookhoek, B.J. Blaiszik, H.R. Fischer, N.R. Sottos, S.R. White and S. van der Zwaag, *J. Mater. Chem.*, 2009, **18**, 5390-5394

paper to drug delivery systems, and food additives.

In order to design new microcapsules containing reactive liquid media for self-healing materials, we investigated the possibility of creating a novel capsular architecture that has two individually stored liquid phases and is able to release them upon capsule failure. The simultaneous release of two components at close proximety could overcome disadvantagous effects of currently used binary resin systems, *e.g.* epoxy plus hardner, related to stoicheometry and mixing time. Different designs of microcapsules in which multiple liquids are stored separately, made by double emulsion methods, have been reported before.[89–92] The approach reported here is not based on such a strategy, but employs a surface stabilization technique to encapsulate two liquids in a single microcapsule.

In this chapter carefully synthesized poly(urea-formaldehyde) (UF) microcapsules containing a liquid core are employed to stabilize oil/water emulsions. *Via* this route a new microcapsule and colloidosome architecture[93] is created that has a central liquid core decorated at its periphery with microcapsules containing the secondary liquid. It presents the two-step preparation procedure and the characterization of these binary microcapsules. A schematic of the proposed microcapsular architecture is shown in Figure 5.1.

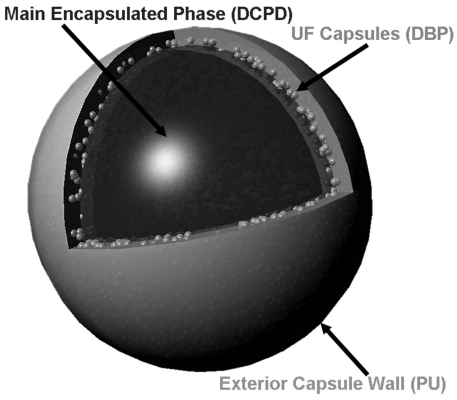

Figure 5.1: Schematic representation of the binary microcapsule architecture.

5.2 Background

Solid particles can create stable liquid dispersions by a phenomenon known as Pickering stabilisation[94] and offer interesting design tools for liquid encapsulation. Ramsden[95] and Pickering[94] were the first to report that particles can adhere to liquid-liquid interfaces and stabilize emulsions. Later Finkle *et al.*[96] and Pieranski[97] found that the explanation for such strong adherence of particles at liquid-liquid interfaces lies in the fact that the particles are partly wettable by the two phases and that the depth of the surface energy well is a function of temperature, particle size and surface tension. In addition to this, Leunissen *et al.*[98] recently also reported the influences of electrostatic interactions of charged-induced particles.

The position of a particle at a two-phase interface is based on capillary forces. To keep a particle at the interface of two inmiscible liquids, the total energy of the system should be minimal to create a stable equlibrium (neglecting gravitational influences). It can be derived that the total energy contribution of the two liquids and the adhering particle can be described by the following equation:[97]

$$E_s = E_{12} + E_{P1} + E_{P2} \qquad \begin{cases} E_{12} = -\sigma_{12}\pi r^2\left(1-\tilde{z}_0^2\right) & \text{liquid1-liquid2,} \\ E_{P1} = \sigma_{P1}\pi r^2\left(1+\tilde{z}_0\right) & \text{particle-liquid1,} \\ E_{P2} = \sigma_{P2}\pi r^2\left(1-\tilde{z}_0\right) & \text{particle-liquid2,} \end{cases} \tag{5.1}$$

where σ's are the corresponding interfacial tensions of the liquid-liquid and particle-liquid interfaces and $\tilde{z} = z/r$ is the relative distance of the center of the particle to the liquid-liquid interface with respect to the particle radius. Figure 5.2 displays the surface energy profile of a stabilizing particle at the interphase of two liquids.

The summation of the three surface energy contributions converts into a parabolic description of the total surface energy as function of the patricle position with respect to the liquid-liquid interface:

$$E_s = \sigma_{12}\pi r^2\left[\tilde{z}_0^2 + 2\left(\frac{\sigma_{P1}-\sigma_{P2}}{\sigma_{12}}\right)\tilde{z}_0 + 2\left(\frac{\sigma_{P1}+\sigma_{P2}}{\sigma_{12}}\right) - 1\right] \tag{5.2}$$

which has a minimum at a value $\tilde{z}_m = \frac{\sigma_{P2}-\sigma_{P1}}{\sigma_{12}}$.

When the particle is moved away from the interface into either of the two liquid phases the total surface energy goes up. Hence, the most energetically favourable position for the particle in a two phase system is at the interface, lowering the total surface energy between the two liquids. As is derived from the minimal surface energy, the stabilization effect of a particle at a liquid-liquid interface, is governed by its surface properties, *i.e.* interfacial tension. By choosing different surface interactions researchers have been able to adjust

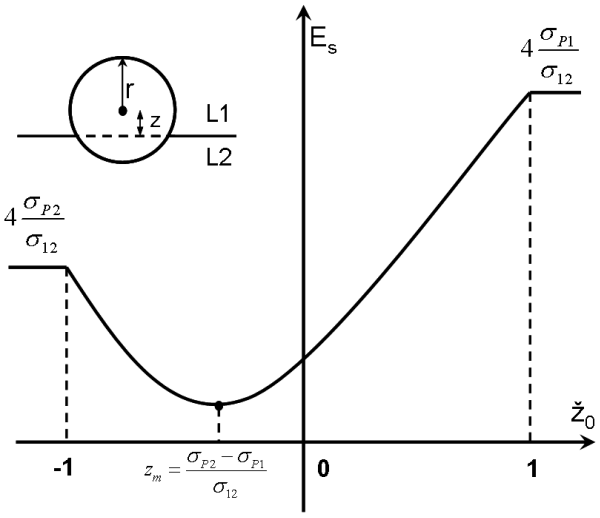

Figure 5.2: Energy profile for a spherical particle sitting at a flat two-liquid phase interlayer based on capillary forces. Reproduced after Pieranski[97]

the stabilization and develop new materials to create particle stabilized emulsions. Besides commercially available inorganic nano-particles (*e.g.* clays etc.), different types of polymer particles have previously been shown to be suitable Pickering stabilizers. The most common examples of polymeric particles used as Pickering stabilizers are solid polymethyl methacrylate (PMMA) and polystyrene (PS) microspheres.[93,99]

Since the stabilizing phenomenon is only surface related, core-shell particles similar to solid bodied particles are able to create Pickering emulsions. The use of core-shell particles as Pickering stabilizers has not yet been reported before but offers large potential to create complex and multiphase component microcapsules.

5.3 Experimental

5.3.1 Materials

All materials were used as received without further purification. Urea, resorcinol, ammonium chloride (NH_4Cl), dibutylphthalate (DBP), trimethylol propane (TMP) and perylene fluorescent dye were all purchased from Sigma-Aldrich (USA). Dicyclopentadiene monomer (DCPD, 95% endo) was ordered through Acros Organics (Belgium). Formaldehyde 37% in water solution was obtained from Fischer Scientific (USA). Ethylene-maleic anhydride copolymer (EMA) was purchased from Zeeland Chemicals (Zeeland MI, USA). Airthane PHP-80D polyurethane pre-polymer (NCO content 11wt%) was kindly provided by Air Products (USA). Epikote 828 and diethyltriamine (DETA) were purchased from Miller-Stephenson (USA).

5.3.2 Preparation of binary microcapsules

Synthesis of liquid filled Pickering stabilizers Core-shell particles (urea-formaldehyde microcapsules) with dibutylphthalate as their core material were used as Pickering stabilizers. They were synthesized according to the method described by Blaiszik *et al.*[100] To encapsulate DBP, 5.5 ml of the liquid was emulsified at room temperature in water containing urea and resorcinol using a polymeric surfactant, ethylene-maleic anhydride copolymer, in combination with a sonication treatment (Cole-Palmer ultrasonic homogenizer 750 W at 40% intensity) and a high shear-rate impeller. For spectroscopic reasons, a small quantity (0.01 g/ml) of perylene fluorescent dye was pre-dissolved in the oil phase. Subsequently, an *in-situ* polymerization reaction between urea and formaldehyde at 55^oC for 4 h was used to encapsulate the DBP within a polymeric (UF) shell wall.[66] When the reaction was ended the resulting urea-formaldehyde capsule suspension was centrifuged, decanted and redispersed in de-ionized H_2O five times to remove the free EMA polymeric surfactant.

Synthesis of micronsized UF resin particles To demonstrate that micron-sized particles of UF resin were able to stabilize liquid-liquid interfaces, dispersed UF resin was synthesized similarly as described in the the previous paragraph, ommiting the addition of EMA surfactant and DBP, adjusting the pH at 2.00 by using a small quantity of [0.5 M] HCl solution. The reaction was terminated after 2 h by a small addition of NaOH neutralizing the mixture (pH 7.00), resulting in suspended UF resin particles of approximately 2 μm in size.

Synthesis of binary microcapsules The binary capsule structures with dicyclopentadiene (DCPD) as the core material were made by preparing a water/DCPD (vol: 50 ml/10 ml) mini-emulsion using 0.5 g of NaCl and 0.28 g of the earlier synthesized ca. 1.4 μm DBP filled UF microcapsules as Pickering stabilizer without addition of surfactant. Using a

standard laboratory mechanical impeller at 400 *rpm* the water/DCPD dispersion was agitated until the dispersed DCPD was homogenized and non-coalescing at elevated temperature within the time of capsule preparation.

Prior to the emulsification, 1.5 *g* Airthane PHP-80D polyurethane (PU) prepolymer was dissolved in the DCPD. The stable emulsion was then heated to 60°C and the PU microcapsule shell wall was created by the slow and dropwise addition of 10 *ml* [1.3 M] trimethylol propane (TMP)/water solution to the stirring emulsion. The addition of TMP started the interfacial polymerization[101] with the PU prepolymer dissolved in the DCPD. After 2.5 h reaction time, the created microcapsules were filtrated, washed, dried and sieved. The product yield was approximately 7.7 *g* on 9.82 *g* DCPD, 0.28 *g* DBP filled microcapsules and 1.68 *g* wall material (PU prepolymer + TMP). The terminology UF(DBP) on PU(DCPD) designates a polyurethane encapsulated DCPD core with UF(DBP) capsules in the shell wall. The binary capsule production procedure is outlined in Figure 5.3.

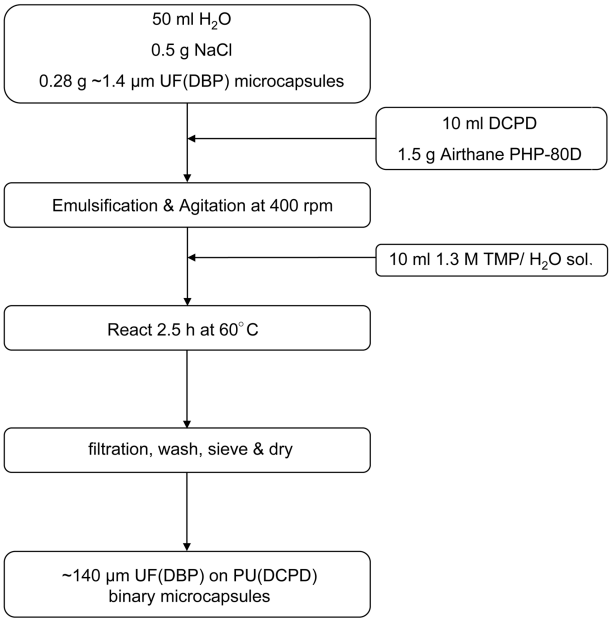

Figure 5.3: Production procedure for UF(DBP) on PU(DCPD) binary microcapsules

Preparation of binary capsule embedded epoxy resin The resin was prepared by dispersing 10 wt% of binary capsules in 6.0 *g* of Epikote 828 (bisphenol-A diglycidyl ether). Subsequently, 0.72 *g* of curing agent (DETA) was added and mixed-in with the resin. The entrapped air was removed under reduced pressure and the resin was poured into cylindrical

molds. The resin was cured over 24 h at room temperature and an additional 24 h at 35^{o}C. Epoxy samples containing the binary capsules were fractured using a razor blade.

5.3.3 Characterisation methods

Focused extinction particle sizing analysis The DBP filled UF microcapsule size distribution was determined by an AccuSizer FX focused extinction particle sizer (0.7 - 20 μm). The UF(DBP) microcapsule-water dispersion was diluted to create a stable semi-transparent microcapsule dispersion. Of this dispersion, 10 ml was analyzed and sizing was performed for approximately 10^6 particles.

Optical-fluorescent & electron microscopy studies The binary microcapsules were characterised using a Leica optical microscope (fluorescent mode). The DBP filled UF microcapsules were made visible by excitation of perylene dye (excitation ≈350-450, emission ≈450-550 nm). Using this technique, the location of the UF microcapsules in the binary capsule could be determined.

Scanning Electron Microscopy (SEM) studies were performed on a Hitachi S-3000N and Philips XL30 ESEM-FEG. Samples of both DBP filled UF microcapsules and binary microcapsules were deposited on carbon-coated tape and sputter-coated with Au/Pd.

Thermal analyses Differential Scanning Calorimetry (DSC) and Thermo-Gravimetric Analysis (TGA) experiments were carried out to characterise the binary capsules and determine the presence of the two liquid components. DSC was performed using a Mettler-Toledo DSC821e and TGA was carried out using a TGA/SDTA 851e. All experiments were conducted from 40^{o}C to 390^{o}C at a heating rate of 10 K/min under flowing N_2 gas.

Testing of mechanical properties The elastic modulus and failure behavior of the peripherally decorated binary microcapsules were determined through single-capsule compression tests according to Keller *et al.*[102] The compression displacement rate was 2.5 $\mu m/s$ using a stepper actuator (Physik Insturment M-230S) controlled *via* a computer interface and accurate to 50 nm. Load data were acquired from a 100 mN load cell (Transducer Techniques GSO-10) and associated software from National Instruments, giving a combined sensor system accuracy of ca. 100 nN.

5.4 Results & Discussion

5.4.1 Microcapsule characteristics & morphology

Urea-formaldehyde resin is found to have excellent surface properties to act as a material for Pickering stabilisation. For microencapsulation *via* an *in-situ* polymerisation this stabilising effect was observed earlier.[66] In the process of encapsulation *in-situ* created nanoparticles of UF percipitate from solution and condense at the interface of an oil in water emulsion, thereby creating a closed shell wall.

Addition of a small quantity, 0.5 g, of the synthesized solid UF resin particle suspension demonstrated that the presence of the UF enabled the surfactant-free emulsification of 2 ml DCPD in 10 ml de-ionized water after shaking. Without UF the two inmiscible liquids instantly phase-separated again after shaking with a DCPD layer on water. The result of this experiment is shown in Figure 5.4.

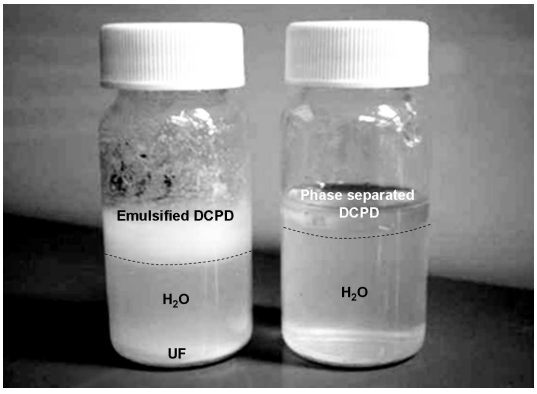

Figure 5.4: Two DCPD/water mixtures after shaking, (l) with addition of UF resin particles, (r) without UF resin particles. The excess of UF particles has percipitated to the bottom of the vial due to its larger density.

Synthesiszed DBP filled UF microcapsules were stable after drying and appeared homogeneous in size as shown in Figure 5.5a. Focused extinction demonstrated an average capsule diameter of 1.4 μm, with a standard deviation of 0.4 μm. A profile of the capsule size distribution can be found in Figure 5.6a.

Analogue to the experiment for solid UF resin stabilisation a stable DCPD/water Pickering emulsion was produced using the UF(DBP) microcapsules. An isocyanate-alcohol interfacial step-growth polymerization[101,103,104] was selected to fixate the assembled UF(DBP) capsules on the DCPD droplet and encapsulate the contents. The PU prepolymer (isocyanate end-capped) was dissolved in the DCPD prior to emulsification, and the TMP was added to the water phase. The insolubility of each component in the other liquid-phase leads

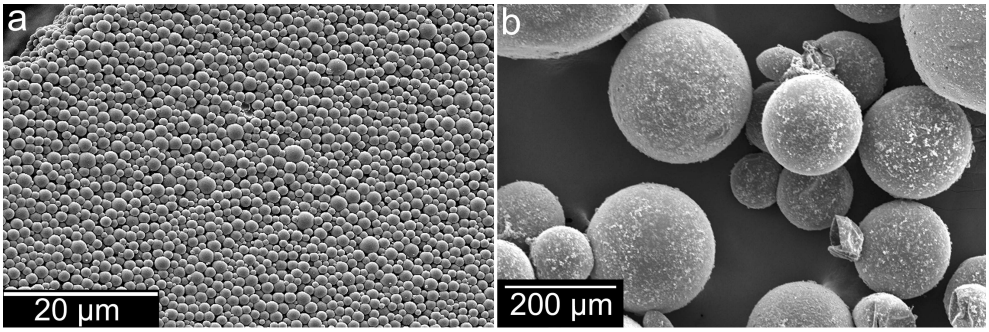

Figure 5.5: Electron microscopy images of a) UF(DBP) microcapsules prepared according to the method of Blaiszik *et al.*[100] after drying, b) binary UF(DBP) on PU(DCPD) microcapsules.

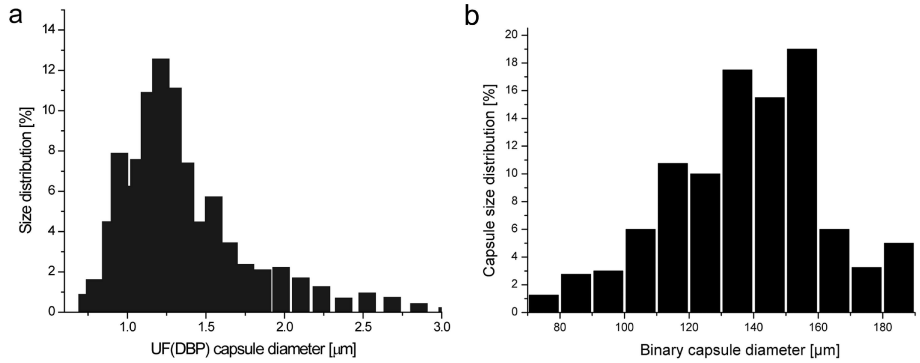

Figure 5.6: Capsule size distribution: a) UF(DBP) capsules, b) binary UF(DBP) on PU(DCPD)

to an interfacial polymerisation reaction only occurring at the liquid-liquid interface.[105,106] The fast polymerization between the -NCO end-groups of the PU prepolymer and the -OH end-groups of the TMP leads to the formation of an insoluble polymeric (PU) shell wall that encloses the UF(DBP) microcapsules at the oil/water interface into the shell wall of the larger microcapsule, creating the binary microcapsule architecture.

Figure 5.5b shows an SEM image of filtered and dried binary capsules synthesised with DBP filled UF microcapsules as Pickering stabilisers. The outer capsule morphology is characterised by a slightly rough texture which is a result of residual UF polymer particle adherence. The few observed buckled structures are caused by liquid depletion/evaporation in the SEM vacuum environment. These binary capsules had a mean diameter of 140 μm, with a standard deviation of 24 μm, which was determined from sizing 200 individual capsules

via optical microscopy (OM). The size distribution is shown in Figure 5.6b. After filtration, the binary capsules were air dried to produce a free flowing powder. The combined physical characteristics of the UF(DBP) and PU(DCPD) microcapsules are provided in Table 5.1.

Table 5.1: Microcapsule physical characteristics

Core	Shell	Shell wall thickness	Mean capsule diameter	notation
DBP	Urea-formaldehyde	$\approx 75\ nm^a$	$1.4\ \mu m$	UF(DBP)
DCPD	Polyurethane	$\approx$ 3-9 μm^b	$140\ \mu m$	PU(DCPD)

[a] Blaiszik *et al.*[100] for similarly prepared DCPD capsules of $\approx 1.5\ \mu m$ (determined from TEM images).
[b] Experiments indicate a strong dependence of the polyurethane capsule shell wall on the capsule diameter (determined from SEM images).

Upon excitation of the binary microcapsules in optical microscopy experiments, the UF(DBP) microcapsules fluoresce strongly. The microscope fluorescent image (Figure 5.7a) clearly indicates that light is emitted from the rim of the binary capsules. Hence, the UF(DBP) microcapsules are located on the periphery of the binary capsule surface. Scanning electron microscopy (SEM) of fractured microcapsules embedded in epoxy resin (Figure 5.7b) confirmed the capsular architecture. Image 5.7b shows the fractured shell wall and the rough exposed interior wall of a fractured binary microcapsule. The rough morphology on the shell wall indicates the presence of the UF(DBP) capsules in the shell wall, which is supported by the observation of ruptured UF(DBP) capsules visible on the shell wall fracture surface. The capsule architecture (depicted in Figure 5.1) is a direct result of the Pickering stabilization, the subsequent interfacial polymerization and the entrapment of the UF(DBP) microcapsules in the capsule wall. Due to the hydrophilic nature of the polyurethane polymer, the shell wall is created on the water side of the oil/water interface. Since the UF(DBP) Pickering stabilizers firmly adhere to the interface, they are fully incorporated into the shell wall. A similar morphology of peripherally organised colloidosomes was also reported by Bon *et al.*[107] who demonstrated the construction of binary hollow silica vessels *via* Pickering stabilization.

5.4.2 Binary capsule components analysis

The presence of both liquid components (DCPD and DBP) within the same structure was demonstrated by performing DSC and TGA analysis on the binary capsules. The data of both thermal analyses are shown in Figure 5.8. In both experiments, two separate transition processes were observed corresponding to the two encapsulated materials. The DSC plot showed two endothermic peaks representing the evaporation of the encapsulated DCPD and DBP with minima at 179°C and 313°C, respectively. By integrating the transition peaks,

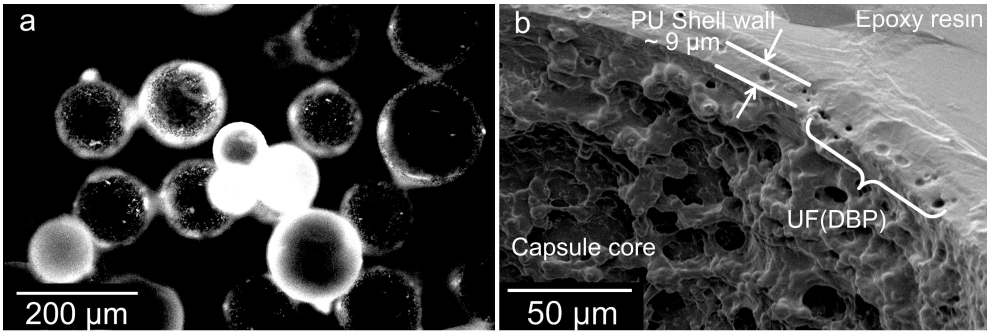

Figure 5.7: a) Fluorescent mode micrograph of the UF(DBP) on PU(DCPD) microcapsules. b) SEM image of a fractured UF(DBP) on PU(DCPD) capsule embedded in epoxy resin.

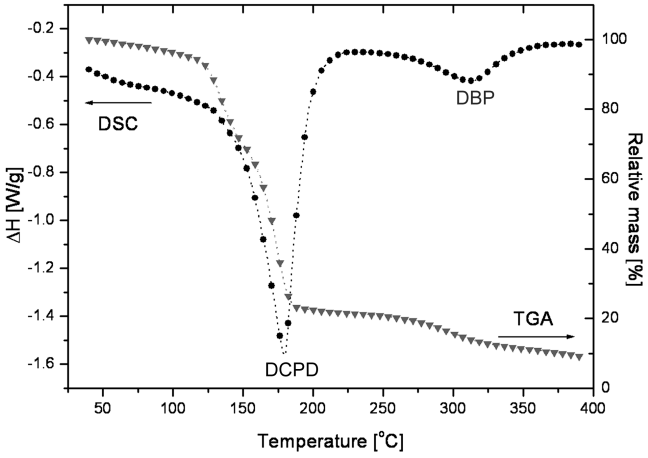

Figure 5.8: DSC (•) and TGA (∇) measurements of a UF(DBP) on PU(DCPD) binary system

the heats of evaporation for both liquids were determined. Using the measured specific heats of evaporation for the DCPD and DBP grades used, it was possible to calculate the volume ratio between the two components in the binary capsule structures. The volume ratio f_{Vol}^{Exp} is defined as follows:

$$f_{Vol}^{Exp} = \frac{V_{DBP}}{V_{DCPD}} = \frac{\Delta H_{DBP}^{Trans}}{\Delta H_{DCPD}^{Trans}} \frac{\Delta H_{DCPD}^{Vap}}{\Delta H_{DBP}^{Vap}} \frac{\rho_{DCPD}}{\rho_{DBP}} \tag{5.3}$$

In eq. 5.3, properties of each phase are expressed using V for the volume, ΔH^{Trans} to

represent the measured heat of evaporation, and ΔH^{Vap} and ρ as the specific heat of evaporation and the density of two encapsulated phases respectively. Using the data listed in Table 5.2 along with eq. 5.3, the DBP concentration was 8.8% by volume. TGA measurements of the binary capsules yielded a similar DBP concentration of 8.3% by weight.

Table 5.2: Component analysis of binary capsule by DSC

Component	$T_{peak}[^oC]$	$\Delta H^{Trans}[J]$	$\Delta H^{Vap}[Jg^{-1}]$	$\rho[gcm^{-3}]$	$V[cm^3]$
DBP	313	-0.22	-345.2	1.043	$6.1 \cdot 10^{-4}$
DCPD	179	-2.01	-296.3	0.982	$6.9 \cdot 10^{-3}$

Based on the average dimensions of the capsules shown previously in Table 5.1, the theoretical volume fraction of DBP was calculated assuming uniform spherical geometries and perfect hexagonal packing of the microcapsules:

$$f_{Vol}^{Theory} = \frac{V_{DBP}^{caps} \cdot n_{DBP}}{V_{DCPD}^{caps}} = \frac{\frac{1}{6}\pi d^3}{\frac{1}{6}\pi D_{eff}^3} \cdot \frac{\pi D_{eff}^2 \phi}{\frac{1}{2}\sqrt{3}d^2} = \frac{\pi d \phi}{\frac{1}{2}\sqrt{3}D_{eff}} \tag{5.4}$$

In eq. 5.4, V^{caps} is the calculated volume for the DBP and DCPD content of a single capsule and n is the number of UF(DBP) capsules on a binary capsule surface. Furthermore, d is the average UF(DBP) capsule diameter, $D_{eff} = D - 2h$ (where h is the PU shell wall thickness) is the inner polyurethane capsule diameter, and the parameter ϕ denotes the coverage fraction of the UF(DBP) microcapsules enclosed into the PU shell wall. When assuming a full monolayer droplet coverage, $\phi = 1$. Using the average geometric values in Table 5.1 the theoretical volume fraction of DBP is 3.6% with an absolute error of 1.6%, based on the polydispersity of the microcapsule size. The calculated volume fraction is only an estimate, taking into account its error, but indicates that more than a single monolayer of UF(DBP) microcapsules ($\phi > 1$) was enclosed into the binary capsule shell wall.

By combining eqs. 5.3 and 5.4, we derive an estimate for the experimental coverage fraction, ϕ_{Exp}:

$$\phi_{Exp} = f_{Vol}^{Exp} \frac{\frac{1}{2}\sqrt{3}D_{eff}}{\pi d} \tag{5.5}$$

Using the experimental data, a coverage fraction of 2.5 $\pm$ 1.1 is obtained. This value suggest that on average the total number of enclosed UF(DBP) particles exceeds the amount for a monolayer of hexagonal packed UF(DBP) colloidal capsules by a factor of approximately 2.

5.4.3 Mechanical properties

Individual UF(DBP) on PU(DCPD) microcapsules were mechanically tested in diametral compression, through which a value for the capsule shell wall modulus was derived according to the method described by Keller *et al.*[102] To study the influence of embedded peripherally micron-sized microcapsules in the larger microcapsule shell wall, similar polyurethane microcapsules containing DCPD were synthesized, substituting the UF(DBP) with a small quantity of EMA in the emulsification step. These microcapsules were synthesized comparably to their analogues and had a similar size distribution.

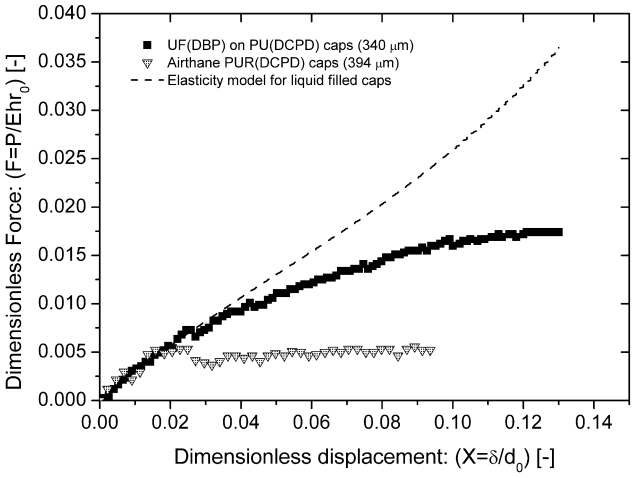

Figure 5.9: Dimensionless force-displacement curves for single microcapsule compression tests for UF(DBP) on PU(DCPD) and surfactant stabilised Airthane PU(DCPD) microcapsules with respect to the elasticity model for liquid filled microcapsules under compression[102]

Figure 5.9 shows two representative loading curves for the two types of microcapsules with similar diameter. The load and displacement have been converted to dimensionless values with $x = \delta/d_0$ (in which δ is the displacement and d_0 the initial capsule diameter) and $F = P/(Eh_0r)$ (in which P is the measured load, E the shell wall modulus, h_0 the capsule shell wall thickness and r the radius of the capsule). Since the microcapsule shell was was found to depend strongly on the capsule diameter similarly sized microcapsules were selected and the shell-wal thickness for each capsule tested was accurately determined by SEM or laser scanning microscopy. The shell-wall thickness together with the load displacement data enabled the calculation of the shell wall modulus *via* fitting the data to an elastic model for liquid filled shells presented by Lardner and Pujara[108] assuming a material Poisson's ratio of $\frac{1}{3}$. From the figure it can be observed that both type of microcapsules follow the elasticity model up to a comparable strain level where the capsule material appears to yield rather than fracture. At the strain of approximately 2% the loading curves deviate from

the model and show ductile deformation behaviour. When observing the failure mode of the microcapsule during testing the rubbery/plastic failure mode is also observed by tearing of the microcapsule rather than fracturing. The somewhat recorded higher values for the UF(DBP) of PU(DCPD) binary microcapsules is within error and is an effect of the slightly larger capsule diameter. The stiffness (before yield) of the microcapsules is also found to be comparable and is not influenced by the introduction of a binary phase encapsulated into the shell wall. Average values for the modulus of both type of microcapsules together with their standard deviation is given in Figure 5.10. Since the thickness of the shell wall exceeds the size of the UF(DBP) layer on average by a factor 2 most of the shell wall properties are governed by the polyurethane material. The average modulus values indicate the rubbery nature of the shell wall material and is found comparable to data provided by Air products of cured Airthane PHP 80D.[109]

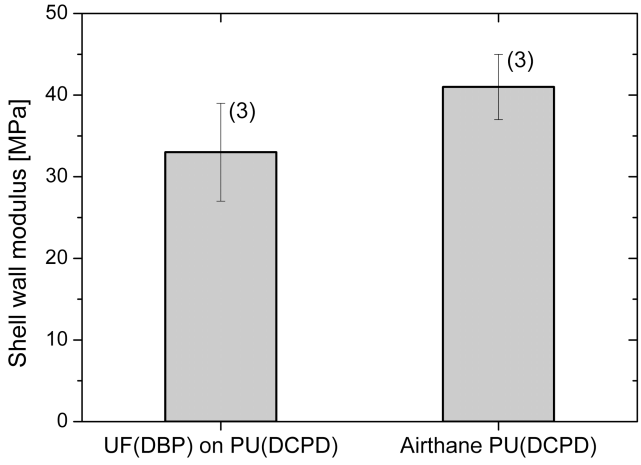

Figure 5.10: Modulus values determined for UF(DBP) peripherally decorated PU(DCPD) microcapsules in comparisson to surfactant stabilised PU(DCPD) microcapsules

5.5 Conclusions

A unique fabrication method to create binary microcapsules containing two distinct liquid components *via* small scale liquid filled microcapsules as Pickering stabilisers in combination with interfacial polymerisation was demonstrated. The capsule morphology, confirmed by fluorescent optical microscopy and SEM, showed that the small DBP filled UF microcapsules form a layer around the main liquid core and are polymerised into the shell wall during encapsulation. The presence of both of the encapsulated phases within a single capsule structure was confirmed by DSC experiments, and analysis indicated a DBP volume fraction

of 8.8%. This value is in good agreement with a calculated theoretical fraction on the basis of the observed architecture and dimensions. The capsule mechanical properties, probed by single capsule compression tests, revealed a high compliance and ductile deformation behaviour for the shell wall material. The behaviour was independent of introduction of peripherally incorporated microcapsules. An analogue result was found for the microcapsule modulus. The modulus was found to be comparable to values provided for the pre-polymer by its manufacturer with which the capsules were synthesised.

Having demonstrated the ability to construct binary capsules containing two isolated liquid phases, it is noted that the resulting ratio of the liquid phases is a function of the synthesis conditions and depends on both microcapsule dimensions. The liquid stoichiometry can be tailored by adjusting the Pickering particle concentration and/or the applied shear stress during emulsification. Binary capsule structures not only provide a novel storage and delivery platform for self-healing materials, but their unique architecture may find use in diverse applications such as therapeutic pharmaceuticals or security devices where a chemical reaction is desired after microcapsule rupture or degradation.

CHAPTER 6

A numerical study into the effect of capsule geometry on the healing efficiency

> There is geometry in the humming of the strings,
> there is music in the spacing of the spheres.
>
> *Pythagoras of Samos*

6.1 Introduction

Liquid-based self-healing material systems rely on the safe storage of latent healing-agents and their adequate release upon occurrence of damage. Dry was one of the first to described a self-healing material system based on resin filled hollow glass fibres with high aspect ratio.[11,12] Such systems are in principle capable of healing large scale and extended damage throughout the material due to their high fracture probability, but display disadvantages in practice. Long and continuous containers that run throughout large volume of material suffer from the risk of bleeding, *i.e.* excessive release of healing agent, and clotting along the fibre length upon triggered hardening mechanisms of the healing agents. Such unwanted bleeding and clotting processes would prevent healing upon formation of new cracks, either due to insufficient resources of healing agent or restricted transport. Additionally, preparation and handling of micrometer sized filled glass capillaries is delicate and labour intensive.

[0]Based on: S.D. Mookhoek, H.R. Fischer and S. van der Zwaag, *Comput. Mater. Sci.*, **2009**, 47(2), 506-511

Bond *et al.*[15,16] extended the work of Dry successfully to the domain of fibre composites and have shown that partly substitution of the composite fibres by resin filled tubes provides the material with a useful and relevant self-healing functionality.

Partly to remedy the disadvantages related to bleeding, clotting and preparation, a highly compartmentalized system using spherical microcapsules was engineered.[18] However, for such compartementalized systems merely spherical shaped microcapsules were investigated. The spherical geometry of the microcapsules is a direct result of their production method, mostly obtained via an *in-situ* polymerisation of an oil-in-water emulsion. It is their relative high volume to surface ratio however that leads to a small fracture probability with respect to their loading fraction and thus a modest release of healing agent into the crack area, in comparison to other capsule geometries. Hence other capsular geometries are to be considered that lead to more release of healing-agent at lower fractions of microcapsules in material formulations.

In order to obtain a relative high fracture probability of the dispersed particles and to enhance the volume of released healing-agent, the introduction of container anisotropy (cylinders, ellipsoids) is suggested. This chapter presents a numerical study into the effect of aspect ratio, volume fraction and orientation of elongated capsules on the healing efficiency of liquid healing agent based systems. The results of the geometrical model support and serve to guide the further development of elongated liquid filled capsules.[110,111] Furthermore the model will give additional insight into the key damage dimensions from a potential healing perspective.

6.2 Experimental

6.2.1 Selection and definition of model parameters

The model is based on a representative volume element (RVE) in which either spherical or elongated capsules are uniformly dispersed, such that the capsules do not overlap nor are in direct contact with each other. (Figure 6.1a and 6.1b respectively). A cubic RVE with edge-length α is defined using periodic boundary conditions. To obtain an RVE with a desired capsule volume, capsules are sequentially positioned in this RVE using a random number generator for the position of centre of gravity of each capsule on a 1000^3 lattice. For each newly positioned capsule, it is verified that the capsule does not overlap or touch with any of the already positioned capsules. In case of overlap the attempt to position a new capsule is cancelled and a new attempt for another position is made. In the case of the elongated capsules, changing the orientation vector of the cylinder axis in order to avoid inter-particle contact is explored prior to rejecting the attempt to position this new particle. For all simulations the thickness of the capsule wall is ignored and the volume of the healing agent to be released by a capsule is therefore equal to the capsule volume.

In order to calculate the amount of healing agent released at a particular planar crack, a test plane is defined at a random position but parallel to one of the faces of the RVE axes. The total released volume normalised to the crack area is calculated by taking the product of the number of capsules bisected and the the single capsular volume. For each condition, defined by the volume fraction of capsules, the individual capsule volume, geometry and the capsule orientation in the case of elongated capsules, 1000 simulations were performed and the results were averaged. In this work only mono-disperse capsule distributions were considered.

6.2.2 Spherical capsules

The applied spherical capsules in our calculations are represented by solid bodied spheres. The volume of a single spherical microcapsule within our model is mathematically defined as a classical sphere:

$$V_{caps}^{sph} = \frac{1}{6}\pi d^3 \tag{6.1}$$

for which d is the capsular diameter, neglecting the capsule shell wall thickness. The peripherally boundary of the capsule was defined at distance $r = \frac{d}{2}$ from the positioned center of body of mass using a spherical coordinate system.

6.2.3 Cylindrical capsules

The cylindrical capsules are formulated as solid bodied geometric cylinders with semi-spherical ends. This particular shape was selected as it approaches the geometry observed from experimentally produced stretched droplets and produced microcapsules.[110] The cylindrical

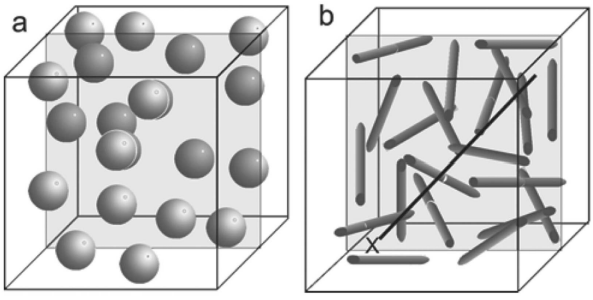

Figure 6.1: Schematic of a) spherical and b) cylindrical capsules being intersected within a volume element

capsule, which is a function of diameter d and aspect ratio AR (=L/d), is given as follows:

$$V_{caps}^{cyl} = \frac{1}{4}\pi \left(AR - \frac{1}{3}\right) d^3 \tag{6.2}$$

The volume of the solid bodied cylinder was then approximated using a series of overlapping spheres which number depends on the applied aspect ratio to preserve accuracy. After selecting $2AR - 1$ equally spaced points on the cylinder axis according to the directional parameter (representing the center bodies of mass for each virtual sphere), the boundary of the capsule was defined at distance $r = \frac{d}{2}$ from those points using a spherical coordinate system. A 2D schematic of the cylindrical representation is given Figure 6.2, displaying the $2AR - 1$ spheres to approximate the cylindric body.

The matrix/capsule system can be adjusted by varying the diameter d, volume concentration ϕ and AR, creating a composite material with varying capsule size, capsule loading and capsule shape. For our simulations we have selected six values for d over two decades, three volume concentrations and four different aspect ratios. Furthermore we also investigated three orientational orders for the cylindrical capsule system.

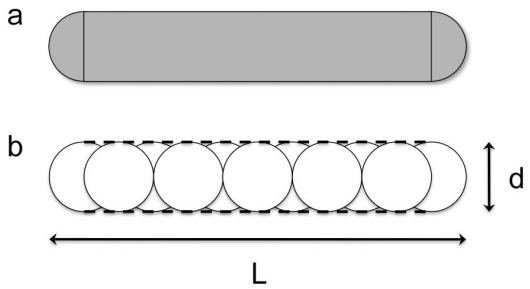

Figure 6.2: a 2D schematic of the cylindrical elongated capsule geometry applied in this model (a) and its representation by $2AR - 1$ overlapping spheres (b)

6.3 Results & Discussion

6.3.1 Spherical capsules

The calculated volume release per crack area for the case of spherical capsules is shown Figure 6.3a. The figure shows a monomodal but slightly skewed volume release distribution towards higher values. In the case of spherical capsules with capsular volume of 15.7 μm^3 (*i.e.* a capsule diameter = 3.11 μm) and volume fraction 0.10 an average volume per area is found of 0.317 μm with a calculated polydispersity index of 1.09. The volume released would

be capable of filling a crack volume with a uniform crack opening distance of maximum 0.317 μm.

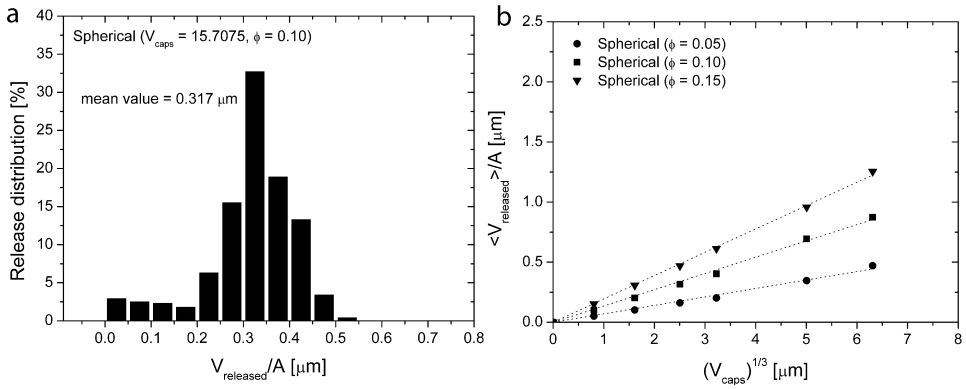

Figure 6.3: calculated average release of spherical microcapsules as function of capsule volume and its distribution for $V_{caps} = 15.705$

Figure 6.3b shows the calculated average volume per area as a function of the capsule size for three volume fractions. The observed linear dependence between average volume released per crack area and the size of a capsule for a given volume fraction, ϕ, is given by equation 6.3, which was derived before in Chapter 4:

$$\frac{V_{released}}{A} = nV_{caps} = \phi dA \tag{6.3}$$

The results presented clearly show the effect of microcapsule dimension on the amount of healing agent released. The total amount of liquid released decreases rapidly with decreasing microcapsule size. Figure 6.3b and eq. 6.3 indicate that small, *e.g.* nanosized, spherical microcapsules should only be employed for healing of damage at a very small scale (such as interfacial debonding[112]) and that a small capsule size does not enhance the healing efficiency in general.

6.3.2 Cylindrical capsules

The model predictions for the liquid release of randomly orientated cylindrical microcapsules of representative aspect ratio AR = 5, capsule volume of 15.7 μm^3 and volume fraction 0.10 are displayed in Figure 6.4a. The distribution here is also found to be monomodal and is shifted to larger volumes with respect to the simulations for the spherical capsules. The polydispersity remains at 1.09. The average volume released per area has increased from 0.317 μm for the spherical case to 0.448 μm, capable of filling a larger crack volume, referring

to a larger width.

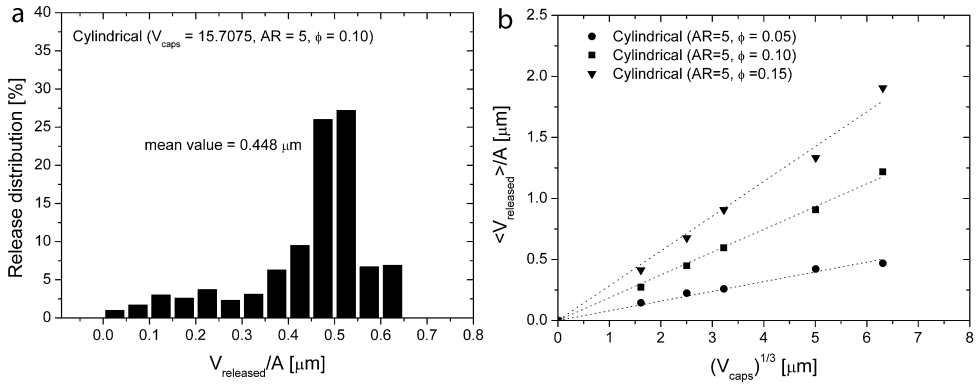

Figure 6.4: calculated average release of cylindrical microcapsules as function of capsule volume and its distribution for $V_{caps} = 15.705$

Figure 6.4b shows the average volume released per area as a function of the (capsule volume)$^{1/3}$ for three volume concentration and a fixed aspect ratio (AR = 5). Similar to the case of spherical capsules (Figure 6.3b) linear dependences are obtained, but the observed slope of the dependences has increased significantly, *i.e.* for a given capsule volume and a given capsule volume fraction a larger amount of healing agent can be delivered to a crack surface indeed.

Table 6.1: Fitted values for the curve slopes in Figure 6.3b (spheres), 6.4b (AR = 5) and the slopes for other investigated aspect ratios; AR = 3, 5, 7 and 10

ϕ [-]	k_{sph} [-]	k_{cyl} AR=3 [-]	k_{cyl} AR=5 [-]	k_{cyl} AR=7 [-]	k_{cyl} AR=10 [-]
0.05	0.066	0.072	0.084	0.108	0.133
0.10	0.133	0.143	0.181	0.213	0.255
0.15	0.190	0.213	0.274	0.312	0.355

6.3.2.1 Effect of capsule aspect ratio

The effect of the capsule aspect ratio on the release characteristics has been examined for different values of AR, namely AR = 3, 5, 7 and 10. This range of values for AR is considered relevant and viable for the elongated capsules when being manufactured *via* routes such as presented by Bon *et al.*[110] For all aspect ratios an approximately linear dependence between the released volume per area and the (capsule volume)$^{1/3}$ was obtained. The slopes of these linear relations are listed in Table 6.1.

The data in Table 6.1 show that the average amount of volume released for elongated particles increases with respect to that for spherical particles. The quotient of the determined slopes for elongated and spherical particles at a fixed capsule volume fraction (k_{cyl}/k_{sph}) is defined as the *release improvement factor*, RIF. The RIF will be used to evaluate the potential of elongated microcapsules. For randomly positioned cylindrical microcapsules the RIF is a function of the capsule aspect ratio only and appears independent of the volume fraction and the capsule volume.

The RIF as a function of the AR is given in Figure 6.5 and shows a significant increase for aspect ratios > 3, reaching an RIF of 1.9 at an aspect ratio of 10 for a system containing randomly dispersed cylindrical microcapsules.

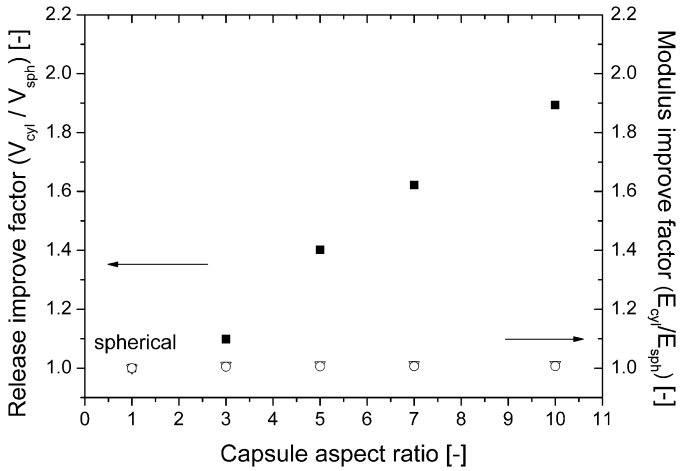

Figure 6.5: release improve factor (RIF: ■) and the modulus improve factor (MIF: 0.075 ○, 0.15 ▼) as function of the capsule aspect ratio (AR). For definition of the MIF see section 3.2.3. The released volume and modulus are normalised to the release and composite modulus for spherical capsules: AR = 1.

The significant increase in RIF with increasing aspect ratio can be converted in a desirable reduction in required volume fraction of capsules to obtain an equal released volume per

crack area, *i.e* a similar specific healing potential. Such a decrease in volume concentration lowers the effect of the liquid inclusions on intrinsic material properties, such as Young's modulus and density. This effect is illustrated in Figure 6.6 for different aspect ratios.

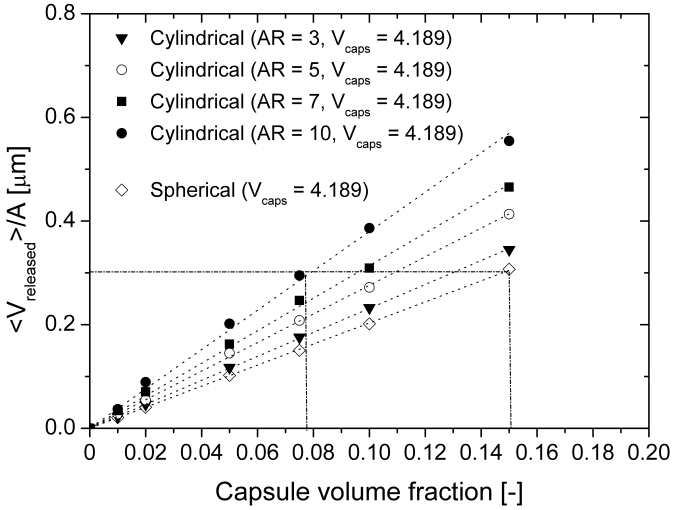

Figure 6.6: calculated average released volume as function of the capsule concentration for different values of AR. The horizontal and vertical crossing lines indicate the magnitude of the effect when changing from classical spheres to anisotropic capsules.

6.3.3 Experimental validation of the model for randomly dispersed particles

The predicted improvement factor for randomly dispersed cylindrical in comparison to spherical bodies was experimentally confirmed from fracture surface studies of particulate composites containing spherical polymer particles and chopped glass fibres with an aspect ratio of 10. In the experiment, polymethylmethacrylate (PMMA) solid bodies spheres and short, high aspect ratio, glass fibres of similar volume were dispersed in epoxy resin at equal volume concentration (10 vol%). Both filler type composites were molded into a cylindrical sample and subsequently cryogenically fractured after submerging them in liquid N_2. The surfaces were examined by scanning electron microscopy (SEM) at equal factors of magnification.

From the SEM images the number of intersected particles for a fixed surface area was derived by summation of the number of spheres and fibres sticking out of that surface and the number of holes caused by particle pull-out. The ratio between the amount counted for the glass fibre composite and the spherical particle composite was taken as the experimental value for the RIF. In Figure 6.7 two images are shown, showing a fracture surface of dispersed

PMMA spheres (a) and a fracture surface of dispersed glass fibres with AR =10 (b) in epoxy resin. The images clearly show the larger number of cylindrical bodies that was exposed by the crack. The ratio found here between the number of intersected cylindrical and spherical particles is 1.9, which agrees very well with the outcome of our calculations.

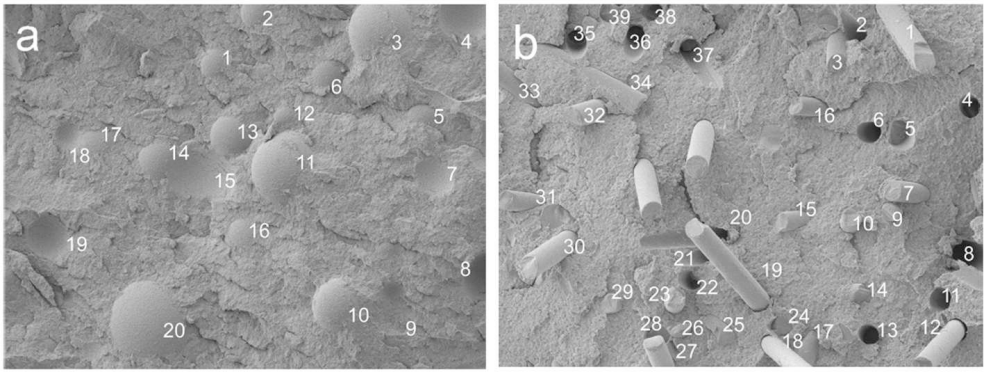

Figure 6.7: Scanning electron microscopy (SEM) images of the a) spherical and b) cylindrical particulate composite fracture surfaces. Both images show a 600 by 450 μm area of the fracture surface, indicating the identified number of intersected particles for each geometry

6.3.3.1 Effect of capsule orientation

In the case of elongated particles also the spatial orientation of the cylindrically shaped capsules inside the material is a system parameter which can influence the release of healing agent volume per crack area. The orientational order parameter for dispersed cylindrical rod-like structures can be given by the second order Legendre polynomial:[113]

$$\langle P_2 \rangle = \frac{\langle 3cos^2\theta \rangle - 1}{2} \tag{6.4}$$

in which θ is the angle between the cylinder axis and the normal axis (X), perpendicular to the fracture orientation, as shown in Figure 6.1. Now by varying the orientation of the elongated capsules in the RVE from $\langle P_2 \rangle$ = -0.5 (parallel to fracture plane) to 0 (random) and 1 (perpendicular to fracture plane) the effect of capsule orientational order on released volume per area can be determined. The results of these calculations are presented in Figure 6.8. The figure shows the release improve factor (RIF) as function of the orientational order parameter for cylindrical capsules with AR = 3, 5, 7 and 10.

The curves show a large dependency of the RIF on capsule orientation. For all aspect ratios the RIF at $\langle P_2 \rangle = 1$ (full alignment perpendicular to the fracture surface), is higher

than that for the randomly orientated structures ($\langle P_2 \rangle = 0$) due to the increase in fracture probability. The degree of increase depends only on the capsule AR. Non-surprisingly, it is also observed that the RIF for cylinder alignment parallel to the fracture plane, $\langle P_2 \rangle$ = -0.5), results a lower value than obtained for the spherical system. For a given particle volume the diameter of the cylinder decreases with increasing AR, leading to lower fracture probability and values for RIF at $\langle P_2 \rangle$ = -0.5.

The positive effect of preferred orientation of the cylinders perpendicular to the fracture plane again offers the possibility to lower the capsule loading when specific potential healing efficiencies are required. To illustrate the magnitude of the effect caused by the orientational order in combination with the aspect ratio, the average released volume as function of the capsule concentration is plotted in Figure 6.9 for the different values for cylinders with AR = 5 and AR = 10.

Now having all capsule variables explored and illustrated quantitatively, the release volume equation for spherical capsules given in eq. 6.3 can be rewritten for anisotropic cylindrical capsules:

$$\frac{V_{released}}{A} = \epsilon \left(V_{caps}\right)^{\frac{1}{3}} \phi \cdot f\left(AR, \langle P_2 \rangle\right) \tag{6.5}$$

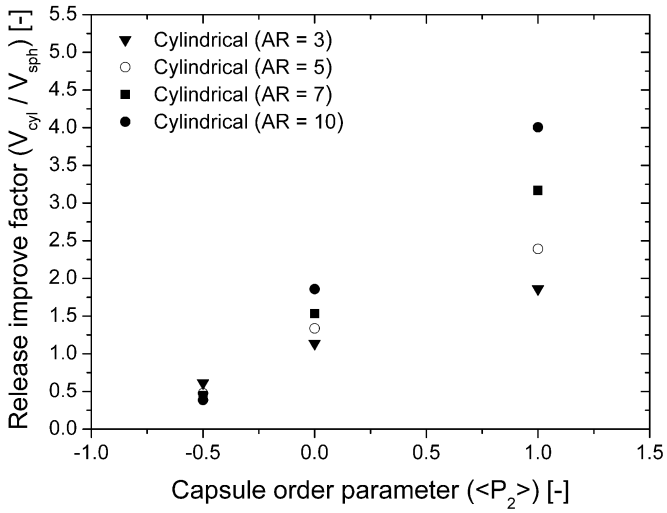

Figure 6.8: release improve factor (RIF) as function of capsule orentaional parameter ($\langle P_2 \rangle$). The released volume is normalised to the release for spherical capsules. $\langle P_2 \rangle$: -0.5 (orientation parallel to fracture plane), 0 (orientation random) and 1 (orientation perpendicular to fracture plane).

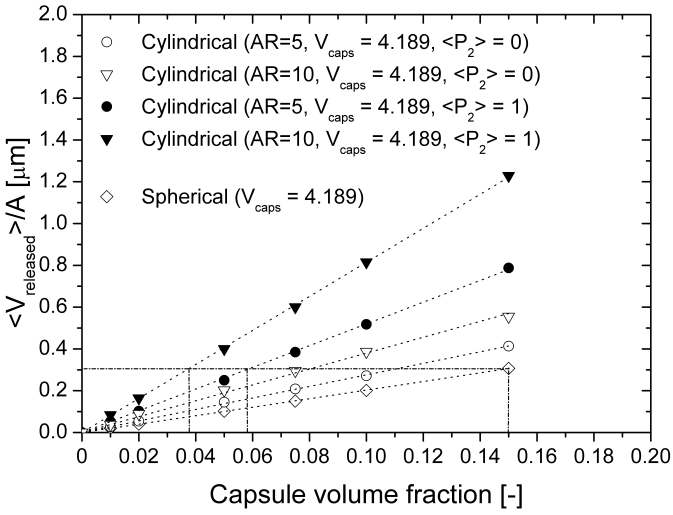

Figure 6.9: calculated average released volume as function of the capsule concentration for two different values of AR and for two different orienational parameters ($\langle P_2 \rangle$). The horizontal and vertical crossing lines indicate the magnitude of the effect when changing from classical spheres to orientated anisotropic capsules.

in which ϵ is a geometrical constant which is equal to $\left(\frac{6}{\pi}\right)^{\frac{1}{3}}$ (≈ 1.24) and $f\left(AR, \langle P_2 \rangle\right)$ is a function that describes the dependency on the aspect ratio and Legendre orientational parameter. Based on the results of the simulations presented for $1 <$ AR < 10 and -0.5 $< \langle P_2 \rangle < 1$ the following approximate function f, which is correct to within 5% for the domain specified, is proposed:

$$f\left(AR, \langle P_2 \rangle\right) = pAR + (qAR)\left(\langle P_2 \rangle + 1\right)^{\frac{1}{2}} + v \tag{6.6}$$

for which the values for the three independent constants are found to converge to p: -0.424, q: 0.530 and v: 0.809, to obtain an optimal fit to the data.

For the specific case $\langle P_2 \rangle = 1$ an analytical solution for the released volmue per crack area can be derived. In this case all cylindrical microcapsules are aligned and are orientated parallel to the normal of the fracture plane. Hence, only a small adaption to eq. 4.1 is required to describe the probability of a crack hitting a perpendicularly aligned cylindrical capsule:

$$\Psi = \frac{LA}{V_{RVE}} = \frac{d_{cyl}\left(AR\right)A}{V_{RVE}} \tag{6.7}$$

in which L now is the length of the capsule's long axis and d_{cyl} the width of the cylinder.

Following the similar deduction in eqs. 4.2-6.3, and the definition of the cylinder volume (eq. 6.2), it follows that the released volume per crack area for cylindrical capsules with $\langle P_2 \rangle = 1$ equals:

$$\frac{V_{released}}{A} = 4^{\frac{1}{3}} \left(V_{caps}\right)^{\frac{1}{3}} \left[\pi \left(AR - \tfrac{1}{3}\right)\right]^{-\frac{1}{3}} \phi AR \tag{6.8}$$

This exact expression allows us to validate the data found through our model for $\langle P_2 \rangle$ values of 1. To demonstrate this, the volume release per area for a given capsule volume (4.189 μm^3), capsule volume fraction (0.15) and AR (10) is calculated through eq. 6.8. Filling in the given parameters into the equation results a $V_{released}/A$ of 1.24, which accords with the value found through the model that is shown in Figure 6.9.

6.3.3.2 The effect of elongated capsules on the composite modulus

Incorporation of relatively high fractions of liquid filled structures inside a material matrix decreases the modulus significantly.[114] Changing the capsule geometry from spherical to anisotropic may also have an effect on the composite properties. The influence of elongated inclusions on the elastic modulus of a composite material can be described by the Halpin-Tsai model.[115,116] Using the factors for particle shape and orientation introduced by Van Es *et al*[117] the Halpin-Tsai model yields:

$$E_c = \zeta E_m \frac{\left(\phi_f + 1/\zeta\right) E_f + \left(1 - \phi_f\right) E_m}{\left(1 - \phi_f\right) E_f + \left(\phi_f + \zeta\right) E_m} \tag{6.9}$$

in which E_c is the composite Young's modulus; E_f the filler modulus; E_m the matrix modulus; ζ the shape factor - depending on geometry, aspect ratio and orientation; ϕ the filler volume fraction. For cylindrically shaped particles the shape factor, ζ, equals to 2AR in the direction of the cylinder axis and has a value of 2 in the cylinder radial direction. Van Es calculated that the average composite modulus for random orientated particles in 3D is given by:[117]

$$E_c^{3D-random} = 0.184 E_c^{//} + 0.816 E_c^{\perp} \tag{6.10}$$

In our case the thickness and modulus of the capsule shell material can be neglected as the thickness is much smaller than the capsule diameter and its modulus in most cases is comparable to the matrix material.[102] The tensile modulus of the liquid itself is assumed zero. With these assumptions eq. 6.9 can be rewritten:

$$E_c = \zeta E_m \frac{\left(1 - \phi_f\right)}{\left(\phi_f + \zeta\right)} \tag{6.11}$$

From the model (combining eqs. 6.10 and 6.11 the influence of a 3D random distribution of liquid-filled capsules (geometry and volume fraction) on the composite properties can be calculated. By introduction of anisotropic microcapsules in stead of spherical ones, (ζ) and $E_c^{//}$ are changed positively and a smaller influence on the matrix intrinsic properties is expected.

The modulus improve factor (MIF) is defined as the quotient of the calculated 3D random modulus using anisotropic particles and the 3D random modulus when applying spherical inclusions (E_{cyl}/E_{sph}). The definition makes the MIF independent of material properties. The MIF as function of aspect ratio is also given in Figure 6.5 for two concentrations (0.075 and 0.10) in comparison to the RIF at similar scales. In contradiction to the RIF the MIF (at different concentration levels) only shows very low values above unity and almost no dependence of AR due to the fact that $E_f \ll E_m$ and the capsules are randomly orientated. In addition, full alignment of the elongated capsules, $\zeta = 2AR$, does also not have a significant effect. Hence, increasing the capsule aspect ratio will only directly influence the liquid release characteristics and not the composite material properties. Indirectly, a potential decrease of the capsule volume fraction as a result of capsule anisotropy leads to an increase of the composite modulus.

6.3.4 Consequences for crack dimensions to be healed

As pointed out before, the released volume per crack area reflects the liquid column height that becomes available to fill the crack. Now, when crudely assuming a parallel crack separation the crack size (width) that can be fully filled by the released healing agent is given by the following equation:

$$PCOD \leq \frac{V_{released}}{A} \tag{6.12}$$

in which PCOD is defined as the parallel crack opening distance. This equation indicates that as long as PCOD is less than $V_{released}/A$ maximal achievable healing is obtained for a simplified crack. As demonstrated, this critical PCOD for complete healing scales (linearly) with the $(V)^{\frac{1}{3}}, \phi, AR$ and $\langle P_2 \rangle$ depending on geometry of the microcapsules. When the PCOD exceeds the value of the average released volume per surface area, the parallel crack is no longer filled completely. With a decreasing fraction of the crack being filled, the healing degree decreases accordingly. Some foreseen trends of the curve at which the healing degree is decreased, are given in Figure 6.10 and will be determined by the morphology of the bridging liquid between the crack-faces.[118] The actual dependence of the healing degree as function of the crack opening distance depends on many parameters, such as crack geometry, surface roughness and healing-agent wetting behavior. Hence, the dependence cannot be expressed by a simple mathematical model. However, the plots given are indicative for the

expected dependence.

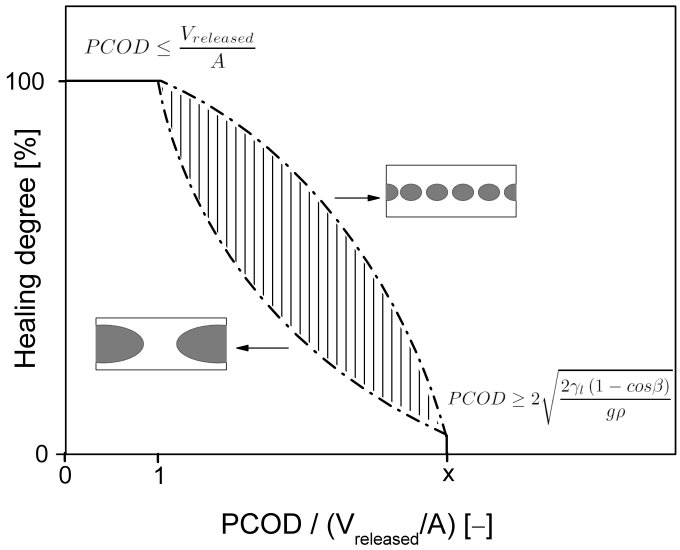

Figure 6.10: An indicative plot for the material Healing Degree dependence on the dimensionless parallel crack opening distance.

The indicative plots shows that at high values of PCOD the distance between the two crack faces is too large to be bridged by the liquid present on both surfaces and the healing degree is zero. If the two crack faces are spaced more closely the liquid on both surfaces can come in contact with both faces locally and healing can be expected.

The critical value of the crack opening distance (for a parallel crack) at which some form of inter-crack surface bridging and hence healing can be expected ($PCOD/\,(V_{released}/A) = x$), is given by the De Gennes' equation for the maximal thickness of a droplet on a surface:[119]

$$PCOD^x = 2\sqrt{\frac{2\gamma_l\,(1-cos\beta)}{g\rho}} \tag{6.13}$$

in which γ_l is the liquid surface tension, β the liquid-solid contact angle, g the gravitational constant and ρ the liquid density. This equation indicates that the critical (horizontal) crack opening that can be healed to some degree is determined by material properties only: γ_l, β and ρ. Thus, for example when selecting dicyclopentadiene as healing agent for an epoxy-resin type of material[18] (γ_l= 0.036 J/m^2, ρ = 987 kg/m^3, β= 4.5^o) a critical PCOD of 340 μm can be found. In contrast to the defined PCOD that can still be fully healed, the maximal PCOD amenable to self-healing is only a function of the liquid/matrix system and

not of the applied capsules (size, fraction and geometry). When the PCOD is reduced below the critical value, the liquid spreads over the fracture surfaces and the remaining flaw size of the crack reduces proportionally.

The analysis just presented leads to an interesting result in the sense that in contrast to classical fracture theory,[120] it is not the length of the crack which is relevant for the recovered fracture strength, but the parallel crack opening distance. Experiments to demonstrate this relation are not presented here, but the model given allows designing and performing the appropriate experiments in future work.

6.4 Conclusions

A simple geometrical model based on a cubic representative volume element filled with discrete liquid healing agent filled capsules is used to quantitatively predict the amount of healing agent released as a function of the capsule dimensions, volume fraction, aspect ratio. In the case of elongated capsules also the influence of capsule orientation is investigated. From the results it is observed that a strong improvement in the healing potential is predicted for elongated capsules in comparison to spherical capsules. The full alignment of such elongated microcapsules perpendicular to the crack plane also has a significant positive effect upon the healing potential. Such a predicted increase in healing efficiency allows a reduction of the capsule volume fraction to obtain equal volume release per area and therefore maintaining more intrinsic material properties.

The influence on composite modulus by introduction of high aspect ratio microcapsules appears to be negligible as difference in liquid and matrix modulus outweighs the effect.

In contrast to the results for the classical fracture theory for isotropic materials, for liquid based self-healing material systems the potential healing efficiency is a function of the average crack opening distance rather than the crack length.

CHAPTER 7

Routes to preparation of elongated microcapsules

Curiosity often leads to trouble

From Alice in Wonderland by Lewis Caroll

7.1 Introduction

The introduction of liquid-filled containers inside structural materials in order to provide them with a self-healing functionality, compromises other desirable intrinsic material properties, such as strength, stiffness, ductility and density. For existing liquid-based self-healing systems, a spherical capsule volume fraction up to 20% can be necessary to achieve a desirable healing performance. Such a large amount of non-structural material is acceptable to deliver a proof of concept in a laboratory environment. However, this amount of non-structural components in the material is far too high for real applications because of its large negative contribution to the overall properties. In order to maximise the healing agent volume release versus the capsule concentration of the liquid-based self-healing materials, elongated capsule geometries have been considered and different production routes to anisotropic microcapsules have been investigated. The previous chapter demonstrated theoretically that the amount of liquid released per crack area from a liquid-capsule equipped self-healing material is enhanced by changing the capsule geometry from spherical to ellipsoidal/cylindrical.

[0]Partly based on: S.A.F. Bon, S.D. Mookhoek, P.J. Colver, H.R. Fischer and S. van der Zwaag, *Eur. Polym. J*, 2007, 43(11), 4839-4842

The release improvement factor is found to be substantial even for a moderate anisotropy, *e.g* an aspect ratio 5.

Although abundant literature is available for the encapsulation of liquids in spherical capsules, using different processes,[84,121,122] materials[83,123] and architectures,[124,125] methods to obtain microcapsules with an aspect ratio exceeding values of 1 have rarely been documented. Since the production of liquid filled microcapsules most frequently proceeds through a stage of droplets dispersed in a stable manner in an immiscible second liquid, the classic spherical shape is the direct result of the minimisation of the surface energy of the two non-compatible fluids. Reported strategies to create elongated particles involve routes *via* solid bodied high aspect ratio templates that are encapsulated first, whereafter the core is removed.[126] After removal of the core material a hollow vesicle is created and subsequently other steps have to be employed to fill the capsule with the desired liquid and adequately close the capsule. These multi-step syntheses are however considered unpractical for our purposes since generally the capsular shell materials, *e.g.* polyelectrolyte multilayers, are relatively permeable and lack sufficient strength to maintain the elongated just created, especially upon removal from the suspending liquid.[127]

Using stable anisotropic droplets rather than solid bodied templates gives the opportunity to use common encapsulation techniques that are able to construct a robust shell wall material, *e.g*, interfacial polycondensation, in-situ polymerisation, precipitation polymerisation, etc. These type of polymer shell materials have adequate mechanical properties and are able to maintain the anisotropic shape upon drying of the capsules. Various techniques have been described in literature to produce such stable non-spherical droplets.[128–131] In these procedures initial spherical suspended droplets are deformed by either continuously stressing or confining the droplets, this to prevent the relaxation of the induced anisotropic shape back to the spherical shape by surface tension effects. When a suitable encapsulation step is introduced at such a deformed stage of the droplets, it fixes the elongated geometry and the desired shaped microcapsules are created.

In this chapter routes to produce elongated microcapsules through stable deformation of droplets are evaluated and two novel procedures are presented that allow the creation of elongated capsules.

7.2 Deformation of emulsion droplets in shear flow

7.2.1 Background

The deformation of droplets into elongated ellipsoids by an induced flow field is a key stage in the dispersive mixing of two immiscible liquids and has been well studied.[132] The imposed shear causes an increase in the interfacial area between the two components. It results in a decrease in the local dimensions perpendicular to the flow direction which is accompanied

by an increase in length over the parallel axis, as the volume is kept constant.

When buoyancy effects of the droplet can be neglected (assuming comparable densities of the two liquids), the drop's deformation is mainly governed by an equilibrium denoted as the capillary number, Ca, which is the ratio of the present shear stress, τ, exerted on the drop by the flow field and the interfacial stress σ/R (with σ the interfacial tension and R the local droplet radius):

$$Ca = \frac{\tau R}{\sigma} = \frac{\eta_s \dot{\gamma} R}{\sigma} \tag{7.1}$$

where η_s is the viscosity of the suspension liquid and $\dot{\gamma}$ the shear rate. When the capillary number increases and exceeds a critical value, Ca_{crit} the shear forces overrule the interfacial stress and the drop will break into fragments and form smaller drops. The critical capillary number is a function of the viscosity ratio between the dispersed and the suspending medium respectively and was studied in great detail by Grace.[133] His work resulted in the later called Grace curves that lead to a phase diagram for droplet deformation, predicting stable and unstable regimes for droplet stretching. The classical Grace plot is reproduced in Figure 7.1. The domain above each of the curves is the unstable region leading to droplet break-up.

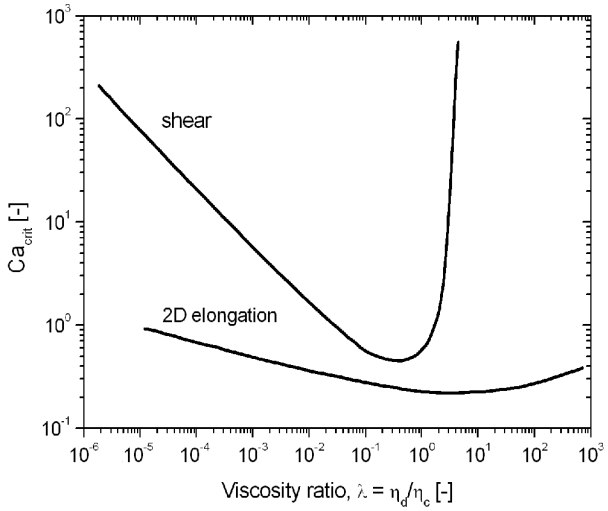

Figure 7.1: The classical Grace curve illustrates the viscosity dependence of the critical capillary number for plain shear and elongational flow; reproduced after Grace (1971)[133]

If the capillary number is relatively small, the interfacial stress exceeds the shear stress and the droplet withstands the external forces and a steady deformed ellipsoidal drop exists.

The degree of anisotropy, S, of a droplet can be expressed as follows:

$$S = \frac{L - D}{L + D} = \frac{AR - 1}{AR + 1} \tag{7.2}$$

wherein, L is the length of the larger and D the length of the smaller axis of the droplet. The symbol AR (aspect ratio) represents the ratio of the two radii respectively. The S value for a spherical droplet is evidently zero.

The degree of anisotropy is a function of the capillary number and the viscosity ratio between the dispersed and suspending medium, λ, for which an approximate expression is given by the Taylor model:[134]

$$S = \frac{16 + 19\lambda}{16\,(\lambda + 1)} Ca \tag{7.3}$$

However, a more accurate expression was suggested by Torza *et al.* to describe the deformation behaviour at large suspension medium viscosities in combination with high rates of shear:[135]

$$S = \frac{16 + 19\lambda}{4\,(\lambda + 1)\sqrt{\left[(20/Ca)^2 + (19\lambda)^2\right]}} \tag{7.4}$$

This expression allows the prediction of the droplet elongation at a given input shear rate, initial droplet size and volume concentration for a known 'emulsion' system (liquid viscosities and interfacial tension). In Figure 7.2 the degree of anisotropy as a function of the viscosity ratio for different capillary numbers is plotted. The figure shows that substantial elongation is only obtainable at high Ca values ($Ca > 1$) and low viscosity ratios ($\lambda < 10^{-1}$).
From Figure 7.2 it can be observed that for relative high viscosity ratios, $\lambda \gg 1$ no significant anisotropy can be achieved, irrespective of the capillary number. Eq. 7.4 is then reduced to a simple linear relationship between the logarithmic anisotropy and the logarithmic viscosity ratio:

$$S = \frac{5}{4\lambda} \tag{7.5}$$

This linear dependence in indicated in Figure 7.2 with a dashed line.

For viscosity ratios much smaller than unity the relation between the degree of anisotropy and the viscosity ratio only appears to be a function of the capillary number. Hence, when selecting a viscosity ratio ≤ 1, a systematic alteration in the capillary number from 0.01 to 1 results different orders of elongation magnitude. However, when looking at the Grace curve (Figure 7.1) the viscosity ratios around unity only have low critical values for the capillary number and droplet break up in shear is expected at moderate capillary numbers. For that reason stable drop deformation, preventing break-up, should rather be carried out at $\lambda = 0.01$ than at $\lambda = 1$.

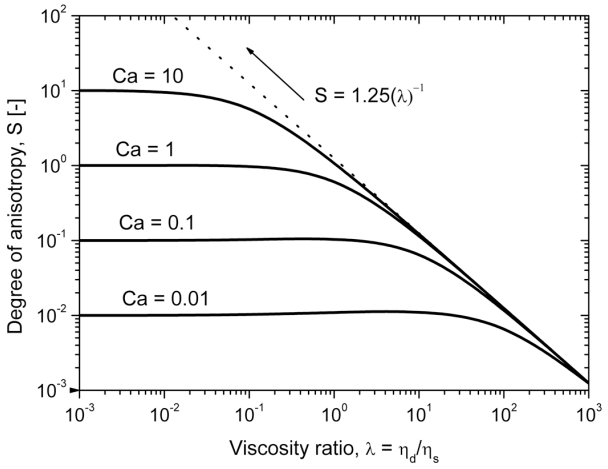

Figure 7.2: Droplet elongation as function of dispersed/continuous phase viscosity ratio for different capillary numbers

In experiments it is therefore advisable to modify a known emulsion system and increase the suspension medium's viscosity to lower the viscosity ratio. The capillary number can be changed either by increasing the shear rate input and or lowering the interfacial tension. Despite the fact that the interfacial tension may be influenced quite easily by the use of surfactants, the described theory does not include the addition of surfactant to the system. Since an unequal distribution of surfactant during the droplet's deformation and thus having a radius dependent surface tension, could result in two drops with identical λ and Ca values not deforming identically.

7.2.2 Experimental

7.2.2.1 Materials

Ethylene-*alt*-maleic anhydride copolymer (EMA, M_w 100-500 kDa) and adipoyl chloride (AC), were purchased from Sigma Aldrich, The Netherlands. Dicyclopentadiene (DCPD, 95% endo), polyvinylalcohol (PVA, M_w 88 kDa, 88% hydrolysed) and diethyltriamine (DETA) were obtained from Acros Organics, Belgium. All materials were used as received.

7.2.2.2 Encapsulation of deformed droplets in shear and elongational flow

For the production of anisotropic microcapsules in large quantities, a standard microencapsulation procedure was modified to create anisotropic droplets in suspension by deformation after the initial emulsification step of the phase to be encapsulated. In all experiments dicyl-

copentadiene was taken as the dispersed phase and typical concentrations of 20 vol% were used. The continuous phase was a 0.5 wt% EMA/H_2O solution. To alter the continuous medium's viscosity, the concentration of PVA in the water phase was varied. The concentrations at which the aqueous solutions were prepared are given in Table 7.1

Table 7.1: prepared PVA/EMA/H_2O solution viscosities at 25^oC

C_{PVA} $[wt\%]$	C_{EMA} $[wt\%]$	η_s $[Pa.s]^a$	λ $[-]^b$
0	0.50	0.005	0.640
4.0	0.50	0.059	0.054
5.0	0.50	0.105	0.030

[a] The viscosity of PVA/EMA solutions of up to 16 wt% at 25^oC is assumed Newtonian in behaviour.[136] [b] The viscosity of DCPD at 25^oC was measured to be 0.0032 $Pa.s$.

To encapsulate the DCPD the liquid was emulsified into the PVA/EMA/H_2O solution by means of a standard stirring blade, creating an average droplet size of ≈ 200 μm for the shear and ≈ 100 μm for the elongational flow experiments.[66] In this study a fast interfacial polymerisation between AC and DETA[137] was used to fix the anisotropic geometry and turn the droplets into microcapsules. In order to allow an interfacial polymerisation at a later stage small quantities of adipoyl chloride (0.12 - 0.40 g/ml) were added to the DCPD before it was added to the stirring aqueous solution.

The created emulsion was subsequently sheared using a custom made Couette set-up or by being pushed through a conical orifice followed by a narrow capillary at variable pressure. Both techniques are schematically shown in Figure 7.3. DETA (1.0 - 3.0 g) was only added after the droplet deformation, as the the AC + DETA reaction is very fast and produces a microcapsule shell almost instantaneously upon addition of DETA.

Batch encapsulation in Couette shear The deformation of dispersed emulsion droplets in the aqueous solutions with varying viscosity, was performed by Couette shear (Figure 7.3a). The set-up composes of a glass outer vessel ($\varnothing$ 88 mm) to hold the suspension and an aluminium inner cylinder ($\varnothing$ 40 mm) of which the cylinder is connected to a Dispermat CV (BYK-Gardner), able to shear the suspension by controlled rotation up to 20000 $revolutions/min$. Depending on the viscosity of the suspending medium, the amount of necessary shear varies significantly with the desired degree of anisotropy. This effect is illustrated in Figure 7.4 where the predicted degree of anisotropy is shown as function of the cylinder revolutions per minute for our emulsion composition and Couette set-up. The interfacial tension for different concentrations of the PVA/EMA/H_2O with DCPD was measured using the Du Noüy ring method on a Krüss K6 apparatus. In this method a platina ring is placed below the interface between the two liquid phases inside a small glass container. The

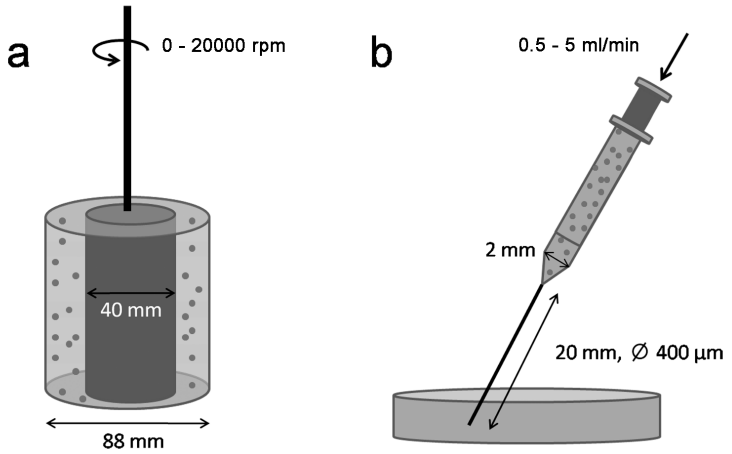

Figure 7.3: A schematic of both experimental set-ups used to create anisotropic emulsion droplets by deformation in flow: a) plain shear in a Couette, b) 2D elongational flow through a capillary

maximum force that is needed to pull the ring from below the interface through the interface is directly proportional to the interfacial tension. The interfacial tension for all the prepared solutions was found to be approximately 11 mJ/m^2. The viscosity of DCPD at 25^{o}C was measured to be 3.2 $mPa.s$.

From Figure 7.4 it can be observed that in the case of moderate suspension medium viscosities a large amount of shear is required to deform the dispersed emulsion droplets and only low degree of anisotropy can be obtained.

In a typical experiment the DCPD emulsion was poured into the Couette set-up and was sheared using a pre-defined shear-rate for 5 min to allow a steady droplet deformation. Then, H_2O diluted DETA (1:5 wt/wt) was added to start the interfacial polymerisation and encapsulate the dispersed phase. An excess of DETA was employed to capture the produced HCl during the reaction. After addition of the DETA the shearing was continued for another 5 min and the produced polymeric particles were filtered from the aqueous solution after dilution of the suspension medium with water. The filtrate was then washed extensively with a large excess of water and was allowed to dry in air.

Fixation of single deformed droplets in elongational flow Besides the deformation in Couette shear, a created emulsion of suspended $\approx$ 100 μm sized DCPD droplets was also deformed in the prepared PVA/water solutions by using 2D elongational flow at different rates ranging from 0.5 to 2.0 ml/min (Figure 7.3b). Elongational flow was realised by pushing the emulsified droplets through a conical orifice in a modified syringe followed by a straight cut, $\varnothing$ 400 μm, needle. The droplet suspension was injected under the surface of a solution of DETA/H_2O (1:5 wt/wt) to capture the elongated droplets into polymeric shells.

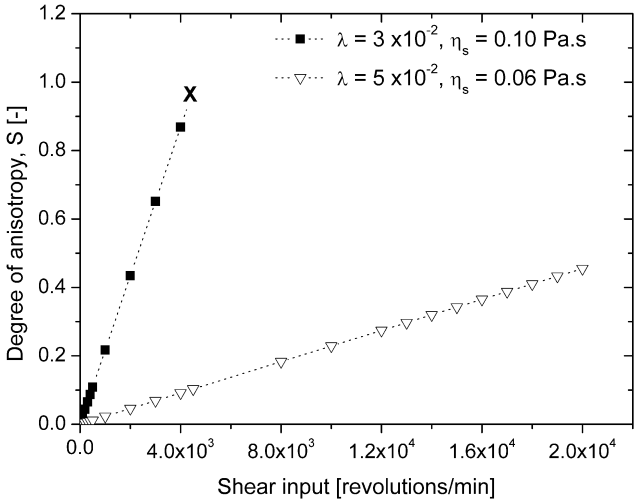

Figure 7.4: Necessary shear rate input for achieving the desired degree of anisotropy at different viscosity ratios, changing the suspending medium's viscosity. For $\lambda = 3 \cdot 10^{-2}$ X marks the limit of the input shear rate where $Ca = Ca_{crit}$ and droplet break-up occurs

Various shear and viscosity ratios, comparable to the Couette shear experiments, were used to prepare anisotropic droplets.

7.2.3 Results & Discussion

The emulsification of DCPD in the prepared PVA/EMA solutions resulted in relative good distribution of the organic phase; a droplet size of approximately 100 μm and 200 μm on average could be achieved for all three viscosity ratios investigated, with polydispersity indices typically between 1.71 ($\lambda = 0.030$) and 1.17 ($\lambda = 0.640$). The encapsulation of the droplets *via* the interfacial reaction between AC + DETA resulted in well defined microcapsules in suspension. The excess of DETA used to remove the reaction product HCl was found most effective compared to other methods that include the addition of alkaline salts, such as NaOH, $NaHCO_3$ or Na_2CO_3. The application of the latter alkaline compounds appear to result in strong hydrolysis of the AC upon addition or produce CO_2 gas, disturbing the two-phase emulsion system.[138] Although the AC can also react with the hydroxyl functionalities of the PVA to produce an interfacial film, no polymerisation product is observed and the dispersed DCPD is freely suspended in the typical time of experiments. Since the rate of this reaction is fairly low, the fast reaction between AC and DETA effectively only leads to the encapsulation of the dispersed liquid phase.

The washing step appeared to be crucial to obtain individual particles when filtering the

microcapsules from the suspending liquid. In the case of PVA being present in the suspending medium multiple washing steps with large amount of water were required to remove all PVA, which agglomerated the microcapsules upon drying. The remaining trace of DETA, that was applied to catch-off the HCl, was removed later by washing the capsules with a dilute HCl solution (0.5 M) resulting in light yellowish particles. Remaining DETA causes the microcapsules to turn yellowish brown and forms a gel-like cake as the capsules link due to unreacted AC and DETA in the presence of water.

Upon drying in air all microcapsules produced with AC + DETA however appeared unstable. The produced core-shell particles deformed slowly under the acting forces of gravity and collapsed in time when the DCPD evaporated. This observation was found independent of variance in AC and DETA concentration, from which it can be concluded that the formed polyamide shell wall is permeable for the volatile DCPD. For that reason observations on particle anisotropy were performed in suspension where the capsules are stable.

7.2.3.1 Encapsulation of deformed droplets in plain shear

The qualitative results for the encapsulation of elongated drops in plain shear experiments are shown in Table 7.2.

Table 7.2: Results of capsule anisotropy in a plain shear flow field

$\dot{\gamma}$ $[rev/min]$ λ $[-]$	0	1000	2000	3000	4000	4500
0.640	O	O	O	O	O	O
0.054	O	O	O	O	O	O
0.030	O	A	A	X	X	X

O: no capsule anisotropy observed. A: capsule anisotropy observed, X: droplet fragmentation and capsule rupture

For the viscosity ratios investigated only relative low degrees of anisotropy were observed at the lowest prepared value of λ and only at shear input values of 1000 and 2000 rev/min. Moreover, anisotropy was only observed for a small fraction of the capsules, as the majority of the capsules was still perfectly spherical. Representative images of the observed capsule anisotropy are given in Figure 7.5. The anisotropy obtained for the shear rate values of 1000 and 2000 rev/min more or less agree with what was expected from our predictions in Figure 7.4. At 1000 rev/min an average aspect ratio of 1.6 was measured, *i.e.* a degree of anisotropy, $S = 0.23$. For $\dot{\gamma} = 2000$ rev/min the aspect ratio increased to 2.2 ($S = 0.375$). Both values match the predicted values for the given viscosity ratio at the respective shear rate.

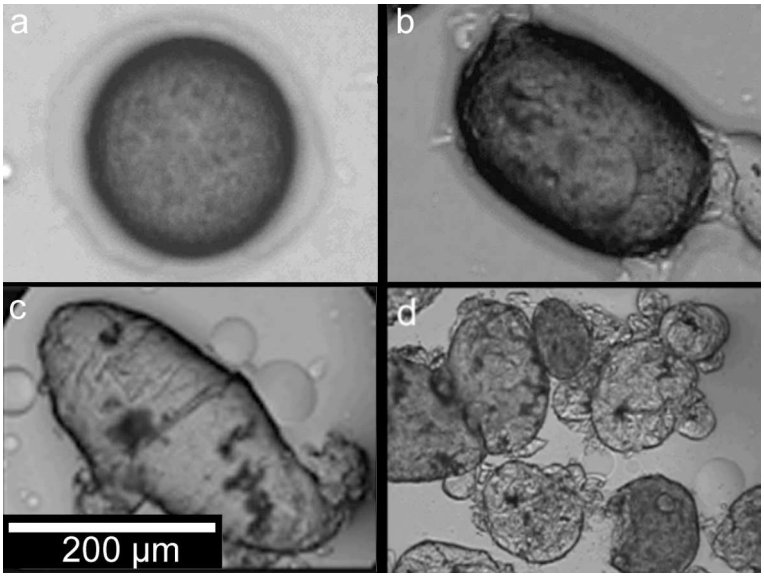

Figure 7.5: Evolution of capsule anisotropy with increasing shear rate for $\lambda = 0.030$. a) $\dot{\gamma} = 0\ rev/min$; AR = 1. b) $\dot{\gamma} = 1000\ rev/min$; AR = 1.54. c) $\dot{\gamma} = 2000\ rev/min$; AR = 2.24. d) $\dot{\gamma} = 3000\ rev/min$; capsules ruptured and are smaller than initial size.

The experiments did not result a high degree of anisotropy and uniformity, although for higher values of shear rate the applied values of Ca were theoretically ideal to obtain a significant degree of elongation. The most probable explanation for the observations is that vibrations of the Couette's inner cylinder in the higher shear region (3000 - 5000 rev/min) cause droplet break-up below the critical value of the capillary number, leading to smaller droplets and irregular shell morphologies, which subsequently are insensitive to deformation at the given shear. At high rotational speeds the average droplet diameter is indeed decreased and the distribution is shifted towards smaller droplet diameters. Additionally, when the capsules are formed by the addition of DETA, capsules rupture under the high shear. Hence, obtaining high quality capsules is difficult. The presence of relative large concentrations of viscosity modifier PVA may account for the somewhat lower obtained anisotropy for the microcapsules prepared at 1000 and 2000 rev/min. Since PVA simultaneously acts as an emulsifier an uneven distribution of the PVA concentration at the interface can be expected upon deformation. Therefore an apparent higher interfacial tension acts on the droplets and much larger values of Ca are required to obtain some degree of anisotropy. In our prediction of the droplet's deformation upon influence of shear, coalescence of the emulsified drops is neglected. However for concentrated dispersions (>20 vol%) coalescence cannot be fully excluded.

7.2.3.2 Fixation of single deformed droplets in elongational flow

The results of the preparation route for elongated DCPD-filled microcapsules using a droplet deformation in elongational flow are presented in Table 7.3. The degree of elongation on the droplets was controlled by injecting the DCPD/PVA/water suspension into the reactive DETA bath for different viscosity ratios and at different flow rates.

Table 7.3: Results of the preparation route for elongated microcapsules *via* elongational flow for different viscosity ratios and different flow rates. For the different experimental conditions particle size distribution after injection is given. Optical microscopy images as inset show the obtained morphology of the microcapsules.

Injection rate	$\lambda = 0.054$	$\lambda = 0.030$
0 (Initial)	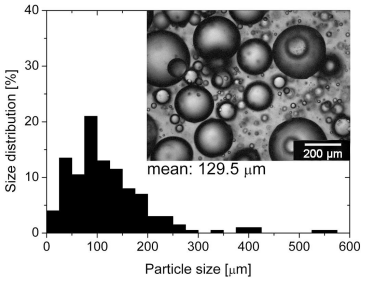	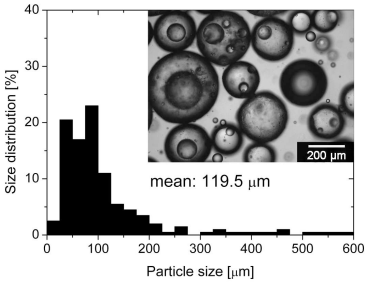
0.85 ml/min	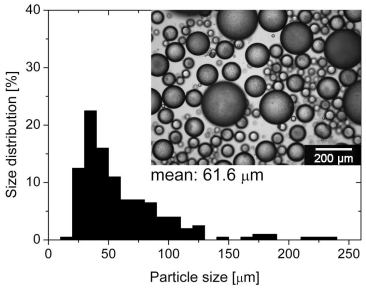	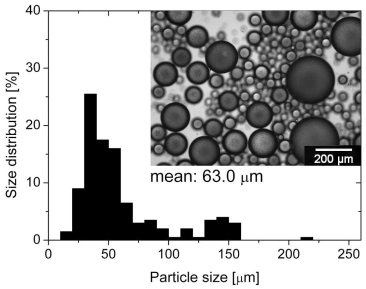
1.30 ml/min	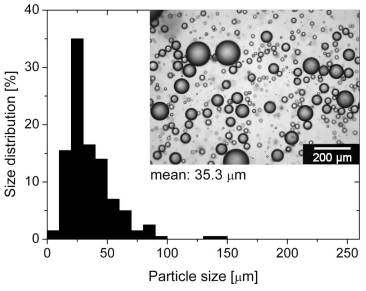	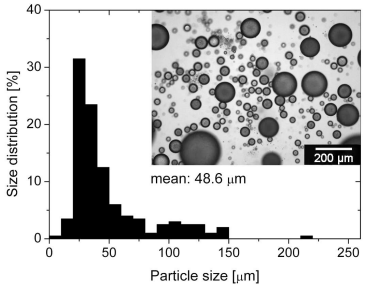

From the micrographs it can be observed that the deformation of the droplets did not successfully result into the fabrication of elongated microcapsules. The resulting microcapsules were nearly all perfectly spherical in shape. The lack of anisotropy may be the result of insufficient elongation in the capillary, relaxation of the deformed droplets inside the capillary and/or droplet break-up when overstretched. Since the particle size distribution and the average particle size has significantly decreased after injection, it indicates that drop break-up is the predominant cause for the absence of elongated structures, as was also the case in the Couette experiments. This phenomenon shows that at these moderate injection speeds droplet break-up is occurring, fragmentising the initial emulsion size distribution. Knowing that the critical capillary limit is significantly lower than for plain shear, the droplet break-up for elongational flow is a limiting factor (see Figure 7.1).

The difference in drop break-up morphology between the two viscosity ratios appears to be trivial as the average particle sizes and size distributions for both values of λ are comparable at the two injection rates studied.

7.3 Preparation of anisotropic microcapsules by ink-jet printing technology

7.3.1 Introduction

Besides the encapsulation of liquids through emulsification steps, alternative existing encapsulation routes involve the extrusion of droplets of the phase to be encapsulated and that of a coating material. A frequently reported technique is the so-called double extrusion principle.[139] This procedure is schematically drawn in Figure 7.6a. In such a procedure the phase to-be-encapsulated is extruded simultaneously with an outer fluid which contains the shell wall material. Since the primary liquid is extruded within the secondary liquid, a drop formed at the tip of the device exhibits a core-shell morphology. Upon release of the droplet the shell wall will be created, such as by removing the solvent from the outer liquid either by coagulation or evaporation. The double-extrusion concept is also used in the preparation of hollow and filled nanofibres through electrospinning.[140]

A variant of this double-extrusion principle was developed by TNO[141] and describes the encapsulation of single extruded droplets by shooting them through a film of a secondary liquid. This variant allows the production of uniformly sized microcapsules of nearly any liquid at a very high rate using a piezo-controlled ink-jet printing head operating at frequencies up to 25 kHz. The speed at which the liquid is fed to the printing head can be tuned to penetrate the liquid film and to deform the extruded droplets upon impact.

Due to intellectual property issues not all technical aspects of the experiments can be reported in this thesis.

7.3.2 Experimental

7.3.2.1 Materials

Stearine, sodium silicate (Na_2SiO_3), sodium alginate, dibasic ester (DBE, a commercial DuPont blend of di-functional C4-C6 esters) and calcium chloride were purchased from SigmaAldrich, The Netherlands. HCl (37% H_2O solution) was ordered from Acros Organics, Belgium. All materials were used as received. Prior to use the HCl was diluted to a 4 *M* solution.

7.3.2.2 Creation of deformed microcapsules by ink jet-screen printing

In a typical experiment 1 *l* of molten stearine, 2.5 wt% sodium alginate or 2.5 wt% sodium silicate water solution was used to create a liquid film of controlled uniform thickness. In parallel *ca.* 50 *ml* of liquid to be encapsulated, *e.g.* DBE, was poured into a reservoir leading to the printing head. The liquid was fed to the printing head under pressure at the desired rate. The nozzle inside the printing head was controlled by a piezo actuator connected to a high voltage power source with tuneable frequency. At the printing head the feeding liquid was extruded into a stream of drops. The shape and rate of the produced droplets was monitored using a stroboscopic light source and a CCD camera. A schematic figure of the encapsulation set-up is given in Figure 7.6b

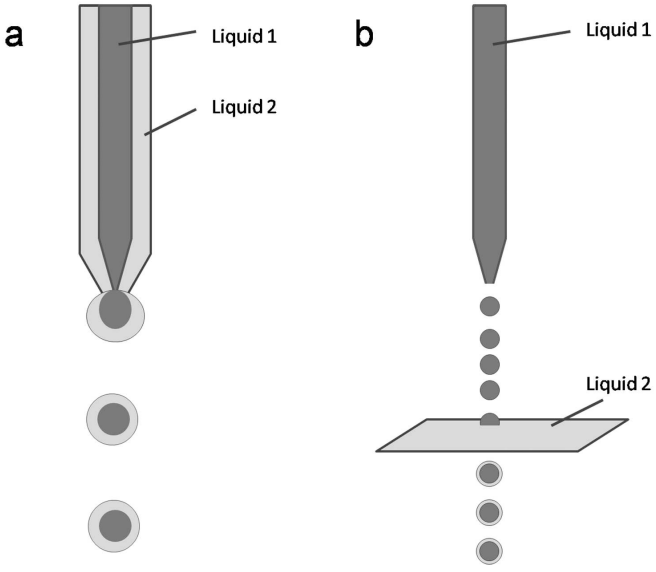

Figure 7.6: A schematic of a) classic double liquid extrusion encapsulation procedure and b) newly developed liquid screen printing encapsulation set-up.

The liquid film was positioned perpendicular to the jet of drops in such a way that the film was breached symmetrically by the incoming droplets. The impact position of the droplet jet could be altered when changes in the film were observed. After passing through the liquid film the drops were caught into a petri-dish containing the necessary coagulation liquid for the experiment.

Stearine crystallised already in air after leaving the screen and was collected in cold water containing 10 vol% of isopropanol. Sodium alginate was coagulated in a 5% solution of $CaCl_2$ and sodium silicate was reacted into silica by catching the coated droplets in a 4 M HCl solution.

7.3.3 Results & Discussion

The printing of DBE with stearine as a liquid screen resulted in the production of non-spherical particles when a printing flow rate of 4 ml/min and a printing frequency of 15 kHz were employed. A microscopic image of the DBE encapsulated stearine particles is given in Figure 7.7. The micrograph shows elongated particles indeed. However, it can be deduced from the image that the shell wall of the dried particles was not uniform in thickness (opaque and transluscent parts of the capsules). The stability of the capsules is poor and the capsules collapse upon removing from suspension. The shell wall ruptures at one end of the capsules (translucent part) and the DBE escapes from the vacuoles rapidly, leaving an empty capsule. The elongation of the particles occurs when the microdrops leave the stearine screen. The stearine is then drawn from the film by the moving drop, while at the same time it crystallises. Essentially the elongated shape of the particles consists of a nearly spherical liquid drop embedded in a 'tadpole' like particle.

Replacing the screen liquid with solutions of sodium alginate or sodium silicate however only results spherical particles, which agrees with the hypothesis that processes of drawing and crystallisation of the stearine upon exiting of the film creates a tail of material on the particle.

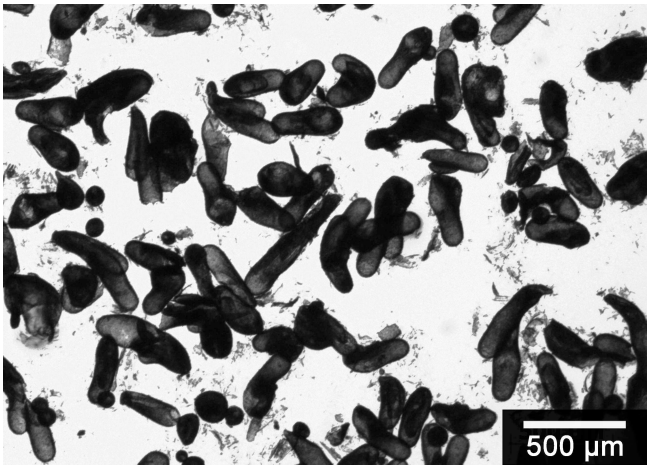

Figure 7.7: Non-spherical stearine DBE-filled microcapsules fabricated with the ink jet-printing encapsulation route

7.4 Route to anisotropic capsules *via* Pickering stabilisation

7.4.1 Background

A common feature of oil-in-water emulsions stabilised with surfactants is that such oil droplets invariably have a spherical shape when not exposed to external forces. When the droplets are deformed they normally re-adapt their initial shape upon relaxation. However, wen surfactants are replaced by solid particles, also refered to as Pickering particles[94,142] it can be prevented that the droplets relax back to the spherical shape. These particles' favourable surface wetting behaviour enables them to adhere strongly on liquid-liquid interfaces.[95,97] Once adhered, they cannot leave the interface under normal low-shear conditions in a closed system. The energy barrier to re-enter either one of the bulk phases is several orders of magnitude larger than the thermal energy, k_BT.[97,143] The strong adherence of effectively non-compressible particles offers additional potential for them to create stable non-spherical emulsion droplets. In order to adhere the particles to the interfaces the ζ-potential typically needs to be reduced between -30 and 30 mV,[144] which can be achieved by either variation of pH[145] or addition of electrolyte.[146] This is done to reduce the charge double layer and thus inducing colloidal stability.

When Pickering stabilised droplets are deformed, their surface area increases accordingly. The increase in the interfacial area of the two liquid phases allows adherence of additional particles if an excess of particles is present in either of the two phases. Provided the elong-

ated shape is maintained long enough, also the elongated interfacial area will be fully covered by the Pickering particles. Upon relaxation of the flow stress the droplet will tend to restore its spherical shape and reduce its interfacial area. However, this contraction is prevented by solid state jamming of the particles at the interface. Hence, the elongated shape is preserved.

To ensure an excess of particles, able to saturate the increased interfacial area upon deformation of the emulsion droplets, a simple coverage calculation can be done in order to determine the maximum number of particles that can fit on the desired initial spherical shaped interface.

$$Coverage = \frac{A_{part}^{cov}}{A_d} = \frac{1}{\pi}\frac{w_{part}}{w_d}\frac{\rho_d}{\rho_{part}}\frac{r_d}{r_{part}} \tag{7.6}$$

where A is the surface area and $part$ and d denote the particle and the dispersed phase respectively. The other parameters: w is the weight, ρ is the density and r is the radius. The coverage of a 100% (1.0) is used, since a saturated coverage of the droplets is desired for a jammed interface. Under the experimental conditions approximately 1 g of Pickering Particles (diameter: $\approx 300\ nm$) is used to emulsify ca 20% DCPD (density: 986 kg/m^3 at 25^{o}C) in water. Typical dispersion sizes are 600 - 1000 μm. Thus, the ratio of the radii in eq. 7.6 is in the order of 10^3 thereby securing an excess of particles in the order of 10^2.

7.4.2 Experimental

7.4.2.1 Materials

Styrene monomer, basic alumina, toluene diisocyanate (TDI), sodium chloride (NaCl) and 1-bromohexane were obtained from SigmaAldrich, The Netherlands. Dicyclopentadiene (DCPD, 95% endo) and diethyltriamine (DETA) were purchased from Acros Organics, Belgium. Laponite RD was kindly donated by Rockwood additives, UK. AIBN initiator (2.2'-azobis(isobutyro-nitrile)) was purchased from Wako, UK. Divinylbenzene (DVB, 80% technical) was purchased from Fluka. Styrene and DVB were passed over basic alumina to remove the radical inhibitor prior to use. The other materials were used as received without further purification.

7.4.2.2 Synthesis of clay-armoured polystyrene latex particles

Crosslinked polystyrene (PS) particles that are used to create stable spherical and anisotropic emulsion droplets in emulsion were synthesised *via* a mini-emulsion polymerisation using either laponite clay or ethylene-maleic anhydride copolymer as dispersing agent.[147]

In the experiments 1.00 g of laponite clay or 5 ml of 2.5 wt% EMA/H_2O was dispersed in 100 ml de-mineralised water solution inside a round-bottom flask and was subsequently

sonicated for 1 *min* whilst stirring applying a Cole-Palmer 750 W sonifier at 50% intensity. After 1 *min* sonication NaCl was added to obtain a 0.1 M solution, and sonication was continued for another 3 *min*, with a 30 *s* interval in which the solution was allowed to cool down. Next, a mixture of 7.50 *g* styrene, 1.50 *g* of DVB and 0.22 *g* of AIBN was added to the water clay suspension. To obtain non-soluble polymer latex particles, divinylbenzene (DVB) was copolymerised with styrene monomer by a free radical reaction, initiated by AIBN.

Another sonication treatment of 5 *min*, in five series of 1 *min* using a 30 *s* interval, was used to create a stable mini-emulsion of the organic phase in the water. Subsequently, the flask containing the mini-emulsion was put into an oil bath under flowing N_2 and heated to 65^oC and the monomer mixture was polymerised overnight for 16 *h*.

The synthesised latex of polystyrene was characterised using Dynamic Light Scattering and Scanning Electron Microscopy to determine size (distribution).

7.4.2.3 Creation of a stable DCPD/water emulsion

A stable microemulsion of DCPD in water was created using the (clay armoured) crosslinked latex particles synthesised earlier. For the preparation of the emulsion a glass vial was filled with 100 *g* of de-mineralised water together with 0.30 *g* of NaCl. The vial was hand-shaken to dissolve the NaCl and subsequently 12.5 *g* of the PS latex solution (solid content: 9 wt%) was added drop-wise to the solution. A sonication treatment of 3 *min* was applied to re-disperse the latex particles in the aqueous solution. In the case of creating anisotropic microcapsules, parallel 20 *g* of DCPD monomer was mixed with 17 *mmol* of TDI. From this mixture a quantity of 2 *g* was added to the latex particle suspension. With mild stirring stable DCPD colloidosomes[93] could be created with ease in water with a droplet size of 100-1000 μm that are stable for weeks.

In the case of spherical capsules the droplets with the polystyrene particles at the interface were directly fixed (also referred to as scaffolding[107]) by addition of 1.2 *g* DETA to the emulsion, creating polyurea DCPD filled capsules by interfacial polymerisation.

7.4.2.4 Stretching and encapsulation of Pickering stabilised droplets

For the creation of anisotropic droplets and capsules the method described by Bon *et al.*[110] was followed. In order to test the ability of the synthesised particles to form anisotropic droplets, macroscopic ($\approx$ 600 μm) non-scaffolded Pickering stabilised DCPD droplets dispersed in water (with excess of latex particles) were pushed slowly back and forward periodically through a narrow 'hourglass' shaped glass capillary. This capillary being thinner at its mid-section than the created droplets, forces them to stretch, resulting in the extra surface area. A pulsating procedure was applied to stimulate mixing and promoting liquid-liquid interface assembly of the dispersed excess of Pickering particles. The shape and dimensions of the capillary are schematically shown in Figure 7.8. For the production of anisotropic microcapsules $\approx$ 40 μm sized droplets, stabilised with a tenfold higher amount of Pickering

particles, were once passed through a long (100 mm) and more narrow glass capillary (minimum inner diameter: 20 μm) made by drawing a hot glass pipette tip in a methane flame. Equally in this procedure a pulsating flow was applied to stimulate mixing and promoting liquid-liquid interface assembly. Droplets exiting from the capillary were caught in a gently stirring solution of water, 0.1 M NaCl and DETA, where they were fixed as capsules by the interfacial polymerisation of TDI and DETA to create a polyurea shell wall.

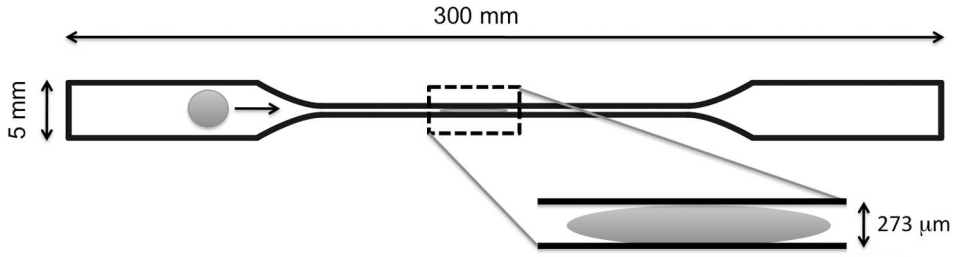

Figure 7.8: Schematic representation of the Pickering stabilised emulsion droplets deformation procedure in the custom made glass capillary

After formation of the shell wall the suspended microcapsules were filtered off and were washed with a large volume of diluted HCl to remove the remaining DETA. The filtrate was then washed extensively with a large excess of water and was allowed to dry in air.

7.4.3 Results & Discussion

The synthesised PS latex particles were relative homogeneous and had a nearly monomodal size distribution as recorded with SEM and DLS. From the SEM investigation of the latex particles on carbon tape (Figure 7.9a) it can be observed that the particles are all spherical and armoured with the laponite clay particles as the outer surface of the particles has a non-smooth texture. From Figure 7.9b it is found that the average latex particle size is 0.34 μm and has a polydispersity of 1.2, which correlates to the particle size shown in the SEM micro-graph.

Before the stretching of the macroscopic droplets inside the hourglass shaped capillary (this to test the ability of Pickering particles to form stable non-spherical droplets) many type of known Pickering stabilisers were evaluated in their emulsion stability. Among the examined solid stabilisers, ranging from poly(methyl methacrylate) microgels,[148] titanium dioxide nanoparticles[149] and Laponite clay armoured cross-linked polystyrene submicron spheres,[107] the clay armoured PS latex particles proved to be most versatile solid stabilisers for obtaining stable emulsion droplets for various organic liquids in water.

In the hourglass capillary test the synthesised PS sub-micron spheres were able to create non-spherical droplets of DCPD, styrene and 1-bromohexane after only passing droplets half a dozen times back and forward, with total residence times of approximately 15 s. When

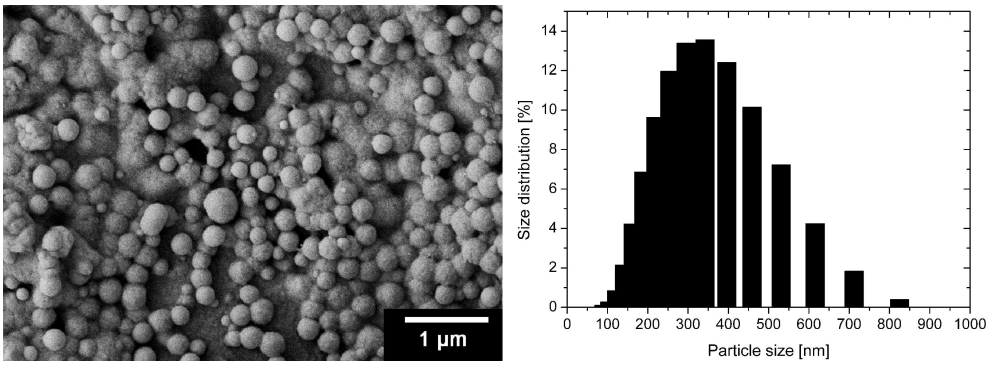

Figure 7.9: Scanning Electron Microscope image of the synthesised Laponite armoured PS latex particles on carbon tape and their size distribution curve

more than a single droplet was inside the capillary the droplets did not coalesce (inside nor outside the mid-section) and all the droplets were deformed similarly. The droplets remained non-spherical after relaxation in the outer parts of the capillary where the diameter is much larger than the droplet diameter. Without optimisation the aspect ratios of the shaped emulsion drops exceeded a value of 10 and their cross-sectional diameter was in the order of the capillary geometry. As expected, droplets with initial diameters smaller than the capillary did not deform and remained spherical. A representative image of undeformed and deformed Pickering stabilised droplets of styrene monomer are given in Figure 7.10. Droplets stabilised with EMA did not exhibit this induced anisotropy phenomenon by passing through the capillary, since surfactant molecules can easily rearrange or desorb to create a minimal droplet interfacial area, resulting in spherical droplets. This could be easily visually observed as the capillary is translucent. Hence, the anisotropic droplet geometry can solely be obtained upon elongation of the droplets by confinement inside the thinnest part of the capillary.

The incidental and singular creation of non-spherical particles *via* Pickering particles has been reported in literature,[150–152] but the mechanism has not been used intentionally to produce elongated particles on a larger scale.

In the work of Subramaniam *et al.* it was shown that similar Pickering systems, using polystyrene particles, were used to create non-spherical and even anisotropic bubble and droplet geometries.[153,154] In comparison to this work, Subramaniam *et al.* mainly focused on the merging of two gas bubbles. With their procedure they were able to create anisotropic moieties with aspect ratios higher than 10, comparable to our results.

The non-spherical droplets appear to be stable in suspension, but exhibit fragmentation or coalescence in time when being in contact with a water/air interface. To overcome this, most of the explorational experiments in the hourglass capillary were performed with 1-bromohexane as the dispersed phase, which has a density higher than that of water. Anisotropic droplets of the latter phase could easily be resuspended into a beaker after passing through the capillary and remained intact when gently stirring.

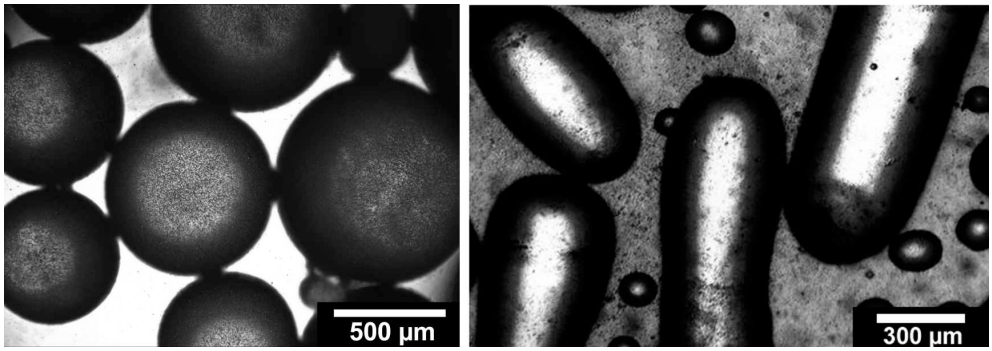

Figure 7.10: Optical microscopy image of stable a) initial spherical Laponite armoured PS stabilised DCPD droplets and b) deformed high-aspect ratio DCPD droplets created by passing the spherical droplets through the hourglass shaped capillary

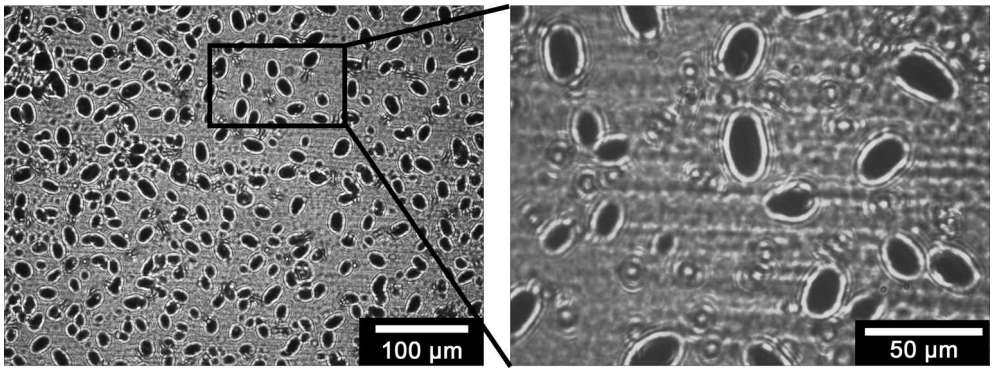

Figure 7.11: Optical microscopy images showing a) anisotropic microcapsules built from Pickering stabilised emulsion droplets at 10x magnification and b) a local magnification at 20x

The time dependent stability of the other liquids (DCPD and styrene monomer) requires fast scaffolding of the droplets in order to capture the anisotropic geometry. Uniform anisotropic DCPD capsules were made by pushing dispersed ($\approx 40\ \mu m$ size) DCPD (+TDI) drops through the narrow glass capillary and by directly injecting them into the the reactive DETA/water solution. The interfacial polymerisation through isocyanate and amine condensation led to the formation of capsule shell walls, encapsulating the DCPD emulsion droplets. When polymerised, the anisotropic shape was fixed and the produced microcapsules that are shown in Figure 7.11 clearly exhibit some degree of anisotropy.

The average aspect ratio for the deformed droplets was found to be 1.47 with a standard deviation of 0.18 (Figure 7.12) and was determined by measuring the long and short axis of 200 individual microcapsules in optical microscopy images. The degree of anisotropy is limited compared to experiments performed on larger droplets inside the 'hour glass' capillary.

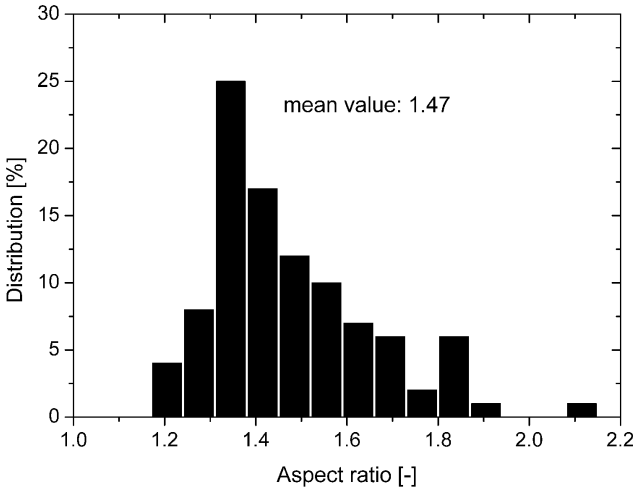

Figure 7.12: Distribution diagram of the Pickering stabilised induced microcapsule anisotropy via droplet elongation, demonstrated in Figure 7.11

The droplets did not elongate to a large extend, since the initial diameter of the $\approx 40\ \mu m$ particles was in the order of the size of the capillary. Furthermore, the excess of Pickering particles used in this experiment was only in the order of 10^1 and could have been insufficient to adequately maintain the droplets elongated shape upon relaxation.

The anisotropic polymer microcapsules created were stable at the air/water interface while remaining in water suspension. Despite this increase in stability in suspension, drying of the capsules after washing did not result in individually separated microcapsules, since the microstructures had collapsed, analogous to the encapsulated DCPD using the interfacial polymerisation between adipoyl chloride and DETA.

7.5 Conclusions

In this chapter different routes towards anisotropic microcapsules are evaluated. Encapsulation of deformed droplets in plain shear and elongational flow does result in a low degree of anisotropy (maximal 2.2) for a very restricted shear rate regime only. The instability of the deformed droplets in the high shear regime prevented the production of desirable high aspect ratio microcapsules and led to fragmentised structures which are most probably the effect of uncontrolled vibrations of the Couette set-up. All microcapsules produced using interfacial polymerisations by AC and DETA were stable in suspension but collapsed upon drying.

A novel ink-jet printing technique to encapsulate liquids and to produce anisotropic mi-

crocapsules can indeed lead to the production of elongated microcapsules, but the printed particles exhibited non uniform shapes and appeared unstable over time. Additionally the printing procedure is technologically challenging as the liquid film through which the liquid is printed is sometimes unstable and thus often an unwanted mixture of liquid-filled and solid particles is obtained.

The developed route via Pickering stabilisers provides the most successful route towards anisotropic high aspect microcapsules. Common Pickering stabilised emulsion droplets were easily deformed and stable elongated droplets up to aspect ratios of 10 were created. They could be scaffolded into microcapsules with similar geometries.

Unfortunately, the routes described here did not lead to the large scale preparation of elongated liquid filled capsules for the design of self-healing materials. However, the ultimate goal of producing high aspect microcapsules should be further explored as the potential impact on the self-healing release characteristics is shown to be significant.

CHAPTER 8

Compartmented fibre as novel liquid container

The miller: "You know, I've got a daughter who can spin gold from straw".
- The King: "Now, that's an art I can appreciate"."

From Rumpelstiltskin by the Grimm brothers

8.1 Introduction

Hollow fibres as storage and delivery system was one of the first concepts presented in literature for the fabrication of autonomous self-healing materials. These materials normally consisted of a conventional matrix structure that contained a certain fraction of liquid-filled capillaries.[11] At first the concept was demonstrated to work for concrete, but was quickly extended to polymer matrices.[12] The use of such capillaries in fibre reinforced polymer composites was presented not much later by others, thereby making use of the reinforcing effect of the capillaries in addition to their ability to release healing agent.[14,15] The capillaries used in both systems, are continuous drawn glass tubes with a typical inner diameter of 50 μm. Before embedding them inside the composite material the glass capillaries were pre-filled with a healing agent. An inclusion of liquid filled capillaries has several major advantages compared to the use of individual capsules containing the healing agent: 1) the capillaries can be more easily integrated in the fibre composite, 2) the rupture probability of such a

[0]Partly based on: S.D. Mookhoek, H.R. Fischer and S. van der Zwaag, *European patent application EP1983025*, **2008**

high aspect ratio capillary is large compared to the use of randomly dispersed capsules, *i.e.* they provide a large amount of healing-liquid per fracture event (see also Chapter 6) and 3) the rigid glass capillaries provide some reinforcement along the capillary major axis. However, the downsides of the use of capillaries relate to the difficulty of manufacturing, filling them with healing-agent, subsequent sealing and the relatively large liquid volume stored in such a capillary. Because the fibres are a continuous medium, upon cracking of the capillary liquid will be drained from the tubes as long as the net capillary action of the damage site is higher than that of the tube. Hence local fibre fracture could affect a large volume of the tube, thereby depleting the liquid from the capillaries over a vast length of the composite. In case of multiple cracking at different sites this depletion effect will decrease the future healing potential of the composite well away of the site of first damage. Additionally, in case a (catalysed) chemical reaction is started off after the deployment of the healing agent, the risk exists that the reaction will propagate into the tubes, solidifying the whole capillary interior and thus disabling the healing mechanism for future damage occurrence. The *pros* and *cons* of the two currently existing liquid-container design concepts, *i.e.* filled discrete spherical capsules and filled continuous hollow fibres, are summed up in Table 8.1.

Table 8.1: *Pros* and *cons* of the currently applied geometries for containing healing-agent

Current container design	Damage sensitivity	Rel. amount of released liquid	Manufacturing ease	Fit to composite
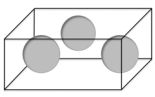	−	−	+	−
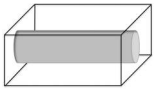	+	+	−	+

Table 8.1 directly shows that the characteristics of the two concepts are complementary and that a hybrid of the two concepts would be beneficial for the advancement of liquid-based systems as a whole. Hence, the design of anisotropic microcapsules was presented earlier in Chapter 7 being applicable for non-fibre reinforced materials. For the latter class of materials a more fibre-like design of the liquid-carring medium, analogue to the capillaries, is preferred which could still provide mechanical reinforcement to the matrix material. At the same time the more macroscopic form of a fibre can be handled better and provides positional freedom, *e.g.* placement at damage prone sites. A possible solution can be found in liquid carrying fibres that are compartmented. Such fibres overcome the disadvantages indicated above and

provide still some form of reinforcement, or fit to the composite architecture in general.

Hence, in this chapter a facile production route to polymeric fibres, comprising multiple liquid cavities, is presented to enhance the healing potential of self-healing fibre composites. These fibres allow controlled release of healing agent and provide a multiple distributed healing capability.

8.2 Background

For the purpose of spinning the compartmented polymeric fibres, alginic type of polymers provide several suitable properties, such as 1) water-solubility, 2) fast coagulation in the presence of divalent ions and 3) adequate mechanical properties.[155] Alginates are natural derived polysacharides, extracted from brown sea algae. The linear polysacharides are co-polymers and consist of individual α-L-guluronic (G) and β-D-mannuronic (M) acid blocks and of alternating blocks of the two (GM). The G-blocks can be bound together (inter- and intra-molecular) by divalent cations, forming a gel which gives rise to a three-dimensional network known as the "egg-box model".[156] The affinity of alginate polymer towards various divalent ions has been investigated priorly by Haug and Smidsrod.[157,158] They have shown that the affinity of the polymer towards the cations increases in the following order: Mn < Zn, Ni, Co < Ca < Sr < Ba < Cd < Cu < Pb. Since the origin of the alginate will determine the exact structure of the alginate, the properties of the gelled material is therefore influenced by the choice of alginate material and crosslinking-ion. The crosslinking morphology of the alginate by the cations in the egg-box model is illustrated in Figure 8.1.

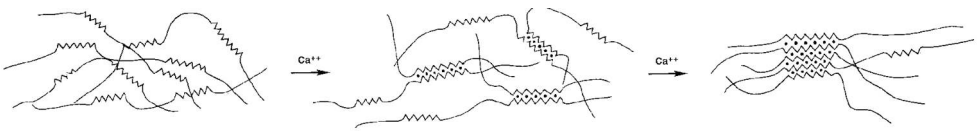

Figure 8.1: A simplified illustration of the crosslinking of alginate polymers with divalent cations. The G blocks of the polymer are indicated by the serrated parts form the so-called egg box around the cations (dots).

Fibres made of alginate have have been presented many decades ago, initially finding their use in the textile and food industry.[155] In the last two decades application of alginate fibres has been focused more on their biological and biomedical properties, such as for wound dressing, because of the material's biocompatibility and hemostatic capability.[159] Much work has been focused on tuning the fibres' mechanical in combination with their biological properties, for instance by combining alginate with other (natural) polymers such as gelatin, polyvinyl alcohol, etc.[160,161] The use of alginate to incapsulate liquid phases in spherical particles has also received significant interest in the preparation of drug carriers to be used

in-vivo.[162] The use of a fibre geometry for this purpose however has not been documented and only a few report on their use a as drug delivery medium,[159,163] most probably due to the inability to flow with the bloodstream. However, application of alginate fibres for the use of healing agent storage medium inside fibre reinforced composite materials, offers potential for the further development of self-healing composites because of the facile production route, ability to incorporate various type of healing agents and the potential to fit to the mechanical properties of the composite matrix polymer (*e.g.* Young's modulus, strain at break, tensile strength).

8.3 Experimental

8.3.1 Materials

Sodium alginate (250 mPa.s, 2% H_2O solution @ 25^{o}C), o-dichlorobezene (DCB), Ethylene-*alt*-maleic anhydride copolymer (EMA, M_w 100-500 kDa), calcium chloride hexahydrate and barium nitrate were purchased from SigmaAldrich, The Netherlands. Diethyltriamine (DETA) was obtained from Acros Organics, Belgium. Epikote 828 (Bisphenol A type epoxy - Hexion) was purchased from Wilsor resins, The Netherlands.

8.3.2 Preparation of an emulsion for spinning

For the spinning of alginate fibres, ultimately comprising multiple liquid-filled reservoirs, 5 g of sodium alginate is dissolved in 95 g water using a high shear impeller over a period of 30 min at room temperature. The process results in a viscous yellowish and slightly opaque solution. Subsequently, a solution of EMA in water (2.5 wt%), the exact concentration level depending on the ultimate desired morphology, is added to the alginate solution and stirring is proceeded for another 5 min. EMA is used as an polymeric surfactant to stabilise the emulsion later on. Then, for the preparation of an oil-in-water emulsion 20 g of the alginate/ema-water solution is poured into a different beaker, equipped with three-bladed mechanical impellor. The shear of the impeller is set to a value desired for the creation of the healing-agent dispersion and 2 g of DCB, a potential healing agent for thermoplastic materials, was slowly added to the stirring alginate/ema-water solution (Chapter 3). The system was sheared over a period of 10 min to create a stable emulsion.

In order to control the morphology of compartmented nature of the fibres, different fibre spinning emulsion were made. By changing the concentration of emulsifier the morphology of the initial emulsion and that of the resulting fibre compartments can be tailored. In table 8.2 the recipe for the different systems are given. The impeller rotational speed and other specs of emulsification were kept identical in all experiments.

Table 8.2: Recipes for the preparation of spinning emulsion

Components [g]	System A	System B	System C
H_2O	19.0	19.0	19.0
sodium alginate	1.0	1.0	1.0
EMA (2.5wt% sol.)	4.0	2.0	1.0
DCB	2.0	2.0	2.0

8.3.3 Spinning procedure for compartmented fibres

The spinning of the emulsion proceeded *via* either a hand-held 20 ml syringe with a straight-cut needle of 255 μm in diameter (30 gauge) or a small-scale wet spinning process using a pilot-size aramid spinning line donated by Teijin Aramid, The Netherlands. The spinning of the fibres with the syringe proceeded by direct extrusion of the emulsion through the needle in a beaker containing a 0.225 M or 0.45 M solution of $CaCl_2$ in water or an equal molar concentration of $Ba(NO_3)_2$. The fibres were collected and were dried at room temperature while hanging.

The pilot-size spinning set-up was equipped with a motor controlled plunger-extruder, a heat controlled coagulation bath, and a tension controlled filament winder. A schematic set-up of the spinning-line is displayed in Figure 8.2a. The created DCB/alginate-water emulsion was extruded through a spinneret die at the bottom of the plunger at a rate between 40 and 50 $\mu l/min$. The spinneret used in these experiments had a single orifice with a diameter (D) of 250 μm. The design geometry of the spinneret is presented in Figure 8.2b. The length of the capillary was 2 mm, resulting a L/D of 8. The time between preparation of the emulsion and the spinning process was typically in the order of 5 min.

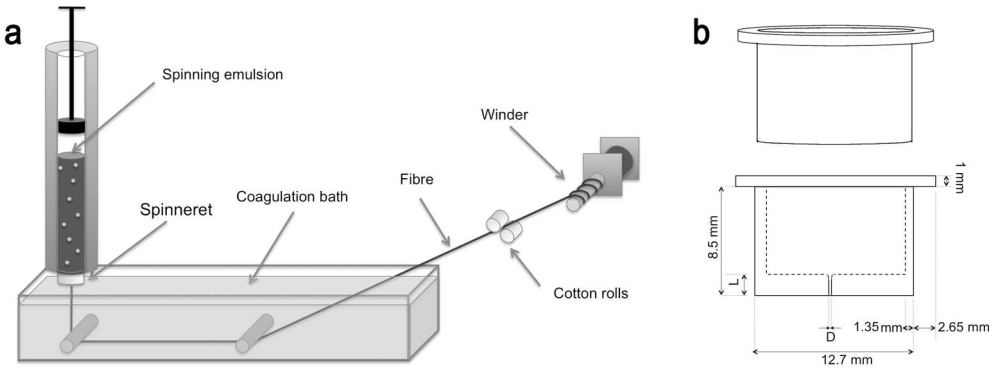

Figure 8.2: a) schematic of the wet-spinning line and b) design of the spinneret.

In this case the spinneret was submerged into the coagulation bath with a constant temperature of 25^oC containing a 0.225 M or 0.45 M solution of $CaCl_2$ in water or an equal molar concentration of $Ba(NO_3)_2$. The residence time of the fibre in the bath was of the order of 10 s. The coagulated fibre was led out of the coagulation bath and was dried between two cotton surfaces after which it was winded on a plastic bobbin under slight tension at a constant rate matching that of the extrusion (*i.e* draw ratio = 1). Afterwards the bobbin with the fibre was placed inside a fume-cabinet at room temperature with air convection to dry slowly over at least a period of 48 h before further testing.

8.3.4 Fibre characterisation

Optical, laser and scanning electron microscopy The fibres were characterized using a Leica optical microscope and an Olumpus LEXT laser scanning confocal microscope. Using these techniques, the fibre size, uniformity and morphology could be investigated.

Scanning Electron Microscopy (SEM) studies were performed on a JEOL 7200 Scanning electron microscope. Samples of both as-spun compartmented fibres and embedded fibres were deposited on carbon-coated tape and sputter-coated with Au.

Thermal analysis The compartmented fibres produced were characterised using thermal analysis to demonstrate the presence of the incapsulated phase and quantify their volume fraction of the fibre. Thermo Gravimetric measurements were performed on a Perkin Elmer Pyris diamond TG/DGA from 20 - 300^oC at a heating rate of 10 K/min. Typical sample weights were 5 mg.

Mechanical evaluation The mechanical properties of the compartmented fibres were evaluated using a standard tensile test on a Zwick/Roell load frame with a 10 N force cell. Prior to testing the fibres were aligned on a custom designed paper frame with a window gauge length of 30 mm. The placing and alignment of the fibre in such a paper window within the framework of the tensile load frame is illustrated in Figure 8.3.

The fibres were glued at the edge of the paper window with small quantities of cyano-acrylate glue. The paper window was clamped in the centre between the two grips of the tensile load frame. Subsequently, the sides of the paper window were cut by a pair of scissors along the indicated horizontal lines. The force was zeroed and the fibres were drawn at a rate of 0.3 mm/min, recording the force as function of cross-head displacement.

8.3.5 Embedment of fibres in a polymer matrix and microtoming

The fibres created were cut at equal length of 50 mm and bundled. Subsequently, the bundle of fibres was inserted vertically inside a PDMS rubber mold for a beam-type specimen with

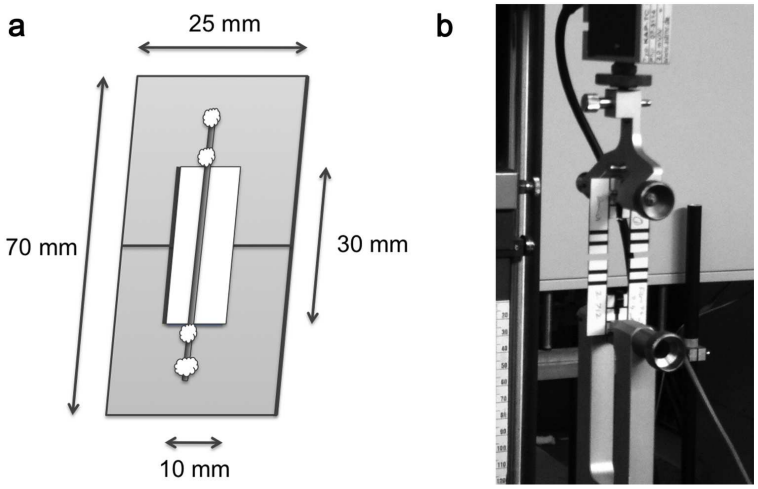

Figure 8.3: a) Illustration of the custom-made paper window for testing the tensile properties of the fibres created. The white dots indicate the points were the fibre had been glued to the paper. b) Tensile test set-up with paper window clamped inside the load frame.

typical dimensions of 50 x 10 x 4 mm, approximately occupying 15 vol% of the sample volume. Epoxy (Epikote 828) resin was mixed with 12 wt% of DETA and a small quantity of TiO_2 to make the matrix opaque. The resin was degassed using vacuum and carefully injected into the mold using a syringe making sure no air was trapped between the fibres.

Microtoming of the epoxy beams along the axis of the fibres was performed using a Leica sliding microtome using a cutting step of 5 μm. Optical microscopy was used to check frequently whether the fibre was exposed during cuts.

8.3.6 Cracking of compartmented fibre/epoxy composite materials

Compartmented fibre/epoxy samples were prepared as described in section 8.3.5, but a small quantity of disperse red dye was added to the DCB before incorporation inside the fibres. The beams were scored in the centre and perpendicular to the long-axis of the sample using a miniature file. Next, the beams were loaded using a 3-point bending set-up and cracked until failure. A piece of tape on the back of the sample prevented the two sample halves to separate. The undamaged and cracked beams were investigated under the laser scanning microscope.

8.4 Results and discussion

8.4.1 Spinning and fibre morphology

The DCB/alginate-water emulsions created were found to have different morphologies depending on the EMA concentration at which the emulsions were made. The morphology and the particle size distributions of the emulsions for systems A and B were studied using optical microscopy and recorded images are given in Figure 8.4. System C did not result in a stable emulsion and the DCB macroscopically phase separated from the alginate solution.

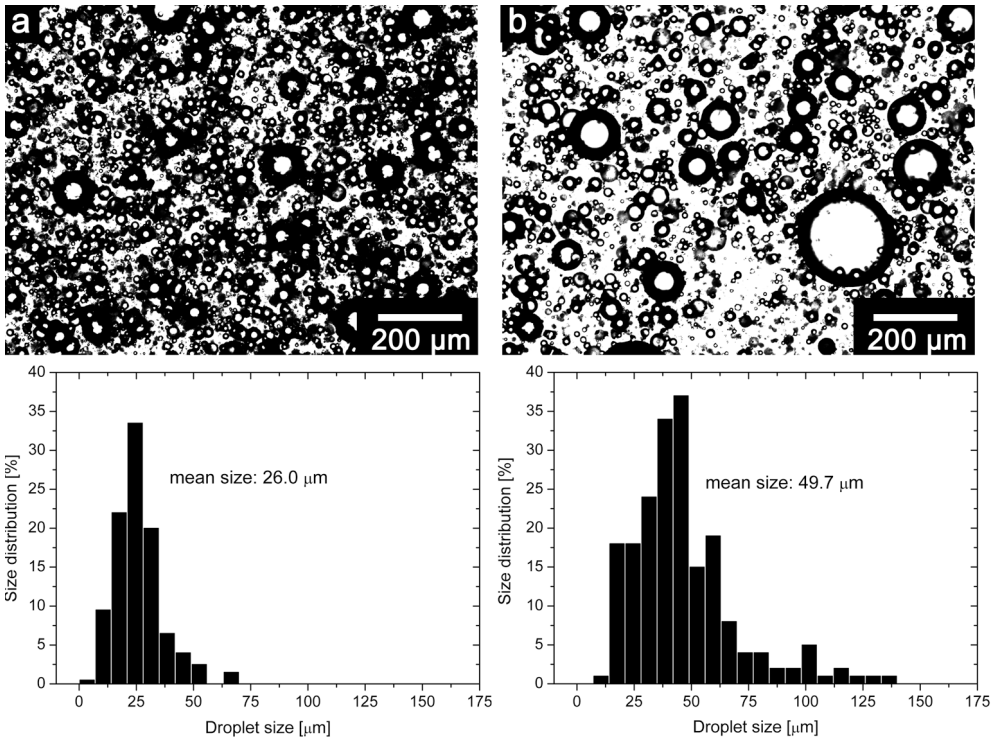

Figure 8.4: Optical microscopy images of the emulsions created of which the fibres were spun,; a) system A and b) system B.

Figure 8.4 qualifies the difference in droplet size for system A and B and shows that the average particle size in system B is about a factor of 2 larger. System A contains droplets with a mean size of 26 μm, while system B contains droplets of 50 μm.

Both systems could be extruded through the straight-cut needle or small die of the spinneret with ease without building up of large pressures. The dissolved sodium alginate could

be coagulated very fast by extruding the emulsion systems in water containing $CaCl_2$ or $Ba(NO_3)_2$.

In the spinning procedure it was found to be crucial to introduce a first drying step before the winding of the fibres. Hence, two cotton surfaces were introduced in the spinning line through which the fibre was guided before winding. Although the fibres remained wet the drying step prevented the fibres from sticking to themselves on the bobbin, making it possible to unwind them without damaging.

Smooth fibres with a relatively homogeneous diameter of 170 μm were obtained after drying when spun with the syringe as are presented in Figure 8.5. The fibres had either classical round shapes or were flat and ribbon-like, depending on the concentration of calcium and barium ions. Concentrations of 0.45 M resulted in round fibres (Figure 8.5). Flat fibres were obtained when lowering the concentration to a value of 0.225 M. It is observed that a low concentration of Ca^2+ and Ba^{2+} ions is not able to coagulate the fibre fully in the time of residence in the coagulation bath and only creates a strong skin, still containing an uncoagulated core. Upon drying of the fibre the water is removed from the core and the fibre collapses. Since the emulsified phase is no longer contained when the fibres collapse, compartmented fibres were made at ion concentrations of 0.45 M.

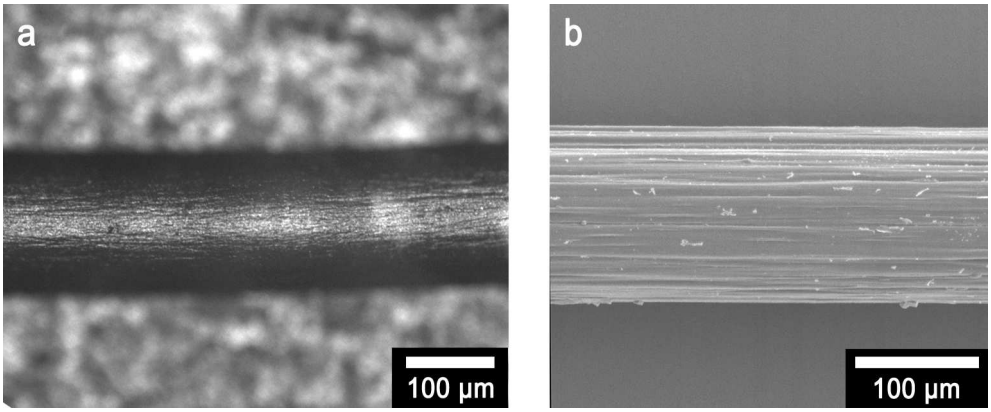

Figure 8.5: Microscopy images of the compartmented fibre outer structure, a) laser scanning microscopy and b) SEM

The priorly emulsified DCB was contained inside the fibres during the spinning of the fibres, since no DCB accumulated in the coagulation medium nor in the syringe or plunger.

The presence and content of DCB inside the fibres was confirmed using TGA. In Figure 8.6 both systems display an identical progression of the sample weight with increasing temperature. The curves show that the fibres still contained about 10% of water after drying. Water is removed in the initial heating of the sample and is indicated by a sloped decrease of the sample weight from room temperature up to around 100°C. Upon further heating DCB

escaped from the fibres around the boiling point of the liquid (194^{o}C) indicated by the large drop in sample mass. The DCB contents of the fibres was found significantly different for the two investigated systems. System A with the small average DCB droplet size contained about 45 wt% of DCB and system B close to 25 wt%.

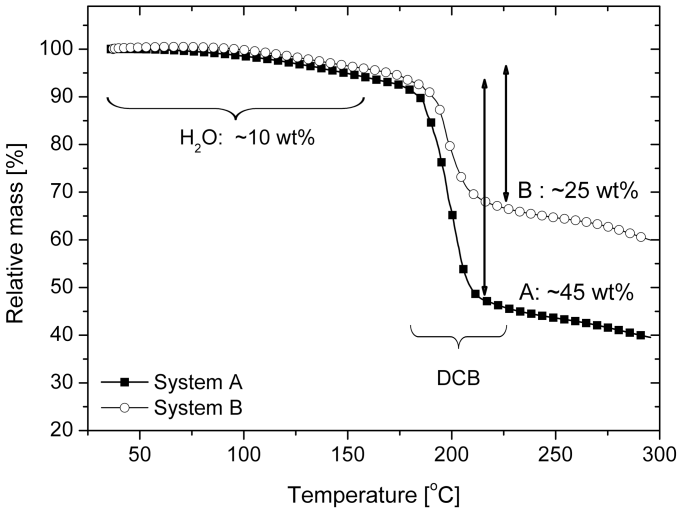

Figure 8.6: Thermogravimetric analysis of the fibres created, showing the content of the enclosed liquid for both systems.

Subsequently to the removal of DCB, the fibres themselves began to decompose slowly at temperatures above 220^{o}C indicated by the sloping curve towards higher temperatures.

The morphology of the fibres created from system A and B could be visualized by laser scanning microscopy. The images in Figure 8.7a and 8.7b clearly display the individual liquid compartments within the fibres and the difference between the two systems and indicates an internal compartment size of approximately 60 μm and 95 μm for system A and B respectively. After embedment of the fibres inside an epoxy-resin material, microtoming along the axis of the fibres revealed the observed morphology in great detail when investigated by SEM. Figure 8.7c shows that the very small-scale DCB dispersion of system A resulted in a very porous fibre with multiple individual compartments where the liquid is stored. The compartments have anisotropic shapes rather than spherical as the droplets are deformed by the elongational flow field during spinning. The compartments have volumes in the range of the emulsion droplets at which the fibres were created and several compartments are distributed over the fibre diameter. In Figure 8.7d the fibre longitudinal cross-section of system B is given. System B has resulted into a different fibre morphology in comparison to Figure 8.7c as only a few large compartments can be identified in the image of fibre cross-section. These compartments are anisotropic too but their volume is substantially larger and a single com-

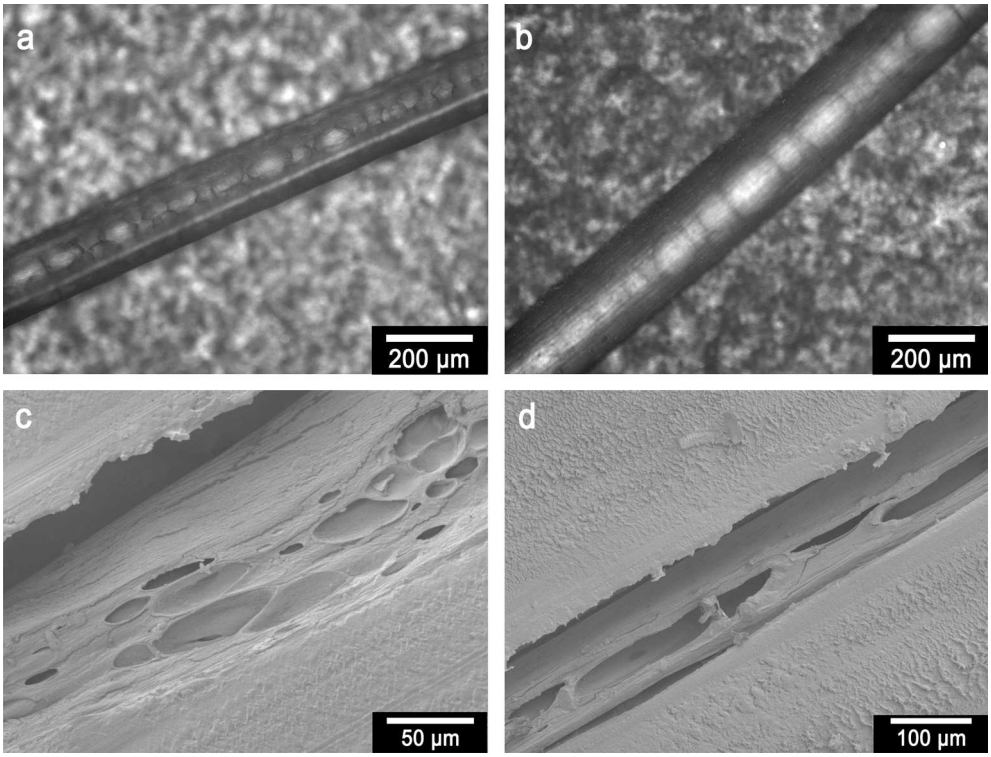

Figure 8.7: Inside compartmented morphology of the fibres created from a) system A (compartmented size $\approx$ 60 μm) and b) system B (compartmented size $\approx$ 95 μm) by laser scanning microscopy and SEM after microtoming

partment size approaches the fibre diameter, spanning the whole fibre width. The increase size of the compartments with respect to system A correlates to the larger emulsion dispersion of system B. Both systems however show a larger size of the compartments as would have been expected from the morphology of the emulsions, which indicated that coalescence of emulsified droplets must have occurred during spinning, increasing the average particle size inside the fibres.

The morphology of system B reveals the presence of aligned anisotropic reservoirs of healing agent, which have an increased healing potential based on their released volume per crack area (Chapter 6). Application of a well designed compartmented fibre therefore not only provides macroscopic handling and facile production of a healing-agent carrier it also can boost the healing agent release in general.

8.4.2 Characterisation of fibre properties and healing agent release

Appropriate mechanical properties of the fibres is crucial for their use a materials for releasing healing-agent in a self-healing system. The premature rupture of the fibre should be guaranteed when the matrix material cracks in order to release the liquid. The overall results of fibre tensile tests for fibres spun by the syringe method from system A and B are presented in Table 8.3.

Table 8.3: Results for fibre tensile experiments

Fibres	Preparation	$\langle d \rangle$ $[\mu m]$	$\langle E \rangle$ $[GPa]$	$\langle \epsilon^X \rangle$ [%]	$\langle R^X \rangle$ $[MPa]$
System A	syringe	167 ± 8	0.6 ± 0.2	3.6 ± 1	8 ± 2
System B	syringe	195 ± 10	0.9 ± 0.2	3.1 ± 1	5 ± 2
Optimised system B	spin-line	172 ± 7	1.6 ± 0.4	1.8 ± 0.5	23 ± 8

The influence of the morphology can be observed in the significant difference in fibre modulus for system A and B. The strain at break and the ultimate tensile strength of the fibres is comparable for the two types of fibre, however they have large standard deviations making it difficult to be conclusive on properties. Additionally the values of the ultimate strength are rather low for application of the fibres in composite material, which appear to be the effect of small defects along the fibre caused by a non-uniform extrusion rate. Hence, in an attempt to optimise the mechanical properties of the fibres system B was selected for spinning with the pilot-size set-up.

The extrusion of the emulsion was uniform and the residence time of the fibres within the coagulation bath was held constant at 10 s using the spinning line. The appearance, smoothness and average diameter of the fibres was comparable to that of the syringe spun fibres, but the uniformity along the total fibre length was much higher. The tensile test results for the fibres spun by controlled extrusion and coagulation on the spinning line are also presented in Table 8.3 for comparison. A representative set of curves for tensile tests performed on fibres made from a spinning experiment of system B are shown in Figure 8.8.

The optimised fibres of system B have enhanced properties with respect to the properties of the other two fibres when comparing modulus and tensile strength. In contrast the strain at break has been reduced as a compromise, making the fibres more brittle in nature. Although the strain at break is around 1.5-2.0 % on average the strain levels of commonly used composite resins such as epoxy are only a fraction higher and ensures the rupture of the fibre when the matrix cracks. The strain range at which epoxy resins commonly fail is indicated in Figure 8.8 by the grey coloured area. The elevation of tensile strength to a level in the order of 20 MPa now also provides the necessary mechanical properties for application in a composite material.

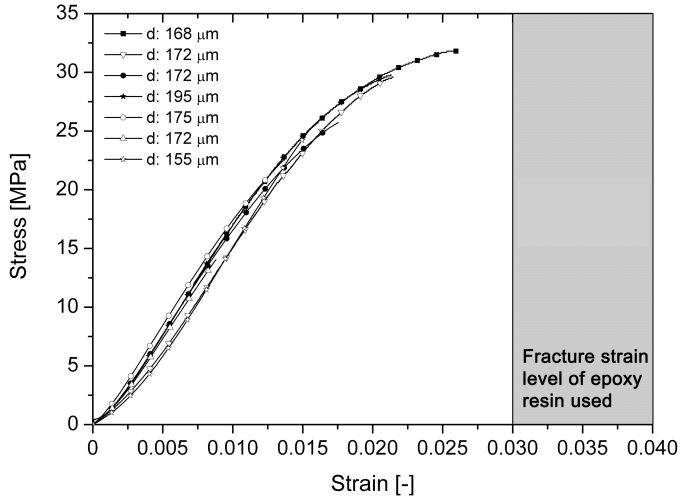

Figure 8.8: representative set of stress-strain curves for optimised fibres of system B, spun *via* use of the pilot-size spinning line, and the fraction strain level of the foreseen matrix.

Observations of the system behaviour following embedment of the fibres inside a polymer matrix and subsequent fracture of the composite, proved that the fibres rupture with the surrounding matrix and release their contents inside the crack. Figure 8.9a and 8.9c show an image of the epoxy composite surface and samples as a whole before scoring and fracture. The direction of the embedded compartmented fibres is indicated by the diagonal lines across the surface. Figure 8.9b displays an microscopy image of the same material surface but after the introduction of a crack. From the figure the released DCD with red dye can clearly be observed. The healing-agent even spread over the material surface when the two surfaces briefly made contact. This large amount of released healing-agent indicates that the compartmented fibre concept is able to release healing-agents in adequate quantities that are comparable to systems with spherical capsules such as presented in Chapter 3. When the material is cracked for a second time at at distance 7 mm away from the initial crack an equal liquid release was detected. Based on the compartment sizes derived from the morphology studies in Figure 8.7 a depleted zone around the crack of maximally 100 and 200 μm (approximately two times the compartment size) is predicted for system A and B respectively.

The fracture surfaces of the fibre-composite material were also investigated by optical microscopy and SEM and show that the fibre indeed was ruptured by the macroscopic crack through the matrix. Figure 8.9d displays a optical microscopy image of the fracture surface of a compartmented fibre/epoxy composite material showing the relative clean fractured end of a single fibre surrounded by the released red DCB .

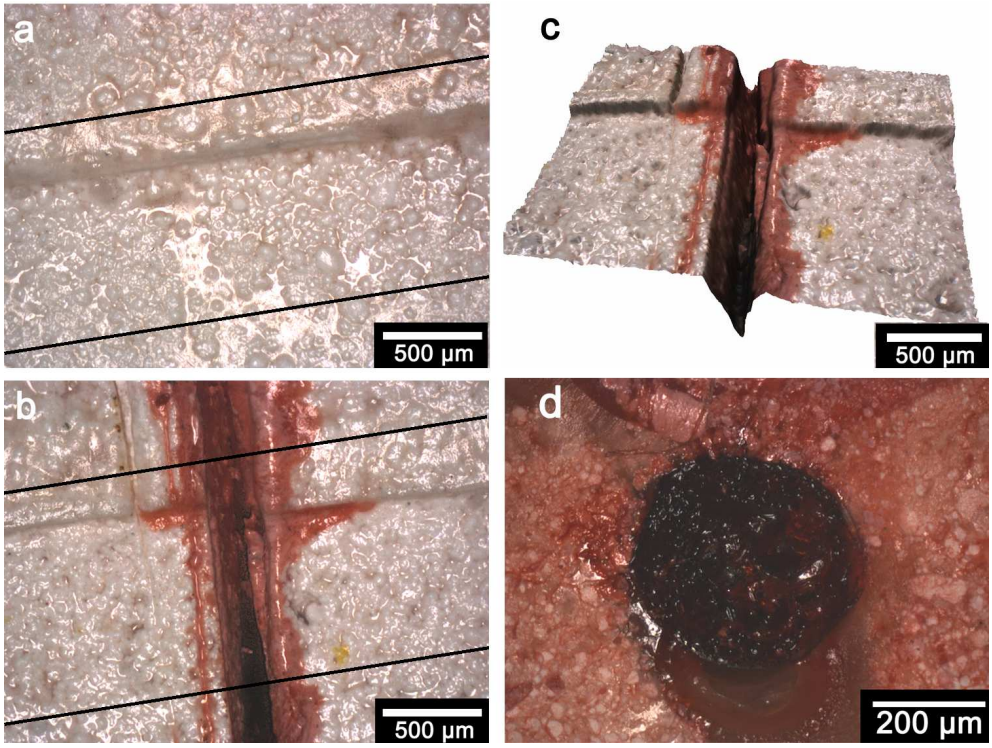

Figure 8.9: Optical microscopy images of a) the undamaged and b) cracked composite material comprising the compartmented fibres. The diagonal lines indicate the fibre orientation. Image c shows a laser confocal micrograph of the crack in 3D. The fracture surface, exposing the clean cleavage of the fibre surrounded by the released liquid is shown in d)

8.5 Conclusions

Polymer fibres with discrete liquid vacuoles inside can be created from spinning of emulsions of healing-agent in sodium alginate water solution. Coagulation of the alginate polymers enclosed the emulsified phase, thereby encapsulating the potential healing agent into a fibrous structure. The morphology of the compartmented fibres can be controlled by adapting the initial emulsion of which the fibres are spun. Anisotropic morphologies such as suggested in Chapter 6 and perused in Chapter 7 could be prepared, providing aligned anisotropic liquid compartments within a macroscopic structure. Healing agent content up to 45 wt%, depending on the compartmented fibre could be achieved.

The mechanical properties of the fibres highly depended on their preparation procedure.

Compartmented fibres with a modulus and strain at break around 1.5 GPa and 2.0 % respectively could be created *via* a spinning procedure using controlled extrusion, coagulation and winding. These properties are promising for the future development of self-healing composite materials based on these type of fibres, since the modulus and strain at break are close to those of commonly used composite resins such as epoxy.

Bibliography

[1] R. Seidel, A. Gourrier, M. Burghammer, C. Riekel, G. Jeronimidis and O. Paris, *Micron*, 2008, **39**, 198–205.

[2] P. Fratzl, and R. Weinkamer, *Prog. Mater. Sci.*, 2008, **52**, 1263–1334.

[3] J. R. Capadona, K. Shanmuganathan, D. J. Tyler, S. J. Rowan and C. Weder, *Science*, 2008, **319**, 1370–1374.

[4] A. Sidorenko, T. Krupenkin, A. Taylor, P. Fratzl and J. Aizenberg, *Science*, 2007, **315**, 487–490.

[5] R. Vaia and J. Baur, *Science*, 2008, **319**, 420–421.

[6] S. C. Cowin, *Ann. Biom. Eng.*, 1983, **11**, 263–295.

[7] D. B. Burr, A. G. Robling and C. H. Turner, *Bone*, 2002, **30**, 781–786.

[8] P. Martin, *Science*, 1997, **276**, 75–81.

[9] S. Van der Zwaag, *Self Healing Materials*, Springer, 2007, vol. 100.

[10] P. Fratzl and F. G. Barth, *Nature*, 2009, **462**, 442–448.

[11] C. Dry, *Smart Materials and Structures*, 1994, **3**, 118–123.

[12] C. Dry, *Composite Structures*, 1996, **35**, 263–269.

[13] M. Motuku, U. K. Vaidya, and G. M. Janowski, *Smart mater. Struct.*, 1999, **8**, 623–638.

[14] S. M. Bleay, C. B. Loader, V. J. Hawyes, L. Humberstone and P. T. Curtis, *Compos. A*, 2001, **32**, 17671776.

[15] J. W. C. Pang and I. P. Bond, *Composites: Part A*, 2005, **36**, 183–188.

[16] R. Trask, G. Williams and I. P. Bond, *J. Roy. Soc. Interface*, 2007, **4**, 363–371.

[17] H. R. Williams, R. S. Trask, A. C. Knights, E. R. Williams and I. P. Bond, *J. R. Soc. Interface*, 2008, **5**, 735–747.

[18] S. R. White, N. R. Sottos, P. H. Geubelle, J. S. Moore, M. R. Kessler, S. R. Siram, E. N. Brown and S. Viswanathan, *Nature*, 2001, **409**, 794–797.

[19] J. M. Kamphaus, J. D. Rule, J. S. Moore, N. R. Sottos and S. R. White, *J. R. Soc. Interface*, 2008, **5**, 95–103.

[20] D. S. Xiao, Y. C. Yuan, M. Z. Rong and M. Q. Zhang, *Polymer*, 2009, **50**, 2967–2975.

[21] M. W. Keller, S. R. White and N. R. Sottos, *Adv. Func. Materials*, 2007, **17**, 2399–2404.

[22] Y. C. Yuan, M. Z. Rong, M. Q. Zhang, J. Chen, G. C. Yang and X. M. Li, *Macromolecules*, 2008, **41**, 5197–5202.

[23] K. S. Toohey, N. R. Sottos, J. A. Lewis, J. S. Moore and S. R. White, *Nature Materials*, 2007, **6**, 581–585.

[24] T. Yin, M. Z. Rong, M. Q. Zhang and G. C. Yang, *J. Comp. Sci. Tech.*, 2007, **67**, 201–212.

[25] M. M. Caruso, D. Delafuente, V. Ho, J. S. Moore, N. R. Sottos and S. R. White, *Macromolecules*, 2007, **40**, 8830–8832.

[26] M. M. Caruso, B. J. Blaiszik, S. R. White, N. R. Sottos and J. S. Moore, *Adv. Funct. Mater.*, 2008, **18**, 1898–1904.

[27] T. Wu and S. Lee, *J. Polym. Sci.*, 1994, **32**, 2055–2064.

[28] W. Peng-Peng, *J. Polym. Sci.*, 1994, **32**, 1217–1227.

[29] H. Eyring and J. Hirschfelder, *J. Polym. Phys.*, 1937, **41**, 249–257.

[30] M. T. Cohen and D. Turnbull, *J. Polym. Phys.*, 1959, **31**, 1164–1169.

[31] H. Fujita and A. Kishimoto, *J. Polym. Phys.*, 1961, **34**, 393–398.

[32] A. E. Bozdogan, *Polymer*, 2003, **40**, 6427–6430.

[33] C. L. Bray, B. Tan, C. D. Wood and A. I. Cooper, *J. Mater. Chem.*, 2005, **15**, 456–459.

[34] N. Winterton, *J. Mater. Chem.*, 2006, **16**, 4281–4293.

[35] B. A. Wolf, *Pure Appl. Chem.*, 1985, **57**, 323–336.

[36] R. J. Wise, *Thermal welding of polymers*, Abington Publications, Cambridge UK, 1999.

[37] R. J. Wise and I. D. Froment, *J. Mater. Sci.*, 2004, **36**, 5935–5954.

[38] C. M. Hansen, *Hansen Solubility Parameters: A User's Handbook*, CRC Press, Boca Raton USA, 1999.

[39] J. H. Hildebrand and R. L. Scott, *The solubility of nonelectrolytes*, Dover Publications, New York, 1964.

[40] T. G. Fox and P. J. Flory, *J. Polym. Sci.*, 1954, **14**, 315–319.

[41] T. G. Fox, *Bull. Am. Phys. Soc.*, 1956, **1**, 123.

[42] R. P. Kambour, C. L. Gruner and E. E. Romagosa, *J. Poly. Sci.: Polym. Phys. Ed.*, 1973, **11**, 1879–1890.

[43] J. Rauch and W. Kohler, *J. Chem. Phys.*, 2003, **119**, 11977.

[44] T. S. Chow, *Macromolecules*, 1979, **13**, 362–364.

[45] J. D. Ferry, *Rev. Mod. Phys.*, 1959, **31**, 130.

[46] J. S. Vrentas and J. L. Duda, *J. Polym. Sci.: Polym Phys. Ed.*, 1977, **15**, 403–416.

[47] J. S. Vrentas and J. L. Duda, *J. Polym. Sci.: Polym Phys. Ed.*, 1977, **15**, 417–439.

[48] J. S. Vrentas and J. L. Duda, *J. Polym. Sci.: Polym Phys. Ed.*, 1977, **15**, 441–453.

[49] D. Turnbull and M. H. Cohen, *J. Chem. Phys.*, 1961, **34**, 120.

[50] R. N. Haward, *The physics of glassy polymers*, Applied science publishers, Essex UK, 1970.

[51] G. C. Berry and T. G. Fox, *Adv. Polym. Sci.*, 1968, **5**, 261.

[52] F. Bueche, *J. Chem. Phys.*, 1952, **20**, 1959–1964.

[53] D. G. Bucknall, S. A. Butler and J. S. Higgens, *Macromolecules*, 1999, **32**, 54535456.

[54] L. A. Weisenberger and J. L. Koenig, *Polvm. Prepr. (Am . Chem. Soc., Div. Polym. Chem.)*, 1988, **29**, 98.

[55] H.-L. Lv, B. Wang and Y. Kong, *Polymer Journal*, 2009, **41**, 10491054.

[56] C. J. Ellison and J. M. Torkelson, *Nature Materials*, 2003, **2**, 695–700.

[57] S.-U. Hong, *Ind. Eng. Chem. Res.*, 1997, **15**, 501–505.

[58] J. S. Vrentas, J. L. Duda and H.-C. Ling, *J. Polym. Sci. B: Poly. Phys.*, 1989, **27**, 1179.

[59] J. D. Ferry, *Viscoelastic Properties of Polymers 3rd edn*, Wiley, New York USA, 1980.

[60] J. E. Mark, *Physical properties of Polymers Handbook*, American Institute of Physics, Yew York USA, 1996.

[61] G. Li, H.-J. Butt and K. Graf, *Langmuir*, 2006, **22**, 11395–11399.

[62] E. N. Brown, N. R. Sottos and S. R. White, *Experimental Mechanics*, 2002, **42**, 372–379.

[63] J.-H. Park and P. V. Braun, *Adv. Mater.*, 2010, **22**, 496–499.

[64] S. D. Mookhoek, *this thesis, chapter* **??**.

[65] A. Altinkaynak, M. Gupta, M. A. Spalding and S. L. Crabtree, *Poly. Eng. Sci.*, 2009, **49**, 471–477.

[66] E. N. Brown, M. R. Kessler, N. R. Sottos and S. R. White, *J. Microencapsulation*, 2003, **20**, 719–730.

[67] J. D. Rule, N. R. Sottos and S. R. White, *Polymer*, 2007, **48**, 3520–3529.

[68] W. Beres, K. K. Ashok and R. Thambraj, *J. Test. Eval.*, 1997, **25**, 536–542.

[69] L. Yuan, A. Gu and G. Liang, *Mater. Chem. Phys.*, 2008, **110**, 417–425.

[70] J. Brandrup and E. H. Immergut (ed.), *Polymer Handbook II*, Wiley, New York USA, 1989.

[71] L. A. Shepp and J. B. Kruskal, *Amer. Math. Monthly*, 1978, **85**, 420–439.

[72] J. C. Elliot and S. D. Dover, *J. Microscopy*, 1982, **126**, 211–213.

[73] E. Maire, J.-Y. Buffiere, L. Salvo, J. J. Blandin, W. Ludwig and J. M. Letang, *Adv. Eng. Mater.*, 2001, **3**, 539–546.

[74] K. H. Khor, J.-Y. Buffiere, W. Ludwig, H. Toda, H. S. Ubhi, P. J. Gregson and I. Sinclair, *J. Phys. Condens. Mater.*, 2004, **16**, 3511–3515.

[75] S. C. Mayo, T. J. Davis, T. E. Gureyev, P. R. Miller, D. Paganin, A. Pogany, A. W. Stevenson and S. W. Wilkins, *Opt. Express*, 2003, **11**, 2289–2302.

[76] S. C. Mayo, P. R. Miller, S. W. Wilkins, T. J. Davis, T. E. Gao, T. E. Gureyev, D. Paganin, D. J. Parry, a. Pogany and A. W. Stevenson, *J. Microscopy*, 2002, **207**, 79–96.

[77] T. Yin, L. Zhou, M. Z. Rong and M. Q. Zhang, *Smart Mater. Struct.*, 2008, **17**, art. no. 015019.

[78] S. D. Mookhoek, *this thesis, chapter 3*.

[79] D. Paganin, S. C. Mayo, T. E. Gureyev, P. R. Miller and S. W. Wilkins, *J. Microscopy*, 2002, **206**, 33–40.

[80] P. Cloetens, W. Ludwig, J. Baruchel, D. van Dyck, J. van Landuyt, J. P. Guigay and M. Schlenker, *Appl. Phys. Lett.*, 1999, **75**, 2912–2914.

[81] *Amira software (Visage Imaging) see http://www.amiravis.com/*, 2010.

[82] E. Maire, P. Colombo, J. Adrien, Babout and L. Biasetto, *J. Eur. Cer. Soc.*, 2007, **27**, 1973–1981.

[83] R. Arshady, *J. Microencapsulation*, 1989, **1**, 13–28.

[84] M. M. Gutcho, *Microcapsules and Microencapsulation Techniques*, Noyes Data Co., New Jersey, USA, 1976.

[85] A. Kondo, *Microcapsule Processing and Technology*, Marcel Dekker Inc., New York, USA, 1979.

[86] S.-J. Park, Y.-S. Shin and J.-R. Lee, *J. Colloid Interface Sci.*, 2001, **241**, 502–508.

[87] B. F. Gibbs, S. Kermasha, I. Alli and C. N. Mulligan, *Int. J. Food. Sci.*, 1999, **50**, 213–224.

[88] M. I. Goller and B. Vincent, *Colloid Surf.*, 1998, **142**, 281–285.

[89] A. S. Utada, E. Lorenceau, D. R. Link, P. D. Kaplan, H. A. Stone and D. A. Weitz, *Science*, 2005, **308**, 537–541.

[90] D. L. Gardner, *World Pat. WO83/03061*, 1983.

[91] C. Microcaps", *Ger. Pat. DE20221414U*, 2005.

[92] T. Matsushita and S. Morishita, *US Pat. US4891172*, 1983.

[93] D. Dinsmore, M. F. Hsu, M. G. Nikolaides, M. Marques, A. R. Bausch and D. A. Weitz, *Science*, 2002, **289**, 1006–1009.

[94] S. U. Pickering, *J. Chem. Soc., Trans.*, 1907, **91**, 2001–2021.

[95] W. Ramsden, *Proc. R. Soc. London, Ser. B*, 1903, **72**, 156–164.

[96] P. Finkle, H. D. Draper and J. H. Hildebrand, *J. Am. Chem. Soc.*, 1923, **45**, 2780–2788.

[97] P. Pieranski, *Phys. Rev. Lett.*, 1980, **45**, 569–572.

[98] M. E. Leunissen, A. van Blaaderen, A. D. Hollingsworth, M. T. Sullivan and P. M. Chaikin, *Proc. Natl. Acad. Sci. U. S. A.*, 2007, **108**, 2585–2590.

[99] O. D. Velev, K. Furusawa and K. Nagayama, *Langmuir*, 1996, **12**, 2374–2384.

[100] B. J. Blaiszik, N. R. Sottos and S. R. White, *Compos. Sci. Technol.*, 2008, **68**, 978–986.

[101] G. Odian, *Principles of Polymerization*, 2nd ed., John Wiley and Sons, New York, USA, 1981.

[102] M. W. Keller, S. R. White and N. R. Sottos, *Experimental Mechanics*, 2006, **46**, 725–733.

[103] P. G. Shukla, B. Kalidhass, A. Shah and D. V. Palaskar, *J. Microencapsulation*, 2002, **19**, 293–304.

[104] Y. Frere, L. Danicher and P. Gramain, *Eur. poly. J.*, 1997, **34**, 193–199.

[105] K. Hong and S. Park, *J. Appl. Polym. Sci.*, 2000, **78**, 894–898.

[106] P. G. Shukla and S. Sivaram, *J. Microencapsulation*, 1999, **16**, 517–521.

[107] S. A. F. Bon and T. Chen, *Langmuir*, 2007, **23**, 9527–9530.

[108] T. J. Lardner and P. Pujara, *Compression of spherical cells.*, 1980.

[109] *Air Products, product specification sheet*, 2009.

[110] S. A. F. Bon, S. D. Mookhoek, P. J. Colver, H. R. Fischer and S. van der Zwaag, *European Polymer Journal*, 2007, **43**, 4839–4842.

[111] S. D. Mookhoek, *this thesis, chapter 7.*

[112] B. J. Blaiszik, S. R. White and N. R. Sottos, *2nd Int. Conference on Self-Healing Materials proceedings*, 2009, **Chicago**, .

[113] G. Vertogen and W. H. de Jeu, *Thermotropic Liquid Crystals - Fundamentals*, Springer-Verlag, 1988.

[114] H. G. Elias, *An introduction to plastics*, Wiley-VHC, 2nd edn., 2003.

[115] J. C. Halpin, *J. Compos. Mater.*, 1969, **3**, 732734.

[116] J. C. Halpin and J. L. kardos, *Polym. Eng. Sci.*, 1976, **16**, 344–352.

[117] M. A. van Es, F. Xiqiao, J. van Turnhout and E. van der Giessen, *Comparing polymer-clay nanocomposites with conventional composites using composite modeling*, Blackwell Science, Oxford, 2001.

[118] E. D. De Souza, M. Brinkmann, C. Mohrdieck and E. Arzt, *Langmuir*, 2008, **24**, 8813–8820.

[119] P.-G. de Gennes, F. Brochard-Wyart and D. Quere, *Capillary and Wetting Phenomena - Drops, Bubbles, Pearls, Waves*, Springer, 2002.

[120] A. A. Griffith, *Phil. Trans. Roy. Soc. A*, 1921, **221**, 163198.

[121] H. N. Yow and A. F. Routh, *Soft Matter*, 2006, **2**, 940–949.

[122] C. Thies, *A short history of microencapsulation technology*, Citus Books, London, 1999.

[123] S. Park and R. Arshady, *Microcapsules for Fragrances and Cosmetics*, Citus Books, London, 2003.

[124] S. K. Gosh, *Functional Coatings: By Polymer Microencapsulation*, Wiley-VCH, 2006.

[125] F. J. Rossier-Miranda, C. G. P. H. Schroen and R. Boom, *Colloids Surf. A.*, 2009, **343**, 43–49.

[126] B. Holt, R. Lam, F. C. Meldrum, S. D. Stoyanov and P. N. Paunov, *Soft Matter*, 2007, **3**, 188–190.

[127] F. Caruso, *Chem. Eur. J.*, 2000, **6**, 413–419.

[128] V. Sibillo, G. Pasquariello, M. Simeone, V. Cristini and S. Guido, *Phys. Rev. Let.*, 2006, **97**, art. 054502.

[129] M. Husmann, H. Rehage, E. Dhenin and D. Barthes-Biesel, *J. Colloid Interf. Sci.*, 2005, **282**, 109–119.

[130] A. M. Seifert and J. H. Wendorff, *Colloid and Polym. Sci.*, 1992, **270**, 962–971.

[131] I. Kobayashi, K. Uemura and M. Nakajima, *Langmuir*, 2006, **22**, 10893–10897.

[132] B. J. Briscoe, C. J. Lawrence and W. G. P. Mietus, *Advances in Colloid and Interface Science*, 1999, **81**, 1–17.

[133] H. P. Grace, *Chem. Eng. Comm.*, 1982, **14**, 225.

[134] G. I. Taylor, *Proc. Roy. Soc. London A*, 1934, **146**, 501.

[135] S. Torza, C. P. Henry, R. G. Cox and S. G. Mason, *J. Colloid Interface Sci.*, 1971, **35**, 529.

[136] K. Hyun, S. H. Kim, K. H. Ahn and S. J. Lee, *J. Non-Newtonian Fluid Mech.*, 2002, **107**, 51–65.

[137] M. L. Soto-Portas, J. F. Argillier, F. Mechin and N. Zydowicz, *Poly. Int.*, 2003, **52**, 522–527.

[138] L. J. J. M. Janssen and K. t. Nijenhuis, *J. Membrane Sci.*, 1992, **65**, 69–75.

[139] P. Aebischer, L. Wahlberg, P. A. Tresco and W. S. R., *Biomaterials*, 1991, **12**, 50–56.

[140] A. Greiner and J. H. Wendorff, *Angewandte Chemie International Edition*, 2007, **46**, 5670 – 5703.

[141] R. J. Houben, A. Rijfers, L. A. M. Brouwers, J. Eversdijk and K. J. C. van Bommel, Eur. Pat. EP202026A1, 2009.

[142] S. D. Mookhoek, *this thesis, chapter 5*.

[143] P. J. Colver, T. Chem and S. A. F. Bon, *Macromol. Symp.*, 2006, **245/246**, 34.

[144] L. L. Schramm, *Emulsions, Foams and Dispersions*, Wiley-VCH, 2005.

[145] F. Yang, Q. Niu, Q. Lan and D. Sun, *J. Colloid Interface Sci.*, 2007, **306**, 285–295.

[146] J. Kim, J. L. Anderson, S. Garoff and P. J. Sides, *Langmuir*, 2002, **18**, 5387–5391.

[147] S. Cauvin, P. J. Colver and S. A. F. Bon, *Macromolecules*, 2005, **38**, 8316.

[148] S. A. F. Bon, S. Cauvin and P. J. Colver, *Soft Matter*, 2007, **3**, 194.

[149] T. Chen, P. J. Colver and S. A. F. Bon, *Adv. Mater.*, 2007, **19**, 2286.

[150] R. Aveyard, J. H. Clint and T. S. Horozov, *Phys. Chem. Chem. Phys.*, 2003, **5**, 2398.

[151] B. P. Binks and S. O. Lumsdon, *Langmuir*, 2000, **16**, 8622.

[152] B. P. Binks, J. H. Clint, G. MacKenzie, C. Simcock and C. P. Whitby, *Langmuir*, 2005, **21**, 8161.

[153] A. B. Subramaniam, M. Abkarian, L. Mahadevan and H. A. Stone, *Nature*, 2005, **438**, 930.

[154] A. B. Subramaniam, C. Mejean, M. Abkarian and H. A. Stone, *Langmuir*, 2006, **22**, 5986.

[155] R. H. McDowell, *Properties of alginates*, Alginate Industries, London UK, 1956.

[156] E. R. Morris, D. A. Rees, D. Thom and J. Boyd, *Carbohydrate Res.*, 1978, **66**, 145–154.

[157] A. Haug and O. Smidsrod, *Acta Chem. Scand*, 1972, **24**, 843–854.

[158] O. Smidsrod and A. Haug, *Acta Chem. Scand*, 1972, **26**, 79–88.

[159] A. Watthanaphanit, P. Supahol, T. Furuike, S. Tokura, H. Tamura and R. Rujiravanit, *Biomacromolecules*, 2009, **10**, 320–327.

[160] L. Fan, Y. Du, R. Huang, Q. Wang, X. Wang and L. Zhang, *J. Appl. Polym. Sci.*, 2005, **96**, 1625–1629.

[161] S. Safi, M. Morshed, S. A. Hosseini Ravandi and M. Ghiaci, *J. Appl. Polym. Sci.*, 2007, **101**, 425–431.

[162] M. George and T. E. Abraham, *J. Control. Rel.*, 2006, **114**, 1–14.

[163] L.-C. Liao, A. C. A. Wan, E. K. F. Yim and K. W. Leong, *J. Control. Rel.*, 2005, **18**, 347–358.

Appendix: Glossary

List of symbols

Symbol	Description	Dimension
Chapter 1		
t	time	$[h]$, $[min]$, $[s]$
Chapter 2		
δ	solubility parameter	$[MPa^{1/2}]$
R_a	radius of solubility	[-]
J	ratio of radii of solubility	[-]
x	volume fraction	[-]
P_a	vapour pressure	$[bar]$
T	temperature	$[K]$, $[^oC]$
T_g	glass transition temperature	$[K]$
t_{spr}	time for solvent spreading	$[s]$
t_{abs}	time for solvent absorption	$[s]$
t_{pdiff}	time for polymer diffusion	$[s]$
t_{evap}	time for solvent evaporation	$[s]$
t_{sdiff}	time for solvent diffusion	$[s]$
ω_p^*	critical weight fraction of polymer	[-]
M_w	polymer molecular weight	$[g/mol]$
D	diffusion coefficient	$[cm^2/s]$
ζ	Stokes friction coefficient	$[N/(m/s^2)]$
k	Boltzmann's constant	$[m^2kg/Ks^2]$
r	radius of a sphere	$[m]$
η	viscosity	$[Pa.s]$
R	gass constant	$[J/kgK]$

Symbol	Description	Dimension
N_A	Avagadro's constant	$[mol^{-1}]$
M_e	polymer molecular weight between entanglements	$[g/mol]$
$\langle R_2 \rangle$	polymer square mean end-to-end distance	$[m^2]$
ρ	polymer mass density	$[g/cm^3]$
N	number of freely orientated polymer segments	[-]
N^*	number of effective polymer segments	[-]
γ	overlap factor	[-]
ω	polymer weight fraction	[-]
$\hat{V}^*$	critical volume at $0K$	$[cm^3/g]$
$\hat{V}^*_{FH}$	total free hole volume	$[cm^3/g]$
K_{ij}	specific system constant	[-]
ξ	solvent-polymer ratio of jumping unit molecular volume	[-]
L	diffusion length	$[m]$
τ_{rep}	reptation time	$[s]$
Chapter 3		
δ	chemical shift	$[ppm]$
G'	storage modulus	$[Pa]$
HE_{str}	average strength related healing efficiency	[-]
Chapter 4		
Ψ	fracture probability	[-]
d	capsule diameter	$[m]$
A	crack area	$[m^2]$
V	sample volume	$[m^3]$
n	total number of intersected capsules	[-]
N	total number of present capsules	[-]
ϕ	capsule volume concentration	[-]
V_{caps}	capsular volume	$[m^3]$
$V_{released}$	total released volume per intersection	$[m^3]$
Chapter 5		
E_s	total system energy	$[J]$
σ	liquid-liquid interfacial tension	$[J/m^2]$
f	volume ratio	[-]
V	liquid volume	$[m^3]$
ΔH^{Trans}	measured heat of evaporation	$[J]$
ΔH^{Vap}	specific heat of evaporation	$[J/g]$
ρ	material density	$[kg/m^3]$
d	capsule diameter	$[m]$
D_{eff}	effective capsule diameter	$[m]$
h	capsule shell wall thickness	$[m]$
ϕ	droplet coverage factor	[-]
E	shell wall modulus	$[Pa]$
r	capsule radius	$[m]$
δ	measured displacement	$[m]$
P	measured load	$[N]$

Symbol	Description	Dimension
Chapter 6		
V_{caps}	capsular volume	$[m^3]$
d	capsule diameter	$[m]$
$V_{released}$	total released volume per intersection	$[m^3]$
A	crack area	$[m^2]$
ϕ	droplet coverage factor	[-]
AR	aspect ratio	[-]
RIF	release improve factor	[-]
MIF	modulus improve factor	[-]
$\langle P_2 \rangle$	2nd order Legendre polynomal	[-]
θ	angle to normal axis	$[rad]$
ϵ	geometrical constant	[-]
E_c	composite modulus	$[Pa]$
E_m	matrix material modulus	$[Pa]$
E_f	filler material modulus	$[Pa]$
ζ	shape factor	[-]
$PCOD$	parallel crack opening distance	$[m]$
γ_l	liquid surface tension	$[J/m^2]$
β	liquid-surface contact angle	$[^o]$
Chapter 7		
Ca	capillary number	[-]
τ	shear stress	$[Pa]$
$\dot{\gamma}$	shear rate	$[s^{-1}]$
R, r	droplet radius	$[m]$
S	degree of anisotropy	[-]
D	length of droplet short axis	$[m]$
L	length of droplet long axis	$[m]$
λ	liquid viscosity ratio	[-]
C	concentration	$[wt\%]$
w_{part}	total weight of particles	$[g]$
w_d	total weight of dispersed phase	$[g]$
r_{part}	radius of particle	$[m]$
Chapter 8		
d	fibre diameter	$[m]$
E	fibre modulus	$[GPa]$
ϵ^X	strain at break	[%]
R^X	tensile strength	$[MPa]$

Summary

Novel routes to liquid-based self-healing polymer systems

The main objective of this thesis was to explore novel routes for self-healing polymer systems which surpasses the classical two-component liquid-based systems comprising either capillaries or capsules as liquid storage medium.

The first concept presented is that of a one-component solvent-based healing mechanism for thermoplastic materials in which the solvent is able to heal cracks by locally reducing the glass transition temperature and inducing increased molecular mobility. Reptation of the polymer chains in combination with re-entanglements results in a welded crack once the solvent has been removed. In *Chapter 2* potentially effective healing solvents are selected on the basis of their vapour pressure and the Hansen solubility model for amorphous thermoplastics, specifically for PS and PMMA. Solvent contact experiments together with micro-indentations show that solvent absorption proceeds at a much higher rate than solvent desorption. Hence, the latter can be expected to dominate the healing kinetics. Upon solvent intrusion the T_g of the surface is depressed to values below room temperature. The solvent dependent behaviour of the materials T_g depression was found to correlate well with the solvent assisted healing behaviour recorded in lapshear tests, evaluating the ability to weld two plastic surfaces. The lapshear tests demonstrate that the solvent assisted healing is time dependent and that substantial healing can be achieved at long healing times when non-volatile solvents are used. The polymer diffusion time across the interface could be estimated from calculated diffusion coefficients. Polymer re-entanglement is expected to occur in the order of hours or days for PS and PMMA (depending on the temperature) when solvent concentrations cause the plasticised material's T_g to drop below room temperature. The combined results provide the basis for a concept of a solvent-induced self-healing mechanism for thermoplastic materials.

In *Chapter 3* it is demonstrated that the non-reactive solvents are indeed able to heal thermoplastic materials without external intervention. The selected solvents can be encapsulated successfully in urea-formaldehyde capsules and the success of the encapsulation is confirmed by optical microscopy and DSC. The permeability of the shell wall is evaluated to ensure that no premature leakage of the solvent into the monomer resin occurs during material preparation. The stability of the prepared capsules against solvents is guaranteed for processing with polymer-solvent mixtures with high solubility.

A suitable thermoplastic matrix material is made by accelerated radical bulk polymerisation at room temperature of a custom MMA-polymer (PMMA or PS) resin, allowing control over the resin viscosity. This route allows embedding of the solvent-filled microcapsules at ambient temperatures, whereas conventional mixing of capsules and the thermoplastic material would involve melt processing techniques. The radical bulk-polymerisation resulted in adequate material properties comparable to commercially available PMMA. When evaluating the mechanical properties such as fracture and healing the polymer matrix shows a significant effect of ageing in the first week. It is found that reproducible data for fracture and healing experiments are only obtained when experiments are performed at least 7 days after preparation.

Depending on the capsule loading and healing time, cracks were only healed partly and a maximum strength related healing efficiency of 30% is obtained for a capsule loading of 15 wt% after healing time of 14 days. It is concluded from experiments that the removal of solvent is a crucial factor for healing and the healing time is found to be the predominant parameter for recovery.

In order to clarify and to quantify the solvent healing mechanism, the fracture and release processes taking place around the crack-zone of a self-healing thermoplastic material have been investigated in detail by SEM-based and synchrotron x-ray microtomography in *Chapter 4*. The 3D microtomography coupled with image segmentation and analysis allowed a quantitative analysis of the relevant processes in a microcapsule based self-healing thermoplastic material, as capsules having released their content could be distinguished from those still intact.

From the reconstructed static tomographic data it is observed that there was good healing across a sizeable fraction of the crack, which is in agreement with an SEM investigation of the crack surfaces. A more detailed segmentation of the crack area showed that the total amount of solvent released at the crack can be determined quantitatively. The measured value of the released solvent volume is in good agreement with the theoretical value predicted *via* statistical calculations.

Dynamic studies on liquid release as a function of time after fracture demonstrated that microcapsules outside the direct crack-path show an unplanned delayed rupture and healing-agent release which depends on the capsule size. The measurements show that the volume of released solvent is absorbed by the PMMA-PS matrix at a fast rate and a cloud-like domain

of high solvent concentration is formed around the original position of the capsule with a radius approximately twice the original capsule diameter. This cloud leads to approximate values of the swollen material's T_g that are close to room temperature. Evaluation of the solvent penetration inside the matrix materials indicated that solvent homogenisation as a function of time does not occur within the time of experiments and local solvent induced mobility is warranted for long times, in line with the conclusions of *Chapter 3*.

In *Chapter 5* a unique fabrication method is described to create binary microcapsules containing two distinct liquid components, designed for guaranteed simultaneous release of two liquid healing components at a fixed ratio at the same location.

Small scale liquid filled microcapsules are used as Pickering stabilizers for a second dispersed liquid and in combination with an interfacial polymerization a peripherally organised capsular structure is produced. The capsule morphology, confirmed by fluorescent optical microscopy and SEM, shows that the small liquid-filled microcapsules form a layer around the main liquid core and are incorporated into the shell wall during encapsulation. DSC experiments confirm the presence of both of the encapsulated phases within a single capsule structure. Quantitative analysis indicates a liquid volume fraction of 8.8% for the small microcapsules. On the basis of the observed architecture and dimensions, this value is in good agreement with a calculated theoretical fraction. The capsule mechanical properties are probed by single capsule compression tests and they reveal a high compliance and ductile deformation behaviour for the polyurethane shell wall material. The deformation behaviour of the capsule and the modulus of the shell wall are barely affected by the presence of the peripherally incorporated microcapsules.

In *Chapter 6* a new geometrical model is presented to quantitatively predict the amount of healing agent released per unit of fracture surface area as a function of the capsule dimensions, volume fraction, aspect ratio. In the case of elongated capsules also the influence of capsule orientation is investigated. On the basis of the amount of released healing-agent per crack area a strong improvement is predicted for elongated capsules. The full alignment and orientation of such elongated microcapsules perpendicular to the crack plane also has a significant positive effect upon the healing potential. Such a large predicted increase in healing efficiency by releasing more healing-agent per crack area allows a reduction of the capsule volume fraction, resulting in better initial mechanical properties and lower costs.

In *Chapter 7* different production routes towards such anisotropic microcapsules with increased fracture probability are evaluated. The first method involves encapsulation of deformed droplets in plain shear and in elongational flow by interfacial polymerisation routes. To achieve this an oil-in-water emulsion is initially created and the dispersed phase is deformed under shear or elongational flow conditions. The degree of deformation is a function of the viscosity ratio of the two liquid-phases and of the interaction between the dispersed and continuous phase. Droplet deformation *via* these methods results in a low degree of

anisotropy (maximal 2.2) for a very restricted shear rate regime only for plain shear. Most likely an instability of the deformed droplets in the high shear regime prevents the production of desirable high aspect ratio microcapsules.

The second method to produce elongated microcapsules is based on a novel ink-jet printing technique to encapsulate liquids. In this technique liquid droplets are ejected by a nozzle at high speed through a thin film of a second liquid material. When exiting the film a thin layer of the second phase forms itself around the droplet. Coagulation or crystallisation of the circumferential layer leads to encapsulation of the liquid droplet. It is shown that the technique also allows the production of elongated microcapsules. However, the printed particles exhibited non uniform shapes and appeared unstable over time. The printing procedure at its current stage of development is still very technologically challenging.

The third and more successful route is based on Pickering stabilised emulsion droplets using laponite armoured latices deformed in a confined space. In the presence of an excess of Pickering particles the increased interfacial area re-saturates with solid particles and the deformed droplet shapes gain stability. When removing the confinement, the droplet remains anisotropic because of interlocking of the solid particles at the over-occupied interface, whereas it would normally relax back to a spherical shape. Through this method stable elongated droplets up to aspect ratios of 10 were created.

In *Chapter 8* compartmented fibres are presented as another strategy for storage and release of healing-agents for composite materials. These fibres allow macroscopic handling of the liquid-carring media and positioning of healing-agent at damage prone sites. Additionally, due to their compartmented structure, the healing-agent release from the fibre is controlled at fibre rupture, allowing equal release characteristics in the case of multiple cracking events. The fibres can be made through common fibre spinning techniques enabling a facile production route. Liquid can be stored within the fibres inside separate vacuoles of which the morphology can be controlled. The fibre mechanical properties are comparable to properties of commonly used composite resins such as epoxy resin. When embedding the fibres inside a polymer matrix material, controlled cracking of the samples in 3-point bending mode shows that the healing-agent release from a crack is adequate for a single healing event and that the degree of crack filling is comparable to that obtained via spherical capsules at equal volume concentrations.

Steven Dirk Mookhoek, 2010

Samenvatting

Nieuwe routes naar vloeistof-gebaseerde zelfherstellende polymeer systemen

De doelstelling van dit proefschrift was het verkennen van nieuwe strategieën ten behoeve van zelfherstellende polymeer systemen die verder gaan dan de klassieke twee-component vloeistof-gebaseerde systemen gebaseerd op capillairen of capsules als opslagmedium voor de reactieve vloeistoffen.

Het eerste concept omvat een één-component zelfherstellende systeem voor thermoplastische materialen dat is gebaseerd op oplosmiddelen. In deze systemen is het oplosmiddel in staat om scheuren te doen repareren door de glasovergangstemperatuur lokaal te verlagen en daardoor de mobiliteit van de polymeerketens in de matrix te verhogen. Reptatie gevolgd door nieuwe entanglements van de polymeerketens leidt dan tot een gerepareerde scheur na verdere verdamping van het oplosmiddel. In *Hoofdstuk 2* zijn potentieel effectieve oplosmiddelen voor zelfherstel aan de hand van hun dampspanning en aan de hand van Hansens oplosbaarheidsmodel voor amorfe thermoplasten (PS en PMMA) geselecteerd. Contacttijd-experimenten van oplosmiddelen op PS en PMMA gevolgd door micro-indentaties laten zien dat de absorptie van de oplosmiddelen veel sneller verloopt dan de desorptie. Wanneer het oplosmiddel het polymeer binnendringt, verlaagt het de glasovergangstemperatuur van het oppervlak tot waarden beneden kamertemperatuur. De invloed van het type oplosmiddel op de glasovergangstemperatuur als functie van de solvent concentratie komt goed overeen met experimentele observaties tijdens oplosmiddel-gebaseerde adhesie-experimenten tussen twee thermoplastische lagen, waarin de potentie van de oplosmiddelen om de kunststoffen te repareren werd gevalueerd. Deze adhesie-experimenten tonen aan dat de oplosmiddel-gebaseerde zelfherstelprocessen tijdafhankelijk zijn en dat voldoende zelfherstel voor niet-vluchtige oplosmiddelen alleen breikt kan worden na een lange tijd van herstel. Uit de diffusiecoëfficienten kan geschat worden hoeveel tijd nodig is voor het diffunderen van poly-

meerketens over de totale scheurbreedte. Het ontstaan van nieuwe entanglements van polymeerketens in de scheur treedt op in een tijdsbestek van enkele uren tot dagen voor PS en PMMA (afhankelijk van de temperatuur) wanneer de oplosmiddelconcentraties zodanig hoog zijn dat de glasovergangstemperatuur beneden de hersteltemperatuur ligt. Tezamen bieden de resultaten een basis voor de ontwikkeling van een oplosmiddel gebaseerd zelfherstelmechanisme in thermoplastische materialen.

In *Hoofdstuk 3* wordt aangetoond dat niet-reactieve oplosmiddelen daadwerkelijk in staat zijn autonoom thermoplastische materialen te herstellen. De eerder geselecteerde oplosmiddelen kunnen succesvol worden geïncapsuleerd in urea-formaldehyde capsules en de aanwezigheid van de geïncapsuleerde vloeistoffen kan worden aangetoond met behulp van DSC. De permeabiliteit van de capsules voor de opgesloten oplosmiddelen is bepaald om er zeker van te zijn dat er geen oplosmiddel voortijdig uit de capsules lekt tijdens het maken van de proefstukken. De metingen laten zien dat er geen oplosmiddel door de wand van de capsules diffundeert wanneer de capsules gemengd worden met een monomeer/polymeer mengsel voor de vervaardiging van test-materialen.

Een geschikt thermoplastisch materiaal wordt gemaakt door middel van versnelde radicaal bulk-polymerisatie bij kamertemperatuur van een speciaal geprepareerde polymeeroplossing van MMA monomeer met voorgepolymeriseerd PMMA of PS waarmee de viscositeit van de oplossing gecontroleerd kan worden. Deze route maakt het mogelijk de oplosmiddel gevulde microcapsules in te bedden bij lage temperaturen, terwijl het inmengen in thermoplasten via conventionele routes in de smelt van de polymeren zou moeten gebeuren. De gebruikte radicaal bulk-polymerisatie resulteert in adequate materiaal eigenschappen die vergelijkbaar zijn met die van commercieel verkrijgbaar PMMA. De mechanische eigenschappen zoals die van breuk en zelfherstel vertonen een sterk afhankelijk gedrag van de verouderingstijd in de eerste week na vervaardiging van de materialen. Reproduceerbare data voor breuk en zelfherstel kunnen pas minimaal 7 dagen na vervaardiging gemeten worden.

Geïntroduceerde scheuren kunnen slechts gedeeltelijk geheeld worden en de mate is afhankelijk van de capsuleconcentratie en de toegestane hersteltijd. Een maximaal herstel van eigenschappen van 30% is verkregen voor een capsuleconcentratie van 15 gew% na een hersteltijd van 14 dagen. Uit de experimenten kan het geconcludeerd worden dat het verdwijnen van het oplosmiddel een cruciale factor is voor het herstel en dat de hersteltijd een van de belangrijkste parameters is voor deze oplosmiddel-gebaseerde systemen.

Teneinde het mechanisme van oplosmiddel-gebaseerd zelfherstel voor thermoplastiche materialen beter te begrijpen, zijn in *Hoofdstuk 4* de processen van breuk en de vrijgave van het oplosmiddel rond de scheur gedetailleerd onderzocht met behulp van electronenmicroscopie- en synchrotron gebaseerde Röntgen microtomografie. Driedimensionale microtomografie samen met beeldsegmentatie en beeldanalyse maakt een kwantitatieve analyse mogelijk van de relevante processen in een zelfherstellend thermoplastich materiaal dat capsules met vloeistof bevat.

Statische tomographische metingen duiden aan dat er over een groot deel van het scheuroppervlak zelfherstel optreedt, hetgeen ook geconcludeerd kan worden uit raster- electronenmicroscopie studies van de breukoppervlakken na een tweede breuk. De gemeten hoeveelheid oplosmiddel die is vrijgegeven in de scheur komt goed overeen met de theoretische waarde die bepaald is aan de hand van statistische berekeningen.

Dynamische studies naar het vrijgeven van het oplosmiddel als functie van de tijd na scheurvorming, laten zien dat ook microcapsules, die niet in het directe pad van de scheur liggen, op een later tijdstip oplosmiddel kunnen vrijgeven en dat de snelheid van dit proces afhankelijk is van de capsulegrootte. De metingen laten eveneens zien dat het vrijgegeven volume aan oplosmiddel snel geabsorbeerd wordt door de PMMA-PS matrix in een gebied van ongeveer tweemaal de diameter van de oorspronkelijke capsule. Dit absorptie volume leidt tot een waarde van de glasovergangstemperatuur die dicht tegen kamertemperatuur aanligt. Het beperkte indringgedrag van het oplosmiddel in de thermoplastische matrix duidt erop dat homogenisering van het oplosmiddel niet optreedt gedurende het tomografische experiment en dat de mobiliteit van de polymeerketens op lokaal niveau voor een lange tijd gewaarborgd is. Dit laatste komt overeen met de conclusies van *Hoofdstuk 3*.

In *Hoofdstuk 5* wordt een unieke methode voor het maken van twee-component capsules beschreven, welke ontworpen was met het doel gelijkertijd twee vloeistoffen in de juiste verhoudingen en op de zelfde plaats voor het zelfherstellende mechanisme vrij te geven.

Zeer kleine vloeistof gevulde microcapsules worden gebruikt als Pickering deeltjes om een andere vloeistof te stabiliseren in een dispersie. Vervolgens kan met behulp van een grensvlakpolymerisatie hiervan een microcapsule gemaakt worden met een architectuur bestaande uit een centrale vloeistofkern en daar omheen een schil van een tweede geincapsuleerde vloeistof. De morfologie van de capsules kan worden aangetoond door middel van fluorisentie- en electronenmicroscopie. DSC metingen bevestigen de aanwezigheid van beide ingesloten vloeistoffen in één enkele microcapsule. Een kwantitatieve analyse van de binaire microcapsules met behulp van DSC geeft aan dat er ca. 8.8 vol% aan vloeistof van de kleine microcapsules is ingesloten ten opzichte van de centrale tweede vloeistof. Aan de hand van de geobserveerde morfologie en de capsule afmetingen kan tevens een theoretische waarde voor de ratio tussen de twee vloeistoffen worden berekend die overeenkomt met de experimentele waarde. De mechanische eigenschappen van de capsules zijn getest in compressieexperimenten en tonen aan dat de capsulewand van polyurethaan een lage stijfheid heeft en zich ductiel gedraagt tijdens deformatie. De aanwezigheid van kleine microcapsules in de wand van de capsules blijkt geen significant effect te hebben op de mechanische eigenschappen.

In *Hoofdstuk 6* wordt een geometrisch model beschreven voor zelfherstelende materialen om de hoeveelheid vrijgegeven vloeistof per oppervlak als functie van de capsuleafmetingen, -concentratie en lengte-breedteverhouding kwantitatief te voorspellen. In het geval van langwerpige capsules is ook de invloed van ruimtelijke oriëntatie van de capsules meegenomen. Het model voorspelt een toename van het potentieel voor zelfherstel van langwerpige

capsules boven dat van sferische capsules. De toename is het gevolg van de stijging van de hoeveelheid vrijgegeven vloeistof per oppervlak. Volledige oriëntatie van de langwerpige capsules loodrecht op de richting van de breuk resulteert tevens in een significante verhoging van de de hoeveelheid vrijgegeven vloeistof per oppervlak. Deze voorspelde verhoging van het potentieel voor zelfherstel door de vrijgave van meer vloeistof per breukoppervlak biedt de mogelijkheid de volume concentratie van de capsules danig te verlagen teneinde de intrinsieke materiaal eigenschappen te behouden.

In *Hoofdstuk 7* worden verschillende routes voor het produceren van langwerpige microcapsules geëvalueerd. Om dit te bereiken wordt allereerst een olie-in-water emulsie gemaakt waarna de gedispergeerde fase vervormd wordt door het opleggen van afschuif- of rekstroming. De mate van vervorming is een functie van de viscositeitsratio en de grensvlakspanning tussen de continue en gedispergeerde fase. Druppeldeformatie en incapsulatie via deze methodes leidt slechts tot microcapsules met een lengte-breedte verhouding van maximaal 2.2 en alleen in een zeer klein regime voor de afschuifsnelheid. De instabiliteit van de vervormde druppels bij hoge afschuifsnelheid blijkt de productie van deeltjes met een gewenste hoge aspect ratio te beperken.

De tweede methode om langwerpige microcapsules te maken is gebaseerd op een nieuwe inkjet-printing techniek om vloeistoffen te incapsuleren. Met deze techniek worden kleine druppels vloeistof via een spuitkop met hoge snelheid door een gordijn van een tweede vloeistof geschoten. Wanneer de druppels door de film gaan blijft er een dunne laag van het vloeistofgordjn rond de druppel achter. Coagulatie en/of kristallisatie van deze buitenlaag leidt dan vervolgens tot de incapsulatie van de druppels. Het is aangetoond dat de techniek ook in staat is langwerpige capsules te maken. De gecreëerde deeltjes zijn echter niet uniform en blijken instabiel. De printtechniek in zijn huidige staat van ontwikkeling blijkt qua afmetingen nog niet voldoende bruikbaar voor grootschalige productie van capsules.

De derde en meest succesvolle methode behelst de vervorming en incapsulatie van emulsiedruppels, die gestabiliseerd zijn met laponiet bezette Pickering deeltjes, tijdens stroming door een capilair. Door een overmaat aan deze Pickering deeltjes in de capillairen kan ook de toename in oppervlak van de vervormde druppelgeometrie gestabiliseerd worden. Wanneer de druppel vervolgens het capillair verlaat, blijft het deeltje anisotroop van vorm omdat het oppervlak teveel Pickering deeltjes bevat. Via deze methode is het gelukt stabiele langwerpige druppels te maken tot een lengte-breedteverhouding van 10.

In *Hoofdstuk 8* worden gecompartimenteerde vezels gepresenteerd als een nieuwe strategie voor het opslaan en vrijgeven van vloeistoffen in zelfherstellende materiaalsystemen. Het voordeel van deze vezels is dat ze macroscopisch zijn en ze daardoor eenvoudig geplaatst kunnen worden daar waar het optreden van schade aan het materiaal de grootste kans heeft. Tevens is de hoeveelheid vloeistof die vrijgegeven wordt door de gecompartimenteerde opbouw van de vezel beperkt tot een klein volume van de vezel. Dit maakt gelijkmatige afgifte van vloeistof mogelijk voor meerdere scheuren over relatief korte afstanden. Het maken van

de vezels gebeurt via conventionele vezel-spintechnieken en de morfologie van de compartimenten waarin de vloeistof is opgeslagen, kan gecontroleerd worden in het productieproces. De mechanische eigenschappen van de vezels tonen aan dat de eigenschappen van de vezel vergelijkbaar zijn met die van composiet harsen zoals epoxy. Wanneer de vezels in een polymeer matrix materiaal ingebed worden, kan met behulp van 3-punt-buigexperimenten aangetoond worden dat er inderdaad vloeistof vanuit de vezel naar de scheur stroomt en dat het scheurvullend vermogen vergelijkbaar is met dat van bolvormige capsules.

Steven Dirk Mookhoek, 2010

Acknowledgements

The great tragedy of Science:
- the slaying of a beautiful hypothesis by an ugly fact.

Thomas Henry Huxley

The completion of this thesis and the work done in the last four years would have been impossible without the supervision, assistance and support of many individuals. Hence, I would like to thank here all who contributed to this work either directly or indirectly.

Firstly, I would like to thank my promotor Prof. dr. ir. Sybrand van der Zwaag and daily supervisor Dr. Hartmut Fischer for their guidance, coaching and help during these years working at the TU Delft. Thank you Sybrand, for giving me the opportunity and lots of freedom to fulfill this PhD project. I always appreciated that you made those extra minutes of your time available to discuss my latest results or answer an urgent question. You were a great mentor and I really enjoyed working for you. Hartmut, I especially owe thanks to you. Your experience in the field of chemistry and materials science has been of great value to me. You have taught me many things, despite the fact that we only met one day a week. I would like to thank you particularly for your enthusiasm, able to motivate me again when I was disappointed after an experiment gone bad.

Secondly, I would like to acknowledge the (financial) support provided by the Dutch Polymer Institute (DPI) and the industrial partners in the consortium. Especially I am grateful for the help of Dr. Pieter de Lange (Teijin Aramid) and Dr. Ludo Aerts (Dow Chemical) during the course of this project.

At the University of Warwick (UK) I would like to thank Dr. Stefan Bon for his offer to be part of his group for two weeks in order to produce anisotropic microcapsules using Pickering stabilisation techniques. During my stay there I enjoyed the collaboration with Patrick Colver and Catheline Colard and because of their assistance the work resulted in a

now frequently cited publication.

I would also like to thank Prof. dr. Scott White and Prof. dr. Nancy Sottos at the Unversity of Illinois at Urbana-Champaign (USA) for giving me the opportunity to work at the Beckman Institute within the Autonomous Materials Systems group for a period of three months. During this internship I have developed many useful skills in the art of microencapsulation and controlled fracture and healing experiments. It was mainly because of the friendship of Magnus Anderson, Mike Keller, Ben Blaiszik and Aaron Jackson that Urbana-Champaign felt like home.

I also would like to acknowledge the financial aid *via* an awarded travel grant from the First International Conference on Self-healing Materials (2007, Noordwijk aan Zee), which allowed a close collaboration with Dr. Anthony Hughes, Dr. Sheridan Mayo and Dr. Scott Furman at CSIRO, Clayton (Australia). Thank you Sherry, for sacrificing a large fraction of your time during those three weeks to perform the XuM X-ray tomography experiments.

At the TU Delft I am indebted to many people for their help and assistance. In particular I would like to thank Frans Oostrum and Serge van Meer for their kind assistance in the experimental work and day to day operations at the lab. Additionally, I am very thankful to Hans Weerheim, Niels Jalvink, Bob de Vogel and Berthil Grashof. I also highly appreciated the input from and discussions with all other materials research related groups at the TU Delft during our monthly Self-healing Material meetings organised by DCMat.

Throughout all of the last four years it was a real honour and pleasure to closely collaborate with a group of bright, interesting, funny and friendly people within the NovAM group at the faculty of Aerospace Engineering. In random order I would like to thank all others (former and current group members) that made every day at work fun: 'The coffee room club' (Alwin, Huang, Arek, Maruti, Mazhar and Chris), Stephane, Chen, Natalia, Doty, Girish, Meiji, Sang Woo, Alexander, Pim, Santiago, Fabrizio, Bui, Russel, Yanmin, Sanna, Xu, Suresh, Rahul, Laura, Geeta, Shanta, Theo, David, Pedro, Daniel, Jie, Wouter, Li, Jason, and Daan. To be honest, I will miss you guys.

I was also very fortunate to have a group of friends that made me enjoy all the other aspects of life, besides research, presentations and writing. Alwin & Ivette, Huang & Xiao, Arek & Alexandra, Maruti and Mazhar, thank you for the friendship and for the lovely dinners that we had together. Martine, thank you for joining me many evenings in drinking a glass or even a whole bottle of wine. Jeroen, Mark, Jorrit and Iwan, I have enjoyed all those weekends together, which really allowed me to forget work for a while.

Finally, I am thankful for all the support from my parents and family, first throughout the years at the University of Twente as a student and later at the TU Delft as a PhD candidate. Thanks *pa* and *ma* for having faith in me all those years. And of course *Renée*, I would probably not be where I am today without your encouragement, trust, love and

understanding. Thanks for being there when I needed it most. Here, I would also like to apologise for all the late evenings at work and for all the occasions that I was far away from home, sometimes even for months.

Leiden, June 2010

Steven

Curriculum Vitae

We make a living by what we get, but we make a life by what we give.

Winston Churchill

Steven D. Mookhoek, was born on November 11, 1979 in Oostburg (Zeeland), The Netherlands. He obtained his 'Atheneum' diploma in 1998 at Scheldemond College in Vlissingen. In September of that year he started his academic study of Chemical Technology at the Faculty of Science and Technology, University of Twente. During his study he performed an internship at Goodyear S.A. in Colmar-Berg, Luxemburg. He obtained his Master of Science degree in December 2005. His Master thesis concerned the investigation towards better and flexible new co-curing agents in thermoplastic-elastomer blends. For this work he was awarded the triennial Förderpreis by the German Rubber Society in 2006.

In January 2006 he started his Ph.D. on a Dutch Polymer Institute project in the Novel Aerospace Materials group led by professor Sybrand van der Zwaag at Delft University of Technology. During his Ph.D. period he spent several periods abroad for scientific collaboration with the Univerity of Warwick (UK), the University of Illinois (USA) and The Commonwealth Scientific Industrial Research Organisation, (Australia).

The author has received two innovation awards from the Dutch Polymer Institute and obtained the title of *Accredited Polymer Scientist* (RPK) from the Dutch National Graduate School of Polymer Science and Technology, PTN (Polymeer Technologie Nederland).

In March 2010 he joined Latexfalt B.V. The Netherlands as New Business Development Manager.

List of publications

2010

- S.D. Mookhoek, H.R. Fischer and S. van der Zwaag, "Design aspects for liquid-based self-healing engineering materials", *Mater. Sci. Eng. C*, **2010**, to be submitted
- S.D. Mookhoek, S.C. Mayo, A.E. Hughes, S.A. Furman, H.R. Fischer and S. van der Zwaag, "Applying SEM-based X-ray Microtomography to Observe Self-healing in Solvent Encapsulated Thermoplastic Materials", *Adv. Eng. Mater.*, **2010**, available online - doi: 10.1002/adem.200900289

2009

- S.D. Mookhoek, H.R. Fischer and S. van der Zwaag, "A Numerical Study into the Effects of Elongated Capsules on the Healing Efficiency of Liquid-based Systems", *Comput. Mater. Sci.*, **2009**, 47(2), 506-511
- S. van der Zwaag, N.H. van Dijk, H.M. Jonkers, S.D. Mookhoek, and W.G. Sloof, "Self-healing behaviour in man-made engineering materials: bioinspired but taking into account their intrinsic character", *Phil. Trans. Series A*, **2009**, 367(1894), 1689-704
- S.R. White, S.D. Mookhoek, N.R. Sottos, B.J. Blaiszik and S. van der Zwaag, "Multi-capsule system and its use for encapsulating active agents", *US patent application US2009181254*, **2009**

2008

- S.J. Picken, S.D. Mookhoek, H.R. Fischer and S. van der Zwaag, "Self-healing in nanoparticle Reinforced Polymers and other Polymer Systems", book chapter in *Optimization of Polymer Nanocomposite Properties*; V. Mittal (ed), **2010** in press, ISBN: 3-527-32521-2
- S.D. Mookhoek, B.J. Blaiszik, H.R. Fischer, N.R. Sottos, S.R. White and S. van der Zwaag, "Peripherally decorated binary microcapsules containing two liquids", *J. Mater. Chem.*, **2008**, 18, 5390-5394
- S.D. Mookhoek and S. van der Zwaag, "Heal Thyself; damage Management by Design", *Plastics Innovations*, **2008**, 1(6), 56-59
- S.D. Mookhoek, H.R. Fischer and S. van der Zwaag, "Polymeric material comprising multiple cavities", *European patent application EP1983025*, **2008**

2007

- S.D. Mookhoek and S. van der Zwaag, "Een nieuw materiaal ontwerpperspectief: zelf-herstellende materialen", De Constructeur, **2007**, 1/2, 38-40

- S.D. Mookhoek, P.J. Colver, H.R. Fischer, S.A.F. Bon and S. van der Zwaag, "The Creation of High Aspect Ratio Capsules to Improve the Efficiency of Self-Healing Polymer Systems", *Conference Proceedings, 1st International Conference on Self Healing Materials*, **2007**, Noordwijk (NL)
- S.A.F. Bon, S.D. Mookhoek, P.J. Colver, H.R. Fischer and S. van der Zwaag, "Route to Stable Non-spherical Emulsion Droplets", *Eur. Polym. J.*, **2007**, 43(11), 4839-4842